A multi-mechanism model for cutting simulations combining asymmetric effects and gradient phase transformations

zur Erlangung des akademischen Grades eines
Doktors der Ingenieurwissenschaften (Dr.-Ing.)
der Fakultät für Maschinenbau
der Universität Paderborn

vorgelegte
Dissertation

von
M.Sc. Chun Cheng
aus Paderborn, Deutschland

Abstract

In order to study the white layer formation and several mechanisms in high speed cutting, we develop a multi-mechanism model (MMM) for cutting simulation taking asymmetric visco-plasticity, phase transformation and transformation induced plasticity (TRIP) into account. To this end, the well-known Johnson-Cook model is extended by the concept of weighting functions for considering the asymmetric effect, which labels different material behaviors under tension, compression and shear. For the special scenario of high speed cutting with martensite as the initial phase, two phase transformations are considered: 1. Transformation of the martensitic initial state into austenite, then 2. retransformation to martensite. The model is formulated within a thermodynamic framework at large strains, and specialized and applied to high speed cutting.

Furthermore, we extend the MMM with a phase gradient based on the concept of generalized stresses proposed by Gurtin and Forest in order to consider different interface energies appearing in phase transformations. To this end, the austenite mass fraction, which represents a chemical variable, is treated as an extra degree of freedom in the modelling part as well as in the finite element formulation. We consider its first gradient and study its influence on the phase transformations. Moreover, hardness dependency and hardness modification due to white layer formation are taken into account.

Zusammenfassung

Um die Weißschichtbildung und verschiedene Mechanismen im Hochgeschwindigkeitszerspanen zu untersuchen, wird ein Mehrmechanismenmodell (MMM) für Zerspansimulation entwickelt, wobei asymmetrische Visko-Plastizität, Phasenumwandlung und Umwandlungsplastizität (TRIP) berücksichtigt werden. Zur Berücksichtigung der asymmetrischen Visko-Plastizität wird das bekannte Johnson-Cook Modell um das Konzept der Wichtungsfunktionen erweitert. Für das spezielle Szenario Hochgeschwindigkeitszerspanen mit Martensit als Anfangsphase werden zwei Phasenumwandlungen berücksichtigt: 1. Umwandlung von der Anfangsphase Martensit in Austenit, dann 2. Rückwandlung in Martensit. Das Modell wird in einem thermodynamischen Rahmen für große Deformation formuliert und anschließend für Hochgeschwindigkeitszerspanen spezialisiert und angewendet.

Des Weiteren wird das MMM zur Berücksichtigung von unterschiedlichen auftretenden Interface-Energien um einen Phasengradienten erweitert, wobei die verallgemeinerte Theorie von Gurtin und Forest zugrunde gelegt wird. Zu diesem Zweck stellt der austenitische Massenanteil eine chemische Variable dar und wird als zusätzlicher Freiheitgrad sowohl in der Materialmodellierung als auch in der Finite-Element-Formulierung behandelt. Der erste Gradient von dem austenitischen Massenanteil wird berücksichtigt und dessen Einfluss auf die Phasenumwandlungen wird untersucht. Darüber hinaus werden Härteabhängigkeit und Härteänderung infolge Weißschichtbildung berücksichtigt.

Preface

Paderborn, 17.01.2019 Chun Cheng

Publications

1. CHENG, C., MAHNKEN, R., 2018, A multi-mechanism model for cutting simulation: A Ginzburg-Landau type phase gradient and numerical implementations, International Journal of Solids and Structures, In Press

2. CHENG, C., MAHNKEN, R., 2016, Extension of A Multi-Mechanism Model: Hardness-based flow and Transformation induced Plasticity for Austenitization, International Journal of Solids and Structures, **102-103**, 127-141

3. CHENG, C., MAHNKEN, R., 2015, A multi-mechanism model for cutting simulations based on the concept of generalized stresses, Comp. Mat. Sci., **100**, B, 144-158

4. MAHNKEN, R.; WOLFF, M.; CHENG, C., 2013, A multi-mechanism model for cutting simulations combining visco-plastic asymmetry and phase transformation, Int. J. Solids Struct. **50**, 3045-3066

5. UHLMANN, E.; MAHNKEN, R.; IVANOV, I. M.; CHENG, C., 2018, Thermo-Mechanical Simulation of Hard Turning with Macroscopic Models, In: Thermal Effects in Complex Machining Processes: final report of the DFG priority programme 1480, Production Engineering, Springer International Publishing,

6. MAHNKEN, R.; CHENG, C.; DÜSING, M.; EHLENBRÖKER, U.; LEISMANN, T., 2016, The concept of generalized stresses for computational manufacturing and beyond. GAMM-Mitt. 39, No.2, S.229–265

7. SCHULZE, V.; UHLMANN, E.; MAHNKEN, R.; MENZEL, A.; BIERMANN, D.; ZABEL, A.; BOLLIG, P.; IVANOV, I. M.; CHENG, C.; HOLTERMANN, R.; BARTEL, T., 2015, Evaluation of different approaches for modeling phase transformations in machining simulation, Production Engineering, Springer

8. UHLMANN, E.; MAHNKEN, R.; IVANOV, I. M.; CHENG, C., 2015, A novel finite element approach to modeling hard turning in due consideration of the viscoplastic asymmetry effect, Procedia Cirp, Proceedings of the "15th CIRP Conference on Modelling of Machining Operations", June 11 - 12, 2015, Karlsruhe, Germany

Contents

Chapter 1

Introduction

1.1 Motivation

High speed cutting is widely used in metal working and plays an important role in modern industry. It is necessary to develop a high-precision and efficient procedure for construction of cutting processes and tools. The classical method for the construction is predominantly based on cutting experiments, which are associated with highly costs on energy, material and time. A possible way for reducing the costs is to use numerical methods, e.g. cutting simulations with the Finite-Element-Method (FEM). In order to apply the cutting simulation purposefully and to obtain realistic simulation results, the description of material behaviors as a starting point for the simulation is of decisive importance. Most Finite-Element systems support different possibilities for the definition of material behaviors. Because of the limitation of predefined material libraries, one can develop its own material models and integrate them into the systems as user-defined subroutines.

In some cutting processes like hard turning of the inner bearing ring with the steel AISI 52100 (see Figure 1.1), white and dark layers can be induced due to phase transformations under the intense, localized, rapid thermal-mechanical loading, which determine the mechanical properties of the workpiece. The white layer is harder than the bulk material and very brittle. Its formation and the induced hardness modification can be predicted by aid of thermo-mechanical simulations. Several macroscopic models were developed
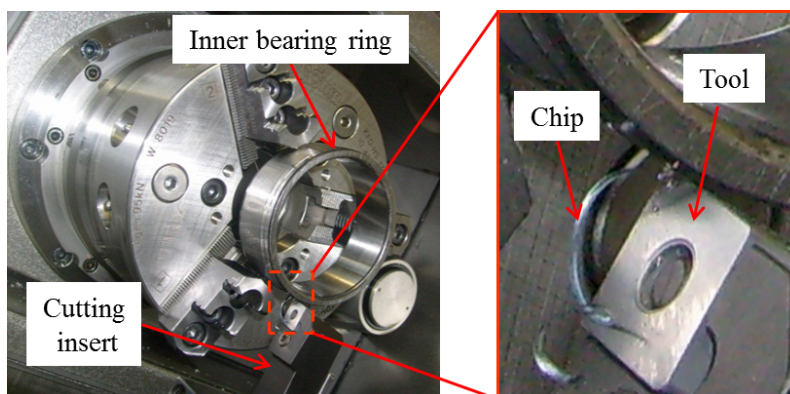
Figure 1.1: Hard turning of inner bearing ring (IWF, TU Berlin).

over the last years to describe the thermo-mechanical effects in cutting simulations. Some effects are still not considered: 1. Inelastic asymmetric effect, which labels different behaviors under different stress modes such as tension, compression and shear; 2. Phase transformation induced plasticity (TRIP), which is induced by the phase transformations under stress loadings; 3. Size effect of phase transformations. In the following section, we will discuss the above mentioned effects in detail.

1.2 State of the art

In cutting and several other metal workings such as turning, milling and drilling processes the workpiece is machined under high speed causing highly inhomogeneous strain rates and temperature, which eventually render residual stresses. To develop three-dimensional constitutive models that account for the finite inelastic deformation of cutting processes, considerable effort was made over the last years. A simple model by DUDZINSKI AND MOLINARI [21] considers the shearing produced during the chip formation in orthogonal cutting. SIEVERT *et al.* [72] consider ductile damage at high strain-rates and the influence of the stress-triaxiality on ductile damage. MARUSICH AND ORTIZ [62] introduce a Lagrangian finite element model with remeshing. Some macroscopic models are developed not for cutting but may also useful for cutting. MAHNKEN *et al.* [58, 59] introduce a macroscopic model taking multi-phase transformations into account for a hybrid forming process. HOLTERMANN *et al.* [35] present an approach for the estimation of a macroscopic heat source term based on a meso-scale finite-element model and a macro-scale kinematic simulation, thereby contributing to a framework to model and simulate Internal Traverse Grinding. UHLMANN *et al.* [79] represent a FEM-modelling for hard turning taking phase transformations into account. In addition, more physically-based models are available, such as the Zerilli-Armstrong model [92], which is based on simplified dislocation mechanics.

A particular role in cutting simulations is played by the well-known Johnson-Cook model [44], where strain softening is incorporated by a phenomenological modification for the yield stress, see e.g. BEHRENS *et al.* [11], OZEL AND ZEREN [67], HORTIG [36], UMBRELLO *et al.* [81] among others. HUH AND KANG [37] introduce a quadratic strain rate form as an improvement to the linear Johnson-Cook strain rate form due to the fact that most materials exhibit a bi-linear dependence of strength on the logarithm of the strain rate, see also SCHWER[71]. Multi-mechanism models are developed over the last years for observing different behaviors in the material, see e.g. CAILLETAUD AND SAÏ[15], SAÏ [70]. These behaviors may be linked to different strain ranges, different stress ranges, different temperatures, etc.

Due to high strain rates and temperature the material microstructure in workpiece surfaces can be changed affecting physical effects such as elasticity, visco-plasticity, asymmetry, phase transformation and transformation induced plasticity (TRIP). The consideration of these effects is a big challenge for material modelling.

Asymmetric effect: Extended experimental tests for high strength steels exhibit different behaviors for different loading types such as tension, compression and shear.

For instance, test results for a superalloy René 95 in STOUFFER and DAME [75] show, that for the same magnitudes of stress in tension and compression the magnitudes of creep rates in tension are much greater than the corresponding rates in compression. A further example is given e.g. in SPITZIG *et al.* [76] for a martensitic steel, where the yield stress in compression is greater than in tension. IWAMOTO *et al.* [40] and MILLER *et al.* [64] obtain the same effect for an austenitc stainess steel. This observation is labelled *strength-difference effect* (SD-effect) or occationally *asymmetric effect*, respectively.

Several publications can be found in the literature for simulation of inelastic material behaviour with asymmetric effects. Most of these approaches are based on a stress potential dependent on the stress tensor and further state variables, which describe e.g. the state of hardening, softening or damage, respectively. Typically, polynomial invariants of the stress tensor are incorporated into the potential. Along this line constitutive equations within the field of plasticity have been formulated e.g. in [76, 4, 49, 93], amongst others. Approaches for asymmetric effects in creep are suggested in [4, 12, 83, 84, 95], amongst others. Some publications used the so-called *stress mode angle*, or *Lode angle*, respectively, in order to detect asymmetric effects. This scalar quantity is expressed in terms of the ratio of the second and third basic invariant of the deviatoric stress tensor and is used as an indicator for detection of differences in the loading mode, see e.g. [94, 22]. In [50] it is used to introduce the concept of *stress mode dependent weighting functions* with the goal to model creep with asymmetric effects.

Phase transformation: Due to friction, plastic deformation and so on, cutting operations lead to a significant heat production. The heat gets distributed into the chips, the work piece, the tool and the environment, and causes phase transformations. This effect has been experimentally verified in various investigations [82, 9]. Several approaches have been developed for describing evolution of the phase transformations. One of the most classical is given by KOISTINEN AND MARBURGER [45] for a austenite-martensite transformation, see e.g. WOLFF *et al.* [88], MAHNKEN *et al.* [56]. LEBLOND AND DEVAUX [46] propose a model for non-isothermal metallurgical transformations, valid for diffusion controlled transformation such as austenitic transformation, see e.g. [13], [20], [65]. The isothermal diffusive phase transformation is well described by the Johnson-Mehl-Avrami-Kolmogorov kinetics, see e.g. [10], [43] for concerning the multi-phase case. MAIER AND AHRENS [60] study the isothermal austenite-bainite transformation in low alloy steels.

Transformation induced plasticity (TRIP) can be explained as the "... significantly increased plasticity during a phase change. For an externally applied load for which the corresponding equivalent stress is small compared to the normal yield stress of the material, plastic deformation occurs ...", See Fischer *et al.* [24]. Several macroscopic constitutive models have been proposed for modelling of a TRIP-strain, most of them are based on the approach of LEBLOND *et al.* [46]. More recent models taking TRIP into account – in which martensite formation has been studied extensively – are presented, e.g. in ANTRETTER *et al.* [6], IDESMAN *et al.* [38], WOLFF *et al.* [86, 87, 88, 89], and HALLBERG *et al.* [32], amongst others.

Extended continuum mechanics: *Extended continuum models* or (*generalized continua*, [63]) have been developed in the last century to account for size effects on the material's response. GURTIN [31] formulates a phase field model within a continuum

3

thermodynamic framework, where microforces associated with an order parameter and its first gradient are introduced. Based on additional degrees of freedom and generalized stresses, FOREST *et al.*[27] describe a thermodynamic consistent phase field model, which is extended with gradient terms. It is shown, that there are strong links between generalized continuum mechanics and phase field models which are striving in modern field theories of materials.

White layer and hardness dependency: As shown in Figure 4.1, high speed cutting can change material structure in workpiece surfaces in which white and dark layers are induced due to the intense, localized, rapid thermal-mechanical loading. UMBRELLO [82] and ATTANASIO [9] show that the white layer and the dark layer consist of untempered and overtempered martensite, respectively. Due to the rapid mechanical loading and high local temperature in high speed cutting, the initial material state martensite transforms into austenite and due to quenching retransforms back to martensite. That is how the white layer forms. RAMESH AND MELKOTE [69] predicted the thickness of white layer taking into account the effects of stress and strain on phase transformation temperatures, where martensitic phase transformation accompanied by the TRIP effect was considered. GUO *et al.* [30] study the influence of hardness of the material DIN 100Cr6 on material behavior under tension and find out that the yield stress and tensile strength increase or decrease following a change of hardness. To describe this relationship, UMBRELLO *et al.* [80] propose a linear hardness-dependent function, which can be integrated into a flow function. UMBRELLO *et al.* [82] study the hardness of the white layer, and find that it is harder than the bulk material. They propose an empirical function, which takes the white layer formation and the influence of maximal reached temperature into account, to describe the hardness modification.

1.3 Goals

Considering the effects mentioned in Section 1.2 on the state of the art, we intend to process the following goals in the experiments and the related thermodynamic simulations:

1. Experimental goals:

   a) Investigation of mechanical high speed tests under tension, compression and shear at different strain rates and temperatures for identifying the SD-effect related to visco-plasticity

   b) Investigation of dilatometer tests for identifying phase transformations and TRIP-strains

   c) Investigation of further mechanical tests using different hardened specimens under tension, compression and shear for identifying the hardness dependence

2. Goals for simulations:

   a) Development of a multi-mechanism model (MMM) for strain rate and temperature dependent asymmetric visco-plastic material behavior based on the Johnson-Cook model

b) In the special scenario of hard turning with AISI 52100, we have martensite as initial phase, which transforms into austenite due to high thermal loading and retransforms back to martensite due to rabid cooling. The TRIP-strains for both transformations are also taken into account

c) Replacing Johnson-Cook rate form with Huh-Kang rate form and applying it for different stress modes such as tension, compression and shear

d) Extension of the MMM with the gradient of the austenite phase fraction based on the concept of generalized stresses for consideration of the size effect

e) Extension of the model with asymmetric hardness dependency and description of the hardness modification with a empirical function

f) Identification of material parameters by comparing the experimental and simulated data using a least-squares functional as an identification criterion

g) Testing the model and studying the characteristic effects with cutting simulations by using the finite-element program ABAQUS: I. Implementation of the MMM as a user-defined material subroutine for explicit calculation (VUMAT). II. Implementation of the extended MMM as a user-defined element subroutine for explicit calculation (VUEL) by treating the austenite phase fraction as an extra degree of freedom.

1.4 Structure

In **Chapter 2** we will present the kinematics for continuum mechanics in the framework of thermodynamics at large strains. Then we will introduce a multi-phase system concerning volume changes due to pressure, temperature and phase fraction. At the end of this Chapter we will introduce the balance equations for linear momentum, energy and entropy.

In **Chapter 3** a multi-mechanism model (MMM) will be formulated in a thermodynamic framework for large deformations taking elasticity, thermal effect, visco-plasticity, asymmetric effect, phase transformations and TRIP-strains into account. The derivation of a prototype model will be started by defining a specific Helmholz energy, which contains an elastic part, a thermal part and a plastic part as well as a chemical part. Then we will define the thermodynamic forces and the evolution equations according to the following items:

- Based on the classical Johnson-Cook model, which considers strain hardening, temperature dependence and strain rate dependence, a yield function of Johnson-Cook type will be formulated. Here, the strain hardening will be replaced by a combination of non-linear and linear isotropic hardening. The linear strain rate form will be improved by the Huh-Kang strain rate form, which allows a quadratic description of the Strength in relation to the logarithm of strain rate. All parameters of the yield function will be weighted by the weighting functions to consider the

SD-effect representing different material behaviors due to different stress modes such as tension, compression and shear.

- A flow rule for transformation plasticity will be introduced based on the approach due to Leblond [47]. The rule considers two phase transformations, austenitization and martensitic retransformation. For the evolution of the austenite phase we suppose a simple approach due to Leblond *et al.* [46]. For the retransformation we use a rate form of the Koistinen-Marburger approach.

Furthermore, we will prove the thermodynamic consistency of the bulk model. Moreover, a numerical implementation will be introduced. For identifying the parameters high speed mechanical tests and dilatometer tests will be investigated. At last, the model will be implemented as a user defined material VUMAT-subroutine and linked to the commercial FEM-software ABAQUS for cutting simulations.

In **Chapter 4** we will extend the above MMM with a phase gradient term based on the concept of generalized stresses as proposed by GURTIN [31] and FOREST [27]. To this end, a chemical variable, representing the austenite mass fraction, will be treated as an extra degree of freedom for FEM, and its first gradient will be involved. In a thermodynamic framework we will derive the balance equations in association with the generalized stresses using the principle of virtual power. Analogously to the formulations in Chapter 3 we will specialize the Helmholz energy and derive a prototype model, where the chemical free energy is extended by a gradient energy. In comparison to the model in Chapter 3 we will also consider asymmetric hardness dependency and hardness modification due to white layer formation besides the extension with gradient term. Moreover, the thermodynamic consistency of the bulk model will be also proved. In a further part of this chapter we will investigate more mechanical tests in relation to the hardness dependency in order to identify the hardness dependency. Finally, we will investigate some cutting simulations, where the model is implemented as a user defined element VUEL-subroutine and linked to ABAQUS.

Notations

Square brackets [●] are used throughout the paper to denote 'function of' in order to distinguish from mathematical groupings with parenthesis (●).

Chapter 2

Basic equations for continuum mechanics and volume changes for a multi-phase system

This chapter summarize the basic equations for continuum mechanics and basic relations for a multi-phase system, which are relevant for formulation of the multi-mechanism model in a thermodynamic framework in next chapters. The kinematic relations are described for a continuum body. The description is based on the multiplicative decomposition of the deformation gradient into inelastic, elastic, thermal and multiphase-transformational parts. Using the assumption that individual phase densities are dependent on the pressure, the temperature and phase fractions an additive decomposition for the Jacobian of the deformation gradient is derived. Furthermore, we will calculate volume changes due to the pressure, the temperature and phase fractions for a multi-phase system. At the end of this chapter, the balance equations for linear momentum, energy and entropy are introduced.

2.1 Kinematics

We consider a continuum body in the reference (initial) configuration $\mathcal{B}_0 \subset \mathcal{E}^3$ within the Euclidian space $\mathcal{E}^3$. Material particles are labelled by a vector $\mathbf{X}$. We introduce a time domain $\mathcal{T} = [0, T] \subset I\!\!R_+$, where time simply provides a history parameter in order to label the sequence of events and quasi-static conditions. The current placement at time t is associated with the mapping $\boldsymbol{\varphi}$. Then, for $\mathbf{X}$ we introduce

$$1.\ \mathbf{x} = \boldsymbol{\varphi}[\mathbf{X}, t], \qquad 2.\ \mathbf{F} = \nabla\boldsymbol{\varphi}[\mathbf{X}, t], \qquad 3.\ J = \det \mathbf{F} \qquad (2.1)$$

where $\mathbf{x}$ is the placement vector of the related particle at the current configuration $\mathcal{B}$ and $\mathbf{F}$ is the deformation gradient, which is known to be a mixed-variant tensor. J is the Jacobian of $\mathbf{F}$.

The deformation gradient $\mathbf{F}$ is used for the transformation of line elements $d\mathbf{x}$, $d\mathbf{X}$ as well as area elements $d\mathbf{a}$, $d\mathbf{A}$ and also for volume elements dv, dV. Therefore

$$1.\ d\mathbf{x} = \mathbf{F}d\mathbf{X}, \qquad 2.\ d\mathbf{a} = J\mathbf{F}^{-t}d\mathbf{A}, \qquad 3.\ dv = JdV, \qquad (2.2)$$
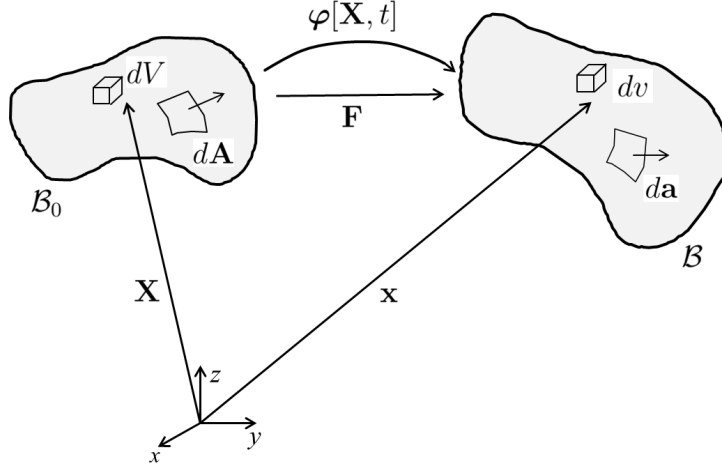
Figure 2.1: Mapping and transformation of the continuum body

as illustrated in Figure 2.1.

The second order deformation gradient can be split multiplicatively as

$$1.\ \mathbf{F} = \mathbf{F}^{\mathrm{vol}} \cdot \mathbf{F}^{\mathrm{iso}} = \mathbf{F}^{\mathrm{iso}} \cdot \mathbf{F}^{\mathrm{vol}}, \qquad \text{where} \qquad 2.\ \mathbf{F}^{\mathrm{vol}} = J^{1/3}\mathbf{1}. \tag{2.3}$$

Note, that the tensors $\mathbf{F}^{\mathrm{vol}}$ and $\mathbf{F}^{\mathrm{iso}}$ are interchangeable in Eq.(2.3.1), which is due to the property $\mathbf{A} \cdot \mathbf{1} = \mathbf{1} \cdot \mathbf{A}$, $\forall \mathbf{A}$ for the second order unit tensor $\mathbf{1}$ occuring in Eq.(2.3.2). By construction, $\mathbf{F}^{\mathrm{iso}}$ and $\mathbf{F}^{\mathrm{vol}}$ represent isochoric and volumetric deformations, respectively. For the scenario of phase-transformation coupled to thermo-elasto-visco-plasticity both quantities are split further based on the following assumptions:

1. the elastic deformation is both volumetric and isochoric, represented by J_e and $\mathbf{F}^{\mathrm{iso}}_e$,

2. the thermal deformation is purely volumetric, represented by J_θ,

3. the transformational deformation is purely volumetric, represented by J_z,

4. the plastic deformation is purely isochoric, represented by $\mathbf{F}_i$,

5. there exists a stress free isochoric intermediate configuration.

From the above 5 assumptions we conclude the following decompositions of the isochoric and volumetric part of the deformation gradient:

$$\begin{aligned} &1.\ \mathbf{F}^{\mathrm{iso}} = \mathbf{F}^{\mathrm{iso}}_e \cdot \mathbf{F}_i \\ &2.\ J \quad = J_e \cdot J_\theta \cdot J_z \quad \implies \quad \mathbf{F}^{\mathrm{vol}} = (J_e \cdot J_\theta \cdot J_z)^{1/3}\mathbf{1}. \end{aligned} \tag{2.4}$$

8

Remarks 2.1

1. Note, that due to assumption 2 we do not have to distinguish between total and isochoric contributions for the inelastic part $\mathbf{F}_i$.

2. The tensors $\mathbf{F}_e^{\text{iso}}$ and $\mathbf{F}_i$ in Eq.(2.4.1) are not interchangeable, which is due to the above assumption 5.

3. Clearly, the scalar terms in J_e, J_θ and J_i in Eq.(2.4.1) are interchangeable.

4. Following LEVITAS *et al.* [48] the inelastic part $\mathbf{F}_i$ is closely related to both, visco-plasticity and phase transformation, see also HALLBERG *et al.* [32].

Inserting Eq.(2.4.1) and Eq.(2.4.2) into Eq.(2.3.1) renders

$$\mathbf{F} = J^{1/3}\mathbf{F}_e^{\text{iso}} \cdot \mathbf{F}_i = (J_e \cdot J_\theta \cdot J_z)^{1/3}\mathbf{F}_e^{\text{iso}} \cdot \mathbf{F}_i. \tag{2.5}$$

From the first part of this relation we derive

1. $\mathbf{F}_e = J_e^{1/3}\mathbf{F}_e^{\text{iso}}$,   2. $\mathbf{F}_e^{-1} = J_e^{-1/3}(\mathbf{F}_e^{\text{iso}})^{-1}$,   3. $\dot{\mathbf{F}}_e = \dfrac{1}{3J_e^{2/3}}\mathbf{F}_e^{\text{iso}}\dot{J}_e + J_e^{1/3}\dot{\mathbf{F}}_e^{\text{iso}}$,   (2.6)

where the dot above the argument represents the derivative with respect to time t. The time derivatives of the volumetric and isochoric contributions in Eq.(2.4) are

1. $\dot{\mathbf{F}}^{\text{iso}} = \dot{\mathbf{F}}_e^{\text{iso}} \cdot \mathbf{F}_i + \mathbf{F}_e^{\text{iso}} \cdot \dot{\mathbf{F}}_i$.   2. $\dot{\mathbf{F}}^{\text{vol}} = \dfrac{1}{3J^{2/3}}\dot{J}\mathbf{1}$,   (2.7)

and consequently from Eq.(2.5) one obtains

$$\dot{\mathbf{F}} = \left(\frac{1}{3J^{2/3}}\dot{J}\mathbf{F}_e^{\text{iso}} + J^{1/3}\dot{\mathbf{F}}_e^{\text{iso}}\right)\mathbf{F}_i + J^{1/3}\mathbf{F}_e^{\text{iso}} \cdot \dot{\mathbf{F}}_i. \tag{2.8}$$

With this result and the inverse from Eq.(2.5)

$$\mathbf{F}^{-1} = J^{-1/3}(\mathbf{F}_i)^{-1} \cdot (\mathbf{F}_e^{\text{iso}})^{-1} \tag{2.9}$$

the velocity gradient with respect to the actual configuration is

$$\mathbf{l} = \dot{\mathbf{F}} \cdot \mathbf{F}^{-1} = \frac{1}{3}\frac{d}{dt}(\ln J)\mathbf{1} + \dot{\mathbf{F}}_e^{\text{iso}} \cdot \mathbf{F}_e^{\text{iso}\,-1} + \mathbf{F}_e^{\text{iso}} \cdot \dot{\mathbf{F}}_i \cdot \mathbf{F}_i \cdot (\mathbf{F}_e^{\text{iso}})^{-1}, \tag{2.10}$$

where the relation $\dot{J}/J = d(\ln J)/dt$ has been used. An elastic pull back renders a velocity gradient with respect to the intermediate configuration $\bar{\mathcal{B}}$

$$\bar{\mathbf{L}} := \mathbf{F}_e^{-1} \cdot \mathbf{l} \cdot \mathbf{F}_e = (\mathbf{F}_e^{\text{iso}})^{-1} \cdot \mathbf{l} \cdot \mathbf{F}_e^{\text{iso}} = \frac{1}{3}\frac{d}{dt}(\ln J)\mathbf{1} + \mathbf{F}_e^{\text{iso}\,-1} \cdot \dot{\mathbf{F}}_e^{\text{iso}} + \dot{\mathbf{F}}_i \cdot \mathbf{F}_i. \tag{2.11}$$

By use of

$$\ln J = \ln J_e + \ln J_\theta + \ln J_z \tag{2.12}$$

and Eq.(2.6.1) we obtain the following additive decomposition

1. $\bar{\mathbf{L}} := \bar{\mathbf{L}}_e + \bar{\mathbf{L}}_i + \bar{\mathbf{L}}_\theta + \bar{\mathbf{L}}_z,$ where

2. $\bar{\mathbf{L}}_e := \mathbf{F}_e^{-1} \cdot \dot{\mathbf{F}}_e,$

3. $\bar{\mathbf{L}}_i := \dot{\mathbf{F}}_i \cdot \mathbf{F}_i^{-1} = -\mathbf{F}_i \cdot \dot{\mathbf{F}}_i^{-1},$

4. $\bar{\mathbf{L}}_\theta := \dfrac{1}{3}\dfrac{d}{dt}(\ln J_\theta)\mathbf{1},$

5. $\bar{\mathbf{L}}_z := \dfrac{1}{3}\dfrac{d}{dt}(\ln J_z)\mathbf{1}.$

(2.13)

Consequently $\bar{\mathbf{L}}_e$, $\bar{\mathbf{L}}_i$, $\bar{\mathbf{L}}_\theta$, $\bar{\mathbf{L}}_z$, represent respectively the elastic, inelastic, thermal and transformation part. Note, the inelastic velocity gradient $\bar{\mathbf{L}}_i$ in Eq.(2.13.3) can also be obtained as

$$\bar{\mathbf{L}}_i = -\frac{1}{2}\mathcal{L}_i^\sharp[\overline{\mathbf{G}}^\sharp] \cdot \overline{\mathbf{G}}^\flat$$

(2.14)

by use of the Lie derivative operator $\mathcal{L}_i^\sharp[\bullet] = {}_*\Phi_i^\sharp\left[\left[{}^*\Phi_i^\sharp[\bullet]\right]\right]$, where ${}^*\Phi_i^\sharp$ is explained in Eq.(A.2.1) and ${}_*\Phi_i^\sharp$ denotes its inverse operation. The notation $\dot{[.]}$ denotes the time derivative.

Furthermore, alternative mixed-variant representations of the inelastic velocity gradient relative to the configurations $\mathcal{B}$, $\mathcal{B}_0$ can be expressed as

1. $\mathcal{B}:$ $\mathbf{l}_i = {}_*\Phi_e^{\backslash}[\bar{\mathbf{L}}_i] = \mathbf{F}_e \cdot \bar{\mathbf{L}}_i \cdot \mathbf{F}_e^{-1} = -\dfrac{1}{2}\mathcal{L}^\sharp[\mathbf{b}_e] \cdot \mathbf{b}_e^{-1}$

2. $\mathcal{B}_0:$ $\mathbf{L}_i = {}^*\Phi_i^{\backslash}[\bar{\mathbf{L}}_i] = \mathbf{F}_i^{-1} \cdot \bar{\mathbf{L}}_i \cdot \mathbf{F}_i = -\dfrac{1}{2}\dot{\mathbf{C}}_i^{-1} \cdot \mathbf{C}_i.$

(2.15)

An elastic push-forward ${}_*\Phi_e^{\backslash}[\bullet] = \mathbf{F}_e \cdot [\bullet] \cdot \mathbf{F}_e^{-1}$ of Eq.(2.14) renders the relation (2.15.1), Here $\mathbf{b}_e$ is introduced in Eq.(A.2). Furthermore the Lie derivative operator $\mathcal{L}^\sharp[\bullet] = {}_*\Phi^\sharp\left[\left[{}^*\Phi^\sharp[\bullet]\right]\right]$ has been used, where ${}^*\Phi^\sharp$ is explained in Eq.(A.2.1) and ${}_*\Phi^\sharp$ denotes its inverse operation. The flow rule (2.15.2) w.r.t. the reference configuration is a consequence of a inelastic pull-back ${}^*\Phi_i^{\backslash}[\bullet] = \mathbf{F}_i^{-1} \cdot (\bar{\bullet}) \cdot \mathbf{F}_i$ of the flow rule Eq.(2.14).

2.2 Volume changes due to pressure, temperature and phase fraction

Let us consider a mixture of $n_z \geq 2$ phases (constituents) fulfilling a volume differential dV and having a mass differential dm at the reference configuration. We assume that the mixture is homogeneous, i.e. all phases are equally distributed. The (bulk) densities ρ_0 and ρ of the mixture with respect to the reference and the current configurations are respectively defined as

1. $\rho_0 = \dfrac{dm}{dV},$ 2. $\rho = \dfrac{dm}{dv}.$

(2.16)

Within the volume dv, let the ith phase have its volume dv_i and its mass dm_i. The volume phase fraction $z_i^{(v)}$, the mass phase fraction z_i and the density of the ith phase

are defined by

$$1. \quad z_i^{(v)} = \frac{dv_i}{dv}, \qquad 2. \quad z_i = \frac{dm_i}{dm}, \qquad 3. \quad \rho_i = \frac{dm_i}{dv_i}. \qquad (2.17)$$

Generally, the mixture is not (spatially) homogeneous. Based on (2.16) and (2.17), the quantities ρ, $z_i^{(v)}$, z_i and ρ_i are defined at a body point $\mathbf{X} \in \mathcal{B}_0$ by a limit process with volumes contracting to this point. We assume that such limit process is possible. Thus, these quantities are functions of space, and, clearly, of time. Obviously, the following balances are valid at all body points and for all times,

$$1. \quad \sum_{i=1}^{n_z} z_i^{(v)} = 1, \quad 2. \quad \sum_{i=1}^{n_z} z_i = 1, \quad 3. \quad z_i^{(v)} \geq 0, \quad 4. \quad z_i \geq 0 \quad \text{for all } i = 1, \dots, n_z.$$

$$(2.18)$$

The mass dm_i included in a fixed volume does not depend on possible volume changes due to temperature or strain changes. Thus, the mass phase fractions z_i in Eq.(2.17.2) have the advantage to be independent of temperature and deformation. Moreover, from (2.16) and (2.17) a relation between mass and volume phase fractions follows (for all admissible temperatures θ and pressures p)

$$z_i = \frac{\rho_i[\theta, p]}{\rho[\theta]} z_i^{(v)}[\theta, p] \qquad \text{for all } i = 1, \dots, n_z, \qquad (2.19)$$

as well as the following mixture rules for the bulk density ρ and its inverse are valid

$$1. \quad \rho = \sum_{i=1}^{n_z} \rho_i \, z_i^{(v)}, \qquad 2. \quad \frac{1}{\rho} = \sum_{i=1}^{n_z} \frac{1}{\rho_i} \, z_i. \qquad (2.20)$$

We remark that some of the formulas derived above can also be found in RANIECKI and BRUHNS [68]. We also remark, that fortunately, due to the small differences of the densities of the steel phases (at the same temperature), the difference between mass and volume fractions ("absolute error") is less than 0.02. The relative error is less than 4.5% in *unfavorable* cases, see [58].

Inserting the relations (2.16) into Eq.(2.1.3) and regarding the multiplicative decomposition of the deformation gradient in Eq.(2.4.2) renders

$$J = \frac{dv}{dV} = \frac{\rho_0}{\rho} = J_e \cdot J_\theta \cdot J_z, \qquad (2.21)$$

where $J_e = \det \mathbf{F}_e$, $J_\theta = \det \mathbf{F}_\theta$, $J_z = \det \mathbf{F}_z$, respectively are elastic, thermal and transformation parts.

We assume that the volume dV will be changed by a density change induced by pressure change $p - p_0$, temperature change $\theta - \theta_0$ and/or by and phase fraction change $\underline{z} - \underline{z}_0$, leading to a new volume dv with a new density ρ. Let ρ be a function of pressure p, absolute temperature θ and of mass phase fractions $\underline{z}$ with reference value

$\rho_0 = \rho[p_0, \theta_0, \underline{z}_0]$. Upon defining a state vector $\underline{s} = [p, \theta, \underline{z}]$, a Taylor extension up to the first-order terms yields

$$J = \frac{\rho_0}{\rho} \approx 1 - \frac{1}{\rho_0} \frac{\partial \rho}{\partial p}\bigg|_{\underline{s}_0} (p - p_0) \quad - \frac{1}{\rho_0} \frac{\partial \rho}{\partial \theta}\bigg|_{\underline{s}_0} (\theta - \theta_0) - \frac{1}{\rho_0} \sum_{i=1}^{n_z} \frac{\partial \rho}{\partial z_i}\bigg|_{\underline{s}_0} (z_i - z_{0i}). \quad (2.22)$$

Using the mixture rule for the inverse density in (2.20) and rearranging, the relation (2.22) gives

$$\begin{aligned}
J = \frac{\rho_0}{\rho} \approx 1 \quad & - \sum_{i=1}^{n_z} \frac{\rho_0 z_{0i}}{\rho_i[p_0, \theta_0]} \left(\frac{1}{\rho_i[p_0, \theta_0]} \frac{\partial \rho_i}{\partial p}[p_0, \theta_0] \right) (p - p_0) \\
& + \sum_{i=1}^{n_z} \frac{\rho_0 z_{0i}}{\rho_i[p_0, \theta_0]} \left(-\frac{1}{\rho_i[p_0, \theta_0]} \frac{\partial \rho_i}{\partial \theta}[p_0, \theta_0] \right) (\theta - \theta_0) \qquad (2.23) \\
& + \sum_{i=1}^{n_z} \frac{\rho_0}{\rho_i[p_0, \theta_0]} (z_i - z_{0i}).
\end{aligned}$$

Using Eq.(2.18) the last summand in Eq.(2.23) can be re-written in accordance with

$$\begin{aligned}
\sum_{i=1}^{n_z} \frac{\rho_0}{\rho_i[p_0, \theta_0]} (z_i - z_{0i}) &= \sum_{i=1}^{n_z} \frac{\rho_0}{\rho_i[p_0, \theta_0]} z_i - \sum_{i=1}^{n_z} z_i^{(v)}[p_0, \theta_0] = \sum_{i=1}^{n_z} \frac{\rho_0}{\rho_i[p_0, \theta_0]} z_i - 1 \\
&= \sum_{i=1}^{n_z} \frac{\rho_0}{\rho_i[p_0, \theta_0]} z_i - \sum_{i=1}^{n_z} z_i = \sum_{i=1}^{n_z} \left(\frac{\rho_0}{\rho_i[p_0, \theta_0]} - 1 \right) z_i.
\end{aligned} \quad (2.24)$$

Defining the isothermal compressibility of the ith phase $\kappa_i[p_0, \theta_0]$, the bulk compressibility κ, the heat-dilatation coefficient of the ith phase $\alpha_i[p_0, \theta_0]$, the bulk heat-dilatation coefficient α and the mass phase-dilatation coefficient β_{m_i} of the ith phase (all related to the reference pressure p_0, to the reference temperature θ_0 and to the reference phase mixture $z_0^{(v)}$) by

$$\begin{aligned}
\kappa[\underline{s}_0] &:= \sum_{i=1}^{n_z} \frac{\rho_0 z_{0i}}{\rho_i[p_0, \theta_0]} \kappa_i[p_0, \theta_0], & \kappa_i[p_0, \theta_0] &:= \frac{1}{\rho_i[p_0, \theta_0]} \frac{\partial \rho_i}{\partial p}[p_0, \theta_0], \\
\alpha[\underline{s}_0] &:= \sum_{i=1}^{n_z} \frac{\rho_0 z_{0i}}{\rho_i[p_0, \theta_0]} \alpha_i[p_0, \theta_0], & \alpha_i[p_0, \theta_0] &:= -\frac{1}{3\rho_i[p_0, \theta_0]} \frac{\partial \rho_i}{\partial \theta}[p_0, \theta_0] \qquad (2.25) \\
\underline{\beta}[p_0, \theta_0] &:= [\beta_1, ..., \beta_{n_z}]^T, & \beta_i[p_0, \theta_0] &:= \frac{1}{3} \left(\frac{\rho_0}{\rho_i[p_0, \theta_0]} - 1 \right),
\end{aligned}$$

a compact form of Eq.(2.23) is

$$J \approx 1 - \kappa[\underline{s}_0](p - p_0) + 3\alpha[\underline{s}_0](\theta - \theta_0) + 3\underline{\beta}^T[p_0, \theta_0]\underline{z}, \qquad (2.26)$$

and where the numbers 3 have been introduced for convenience. Next, assuming the approximation $J - 1 \approx \ln J$ for small elastic, thermal and transformation strains, the multiplicative form (2.21) can be transformed by use of (2.26) into the following additive form

$$\begin{aligned}
\ln J &= \ln J_e + \ln J_\theta + \ln J_z \\
&\approx -\kappa[\underline{s}_0](p - p_0) + 3\alpha[\underline{s}_0](\theta - \theta_0) + 3\underline{\beta}^T[p_0, \theta_0]\underline{z}.
\end{aligned} \qquad (2.27)$$

In order to take experimental findings into account, we let κ depend on θ in forthcoming considerations.

12

2.3 Stress tensors

Due to different stretch tensors, some are given in Section A2, suitable stress tensors must be defined related to the reference configuration $\mathcal{B}_0$ and the current configuration $\mathcal{B}$. Both configurations are introduced in Section 2.1. The Cauchy-stress tensor $\boldsymbol{\sigma}$ represents the true stress in the current configuration. Another important stress tensor is the Kirchhoff-stress tensor

$$\boldsymbol{\tau} := J\boldsymbol{\sigma}, \tag{2.28}$$

where J is the Jacobian defined in Eq.(2.1). According to the approach

$$
\begin{aligned}
&1. \quad \mathbf{t}_c d\mathbf{a} = \mathbf{t}d\mathbf{A}, \quad \text{where} \\
&2. \quad \mathbf{t}_c := \boldsymbol{\sigma}\mathbf{n}, \quad 3. \ \mathbf{t} := \mathbf{P} \cdot \mathbf{N},
\end{aligned}
\tag{2.29}
$$

more stress tensors can be derived. Here $\mathbf{t}_c$ and $\mathbf{t}$ are the macro traction vector related to the current and the reference configuration, respectively. $\mathbf{n}$ and $\mathbf{N}$ are the outer unit normals related to the current and the reference configuration, respectively. Using Eq.(2.2) and Eq.(2.29) the asymmetric first Piola-stress tensor reads

$$\mathbf{P} = J\boldsymbol{\sigma}\mathbf{F}^{-t} = \boldsymbol{\tau}\mathbf{F}^{-t}. \tag{2.30}$$

Furthermore, a material symmetric stress tensor $\mathbf{S}$, which is named as second Piola-stress tensor, can be calculated from the transformation $\mathbf{S} = \mathbf{F}^{-1}\mathbf{P}$ as

$$\mathbf{S} = J\mathbf{F}^{-1}\boldsymbol{\sigma}\mathbf{F}^{-t} = \mathbf{F}^{-1}\boldsymbol{\tau}\mathbf{F}^{-t} = {}_*\Phi^{\sharp}[\boldsymbol{\tau}]. \tag{2.31}$$

Here, ${}_*\Phi^{\sharp}$ denotes full push-forward operation of contra-variant tensor objects introduced in Section A2.

Furthermore, we define a density of internal power $p^{(i)}$, which can be expressed as

$$p^{(i)} = \mathbf{P} : \dot{\mathbf{F}} = \mathbf{S} : \dot{\mathbf{E}} = \boldsymbol{\tau} : \mathbf{d} = \overline{\mathbf{M}} : \bar{\mathbf{L}}. \tag{2.32}$$

$\mathbf{E}$ is the Green strain tensor given in Eq.(A.5). $\mathbf{d}$ is defined in Eq.(A.7.2). The Mandel stress $\overline{\mathbf{M}}$ and the velocity gradient $\bar{\mathbf{L}}$ (Eq.(2.13)) are a dual paring of conjugate stress and strain-rate tensor quantities with respect to a intermediate configuration $\bar{\mathcal{B}}$, where

$$\overline{\mathbf{M}} = \mathbf{F}_e^t(\mathbf{P}\mathbf{F}^t)\mathbf{F}_e^{-t}. \tag{2.33}$$

$\mathbf{F}_e$ is the elastic part of the deformation gradient $\mathbf{F}$ introduced in Eq.(2.6.1).

2.4 Balance equations

In macroscopic modeling of steel behavior, the material is usually regarded as a coexisting mixture of its phases (i.e. constituents). In contrast to general mixtures, the phases do not diffuse. Here, we assume a constant (macroscopic) carbon content.

Using balance relations in a material representation with respect to the reference configuration $\mathcal{B}_0$ we have, see e.g. HAUPT [34]

1. $$\rho_0\,\ddot{\mathbf{u}} - \mathbf{P}\cdot\nabla \;= \mathbf{f}\;\text{ in }\mathcal{B}_0, \qquad\qquad\text{(linear momentum)}$$

2. $$\rho_0\,\dot{\epsilon} + \nabla\cdot\mathbf{q}_0 \;= p^{(i)} + \rho_0\,r_\theta\;\text{ in }\mathcal{B}_0,\;\;\text{(energy)} \qquad (2.34)$$

3. $$-\rho_0\,\dot{\Psi} - \rho_0\,\dot{\theta}\,\eta + p^{(i)} - \frac{1}{\theta}\,\mathbf{q}_0\cdot\nabla\theta \;\geq 0\;\text{ in }\mathcal{B}_0. \qquad\text{(entropy)}$$

In addition to the above notations we use: ρ_0 - density in the reference configuration, $\mathbf{f}$ - body force, ϵ - special internal energy, $\mathbf{q}_0$ - heat-flux density vector, r_θ - mass density of heat supply, Ψ - Helmholz energy. $p^{(i)}$ is the density of internal power defined in Eq.(2.32) in the classic continuum mechanics and will be extended in Chapter 4 due to the concept of generalized stresses. The dot above the argument denotes its time derivative. We also recall, that the inequality (2.34.3) is known as the *Clausius-Duhem inequality.*

These equations are completed by the boundary and initial conditions for the displacement vector $\mathbf{u}$ and for the temperature θ as

$$\begin{array}{llll}
\mathbf{u}[\mathbf{X},0]=0, & \dot{\mathbf{u}}[\mathbf{X},0]=0, & \theta[\mathbf{X},0]=\theta_0=\text{const.} & \text{for }\mathbf{X}\in\mathcal{B}_0,\\
\mathbf{u}=0 & \text{on }\partial\mathcal{B}_0^u\times]0,T[, & \mathbf{P}\cdot\mathbf{N}=\bar{\mathbf{t}} & \text{on }\partial\mathcal{B}_0^\mathbf{P}\times]0,T[, \;\;(2.35)\\
\theta=\bar{\theta} & \text{on }\partial\mathcal{B}_0^\theta\times]0,T[, & \mathbf{q}_0\cdot\mathbf{N}=\bar{\mathbf{q}} & \text{on }\partial\mathcal{B}_0^q\times]0,T[.
\end{array}$$

For convenience we take zero initial values for $\mathbf{u}$ and $\dot{\mathbf{u}}$ as well as a constant for θ. Without loss of generality we take zero values for $\mathbf{u}$ at $\partial\mathcal{B}_0^u\times]0,T[$. $\bar{\mathbf{t}}$ is a given load on $\partial\mathcal{B}_0^\mathbf{P}$, $\bar{\theta}$ a prescribed temperature on $\partial\mathcal{B}_0^\theta$ and $\bar{\mathbf{q}}$ a given heat flux through the remaining boundary part $\partial\mathcal{B}_0^q$.

Furthermore, following Eq.(2.34.1) and Eq.(2.29.3) one obtains the classical local static equilibrium and the associated boundary condition as

$$1.\;\;\mathbf{P}\cdot\nabla + \mathbf{f} = \mathbf{0}\;\text{ in }\mathcal{B}_0,\;\;2.\;\;\mathbf{t} = \mathbf{P}\cdot\mathbf{N}\;\text{ on }\partial\mathcal{B}_0^\mathbf{P}, \qquad (2.36)$$

where the term $\rho_0\,\ddot{\mathbf{u}}$ in Eq.(2.34.1) is not considered for a local formulation.

Chapter 3

A multi-mechanism model for cutting simulations combining visco-plastic asymmetry and TRIP

3.1 Introduction

High speed cutting can change material structures in workpiece surfaces in which white and dark layers are induced due to the intense, localized, rapid thermal-mechanical loading. Extended experimental tests for high strength steels exhibit different behaviors for different loading types such as tension, compression and shear. In this chapter we formulate a multi-mechanism model for cutting simulations taking the following items into account.

Inelastic asymmetry: The so-called stress mode angle, or Lode angle is often used to detect the asymmetric effect, which is expressed in terms of the ratio of the second and third invariant of the deviatoric stress tensor. In [50] it is used to introduce the *concept of weighting functions* with the goal to model creep with asymmetric effects. In this chapter, our objective is to extend the well known Johnson-Cook model [44] with the concept of weigthing functions, in order to account for asymmetric effects within a large strain framework. To this end, a rate independent flow factor with a rate dependent Johnson-Cook type yield function is introduced. The basic idea is the weighting of stress mode dependent material parameters related to visco-plasticity with the above mentioned functions. Here an additive decomposition of the inelastic strain rate is assumed, where each of the related quantities incorporates weighting functions dependent on the stress mode angle.

The advantage of this approach is, that certain (though not all) material parameters, can be obtained individually from specific loading modes such as tension, compression and shear, investigated experimentally in the laboratory.

Inelastic asymmetry applied to quadratic rate dependence: Most materials show a bi-linear dependence of strength on the logarithm of the strain rate [37, 71] including our investigated material AISI 52100. The original Johnson-Cook rate form provides a linear dependence of the strength on the logarithm of strain rate. In order to get a better approach we will use a varied strain-rate form due to HUH-KANG [37] to describe a quadratic strain-rate dependency. The asymmetry of this dependency is analogously

considered by weighting the material parameters with the stress mode related weighting functions.

Phase transformation: High temperatures also result into phase transformations. In order to make our approach as general as possible, in this chapter we will present a general thermodynamic framework for multi-phase transformation with arbitrary initial phases. Then, in the prototypical situation of our study, the following two phase transformations are taken into account:

1. Transformation of the martensitic initial state into austenite, then

2. retransformation to martensite.

In view of the large heating rate and the relatively high austenitizing temperature, the transformation of the martensite into austenite is described by an approach due to LEBLOND and DEVAUX [46] and the retransformation to martensite is taken into account by the classical KOISTINEN-MARBURGER relation [45].

Transformation induced plasticity (TRIP): The irreversible phase transformations (martensite to austenite and the revers) are characterized by crystallographic rearrangements on the atomistic level, cf. TJAHJANTO *et al.* [77]. On the macroscopical level this effect corresponds to irreversible strains (TRIP strains) of the parent phase, even if the material is loaded by a stress state less than the yield stress of the softer phase. Several macroscopic constitutive models have been proposed to simulate the complex interactive mechanisms of phase transformation and plasticity, see e.g. LEBLOND [46], FISCHER *et al.* [24, 25, 26], HALLBERG *et al.* [32], WOLFF *et al.* [88], MAHNKEN *et al.* [56], IWAMOTO *et al.* [42] and to the references therein. Considering micromechanical or multi-scale modeling we refer to CHERKAOUI [18], TURTELTAUB and SUIKER [78], TJAHJANTO *et al.*[77]. It is proved that the TRIP-strain occurs not only at martensitic but also at austenitic transformation. BÖKENHEIDE *et al.* [14] study phase transformations and TRIP-strain of DIN 100Cr6 steel during heating, where the initial material consists of ferrite and carbide. The TRIP during heating with martensite as the initial state is still not studied and this gap will be closed in this chapter. Furthermore, dilatometer tests are performed under heating and stress loadings for identification of the related parameters.

This chapter is organized as follows:

- Section 3.2 presents a thermodynamic framework for combined visco-plasticity and multi-phase transformations at large strains based on the relations in Chapter 2. In a constitutive framework we select the state variables and assume the Helmholz energy concerning elasticity, hardening, transformations and temperature. After defining the thermodynamic forces we split the Clausius-Duhem inequality into a mechanical, a chemical and a thermal part. All these parts must be fulfilled in formulation of the evolution equations in Section 3.3. Furthermore we derive the heat-conduction equation.

- In Section 3.3, a prototype model is derived by applying the thermodynamic framework to a specific Helmholtz free energy function. For incorporation of

visco-plastic asymmetry we introduce a rate independent flow factor with a rate dependent Johnson-Cook type yield function and replace the linear strain rate form with an improved quadratic strain rate form due to Huh-Kang. Furthermore, evolution equations for the phase fractions are formulated. Moreover, we discuss the mathematical structure of the model as a multi-mechanism model in the sense of CAILLETAUD and SAÏ, [15, 70]. Finally, thermodynamic consistency of the proposed model is shown taking multi-phase transformations into account.

- Some aspects of the numerical implementation are given in Section 3.4.

- In the examples in Section 3.5, material parameters are identified for the material AISI 52100, where mechanical and dilatometer tests are performed with respect to asymmetric visco-plasticity and TRIP-strains, respectively. For testing the model and illustrating the characteristic effects some cutting simulations are applied, where the model is implemented as a user-defined material subroutine for explicit calculation (VUMAT) and linked to the commercial FE-software ABAQUS v6.14.

3.2 A thermodynamic framework for asymmetric visco-plasticity and phase transformations

3.2.1 Constitutive framework

Under consideration of cutting processes with phase transformations coupled to thermo-elasto-visco-plasticity state variables are selected as

$$\text{STATE} = \{\overline{\mathbf{C}}_e, \underline{q}, \underline{z}, \theta\}. \tag{3.1}$$

$\overline{\mathbf{C}}_e$ is the elastic right Cauchy–Green tensor given in Eq.(A.3). $\underline{q} = [q_i, \ldots, q_{n_q}]$ is a vector of internal variables for strain hardening. The vector $\underline{z} = [z_1, z_2, \ldots, z_{n_z}]$ introduced in Eq.(2.17), considers the different n_z phases and also plays the role of an internal variable. Therefore, the Helmholtz energy Ψ of Eq.(2.34.3) is assumed as

$$\Psi = \Psi[\overline{\mathbf{C}}_e, \underline{q}, \underline{z}, \theta]. \tag{3.2}$$

There are several possibilities to formulate the stress-power $p^{(i)}$ in Eq.(2.34) as a dual-pairing of conjugate stress and strain-rate tensor quantities as given in Eq.(2.32). Using the additive decomposition of the velocity gradient $\overline{\mathbf{L}}$ in Eq.(2.13.1), Eq.(2.34) and the identity $\partial \Psi / \partial \overline{\mathbf{C}}_e : \dot{\overline{\mathbf{C}}}_e = 2(\overline{\mathbf{C}}_e \cdot \partial \Psi / \partial \overline{\mathbf{C}}_e) : \overline{\mathbf{L}}_e$ the Clausius-Duhem inequality (2.34.3) – with quantities with respect to the intermediate configuration $\overline{\mathcal{B}}$ introduced in Section 2.3 – reads as

$$\left(\overline{\mathbf{M}} - \rho_0 2 \overline{\mathbf{C}}_e \cdot \frac{\partial \Psi}{\partial \overline{\mathbf{C}}_e} \right) : \overline{\mathbf{L}} - \left(\eta + \frac{\partial \Psi}{\partial \theta} \right) \dot{\theta} + \rho_0 2 \overline{\mathbf{C}}_e \cdot \frac{\partial \Psi}{\partial \overline{\mathbf{C}}_e} : \overline{\mathbf{L}}_i$$
$$- \rho_0 \frac{\partial \Psi}{\partial \underline{q}} \dot{\underline{q}} - \rho_0 \frac{\partial \Psi}{\partial \underline{z}} \dot{\underline{z}} - \frac{1}{\theta} \mathbf{q}_0 \cdot \nabla \theta \geq 0. \tag{3.3}$$

Next, we define thermodynamic forces $\underline{Q} = [Q_1, Q_2, \ldots, Q_{n_q}]^T$ and $\underline{Z} = [Z_1, Z_2, \ldots, Z_{n_z}]^T$:

$$1.\ \overline{\mathbf{M}} = \rho_0 2\overline{\mathbf{C}}_e \cdot \frac{\partial \Psi}{\partial \overline{\mathbf{C}}_e}, \qquad 2.\ \eta = -\frac{\partial \Psi}{\partial \theta}, \qquad 3.\ \underline{Q} = \rho_0 \frac{\partial \Psi}{\partial \underline{q}}, \qquad 4.\ \underline{Z} = \rho_0 \frac{\partial \Psi}{\partial \underline{z}}. \quad (3.4)$$

The thermodynamic forces Q_i are called hardening stresses and the quantities Z_i are named chemical forces. The relations (3.4.1-2) result from the Clausius-Duhem inequality by standard arguments, see e.g. [58]. The following inequalities are sufficient for the validity of the Clausius-Duhem inequality (2.34.3)

$$1.\ \mathcal{D}^i = \overline{\mathbf{M}} : \bar{\mathbf{L}}_i - \underline{Q}\ \underline{\dot{q}} \geq 0, \quad 2.\ \mathcal{D}^z = -\underline{Z}\ \underline{\dot{z}} \geq 0, \quad 3.\ \mathcal{D}^\theta = -\frac{1}{\theta}\mathbf{q}_0 \cdot \nabla\theta \geq 0. \quad (3.5)$$

A common approach for the heat flux vector $\mathbf{q}_0$ in Eq.(3.5.2) is the Fourier-law with respect to the reference configuration (see Remark 3.2.1). In a general setting it is necessary to formulate evolution equations

$$1.\ \bar{\mathbf{L}}_i = \bar{\mathbf{L}}_i\ [\overline{\mathbf{M}}, \underline{Q}, \underline{Z}, \underline{q}, \underline{z}, \theta], \quad 2.\ \underline{\dot{q}} = \underline{\dot{q}}\ [\overline{\mathbf{M}}, \underline{Q}, \underline{Z}, \underline{q}, \underline{z}, \theta], \quad 3.\ \underline{\dot{z}} = \underline{\dot{z}}\ [\overline{\mathbf{M}}, \underline{Q}, \underline{Z}, \underline{q}, \underline{z}, \theta], (3.6)$$

which are in accordance with the Clausius-Planck inequality (3.5.1), such that the model under consideration becomes thermodynamically consistent. In the framework above the evolution equations are formulated in terms of the Mandel stress tensor $\overline{\mathbf{M}}$, the hardening stresses $\underline{Q}$ and the chemical forces $\underline{Z}$, which appear as conjugate (dual) variables to $\bar{\mathbf{L}}_i$, $\underline{\dot{q}}$ and $\underline{\dot{z}}$ in Eq.(3.5.1).

Following CAILLETAUD and SAÏ, [15, 70] the terminology "multi-mechanism" is used when different behaviors are observed in the material. These behaviors may be linked to different strain ranges, stress ranges and temperatures, etc. Concerning the mathematical structure of a multi-mechanism model in [70], an $nMmC$ model is obtained with n mechanisms (i.e. number of inelastic strain contributions) and m criteria (i.e. number of yield functions): Accordingly, the above velocity gradient is additively decomposed as

$$\bar{\mathbf{L}}_i = \sum_{j=1}^n \bar{\mathbf{L}}_{in,j}. \quad (3.7)$$

We will return to this issue in Subsection 3.3.9.

Remark 3.1

According to the Fourier-law we have a common approach for the heat flux vector with respect to the current configuration

$$\mathbf{q} = -\lambda_\theta \cdot \nabla_{\mathbf{x}}\theta \quad (3.8)$$

with a positive heat conduction coefficient λ_θ. $\nabla_{\mathbf{x}}$ labels $\partial/\partial\mathbf{x}$ with respect to the current configuration. Due to the fact that the heat flux through area element $d\mathbf{A}$ with respect to the reference configuration ($\mathbf{q}_0 \cdot d\mathbf{A}$) equals which ($\mathbf{q} \cdot d\mathbf{a}$) in the current configuration, we have

$$\mathbf{q} \cdot d\mathbf{a} = \mathbf{q}_0 \cdot d\mathbf{A}. \quad (3.9)$$

Using the relations Eq.(3.8), Eq.(3.9) and Eq.(2.2.2) the heat flux vector with respect to the reference configuration is derived as

$$\mathbf{q}_0 = -\lambda_\theta J \mathbf{F}^{-t}(\mathbf{F}^{-1}\nabla\theta) \tag{3.10}$$

Consequently, the inequality (3.5.3) is rewritten as

$$\mathcal{D}^\theta = \frac{1}{\theta}\lambda_\theta J \mathbf{F}^{-t}(\mathbf{F}^{-1}\nabla\theta)\nabla\theta \geq 0, \tag{3.11}$$

where the absolute temperature θ is always non-negative. The Jocobian J introduced in Eq.(2.2.3) is positive. $\mathbf{F}^{-1}$ and $\nabla\theta$ can be expressed as

$$1. \ \mathbf{F}^{-1} = F_{ij}^{-1}\mathbf{e}_i \otimes \mathbf{e}_j, \quad 2. \ \nabla\theta = \frac{\partial\theta}{\partial X_i}\mathbf{e}_i, \tag{3.12}$$

where $\mathbf{e}_i, i = 1, 2, 3$ are orthogonal unit basis vectors. Following Eq.(3.11) and Eq.(3.12) one obtains

$$\mathbf{F}^{-t}(\mathbf{F}^{-1}\nabla\theta)\nabla\theta = \sum_{i=1}^{3}\left(\sum_{j=1}^{3}F_{ij}^{-1}\frac{\partial\theta}{\partial X_j}\right)^2, \tag{3.13}$$

which is non-negative. Therefore, the inequality (3.11) is fulfilled.

3.2.2 Heat-conduction equation

The following heat-conduction equation can be derived in a standard way from the energy equation (2.34.2) (cf. e.g. HAUPT [34]) with $\Psi = \epsilon - \theta\eta$. Taking the equations (2.13), (2.32) and (3.4) into account, one gets from Eq.(2.34.2):

$$\begin{aligned}
\rho_0\, c_d\,\dot{\theta} + \nabla\mathbf{q}_0 &= \overline{\mathbf{M}} : (\bar{\mathbf{L}}_i + \bar{\mathbf{L}}_\theta + \bar{\mathbf{L}}_z) - \underline{Q}\,\dot{\underline{q}} - \underline{Z}\,\dot{\underline{z}} \\
&\quad + \theta\,\frac{\partial\overline{\mathbf{M}}}{\partial\theta} : \bar{\mathbf{L}}_e + \theta\,\frac{\partial Q}{\partial\theta}\,\dot{\underline{q}} + \theta\,\frac{\partial Z}{\partial\theta}\,\dot{\underline{z}} + \rho_0 r_\theta
\end{aligned} \tag{3.14}$$

with the heat capacity

$$c_d := -\theta\,\frac{\partial^2\Psi}{\partial\theta^2}. \tag{3.15}$$

Eq.(3.14) will be further specialized in Subsection 3.3.9.

3.3 A prototype model for cutting processes

The general thermodynamic framework of the previous section is now specialized to the scenario of a cutting process. To this end, we make concrete proposals for the Helmholtz energy in Eq.(3.2) as well as for the evolution of internal variables. Finally, we discuss the thermodynamic consistency of the model developed below.

In the cutting process under consideration, there are mainly two phases, labelled as follows:

$$A \quad \text{for austenite}$$
$$M \quad \text{for martensite.} \tag{3.16}$$

Consequently, the total number of phases introduced in Eq.(2.18) becomes $n_z = 2$.

3.3.1 Helmholtz energy

The Helmholtz energy Ψ introduced in Eq.(3.2) describes the energy storage due to small reversible deformations of the crystal lattice as well as inelastic deformations. More generally, it can also be used to describe different storage mechanisms, e.g. energy changes due to interfacial effects or dislocations. As a specific example of a Helmholtz energy function we consider, see e.g. RANIECKI and BRUHNS [68], FISCHER $et\ al.$ [24]:

$$
\begin{aligned}
1. \quad & \Psi && = \Psi^{iso}[\overline{\mathbf{C}}_e, \theta] + \Psi^{vol}[\overline{\mathbf{C}}_e, \underline{z}, \theta] + \Psi^{\theta}[\theta] + \Psi^{p}[\underline{q}, \underline{z}, \theta] + \Psi^{ch}[\underline{z}, \theta], \quad \text{where} \\[2mm]
2. \quad & \Psi^{iso} && = \frac{G[\theta]}{4\rho_0} \left(\mathrm{tr}\left[\ln \hat{\mathbf{C}}_e\right]^2 \right) \\[2mm]
3. \quad & \Psi^{vol} && = \frac{1}{2\rho_0} K[\theta] \left(\ln J_e\right)^2 \\[2mm]
4. \quad & \Psi^{\theta} && = \int_{\theta_0}^{\theta} c_d[\bar{\theta}] d\bar{\theta} - \theta \int_{\theta_0}^{\theta} \frac{c_d[\bar{\theta}]}{\bar{\theta}} d\bar{\theta} \\[2mm]
5. \quad & \Psi^{p} && = \Psi^{p1} + \Psi^{p2} = \frac{1}{2\rho_0} H_1 q_1^2 + \frac{1}{2\rho_0} H_2 q_2^2. \\[2mm]
6. \quad & \Psi^{ch} && = \sum_{i=1}^{2} \left(z_i - z_{0i}\right) \phi_{ch,i}[\theta].
\end{aligned}
\tag{3.17}
$$

Remarks 3.2

1. The elastic part $\Psi^{el} = \Psi^{iso} + \Psi^{vol}$ takes storage quantities related to the elastic strains into account. The part Ψ^{iso} in Eq.(3.17.2) considers isochoric deformations due to isochoric elastic strains with $\hat{\mathbf{C}}_e = J_e^{-2/3}\overline{\mathbf{C}}_e$, where $\overline{\mathbf{C}}_e$ is the elastic right Cauchy–Green tensor given in Eq.(A.3). The part Ψ^{vol} in Eq.(3.17.3) considers volumetric strains represented by J_e defined in Eq.(2.4.2). Furthermore, $G[\theta]$ and $K[\theta] = \kappa[\theta]^{-1}$ are the shear modulus and the compression (or bulk) modulus, respectively, both dependent on the temperature θ. These are related to Young's modulus E, Poisson's ratio ν and the compressibility κ as

$$
1. \ \ G[\theta] = \frac{2E[\theta]}{1+\nu}, \qquad 2. \ \ K[\theta] = \frac{E[\theta]}{3(1-2\nu)} = \kappa[\theta]^{-1}. \tag{3.18}
$$

We employ a linear dependence of Young's modulus as

$$
E = E_0 + c_E\left(\theta - \theta_0\right), \tag{3.19}
$$

where θ_0 is the reference temperature and c_E is a constant. We remark, that the above ad hoc extension for the bulk modulus (3.18.2) could also be included in the definition (2.25).

2. According to Eq.(2.27) one obtains the volumetric part of the Helmholz energy

$$
\begin{aligned}
\Psi^{vol} &= \frac{1}{2\rho_0} K[\theta] \left(\ln J_e \right)^2 = \frac{1}{2\rho_0} K[\theta] \left(\ln J - \ln[J_\theta J_z] \right)^2 \\
&\approx \frac{1}{2\rho_0} K[\theta] \left(\ln J - 3 \left(\alpha[\underline{s}_0](\theta - \theta_0) + \underline{\beta}^T[p_0, \theta_0]\underline{z} \right) \right)^2 .
\end{aligned}
\tag{3.20}
$$

$\underline{z}$ is the mass phase fraction defined in Eq.(2.17).

3. We assume the same elastic isotropic behavior for all phases in Eq.(3.17.2) (similarly as in HALLBERG *et al.* [32]). Consequently, it suffices to take into account the temperature dependence as introduced in Eq.(3.19). A dependence of G and K on the phase-fraction vector $\underline{z}$ in Eq.(3.2) is not used.

4. The term Ψ^θ in Eq.(3.17.4) represents the thermally stored energy. Here, we neglect the phase dependence of the specific heat capacity c_d. To be consistent with the approach in (3.17.6), the term Ψ^θ refers to the initial state, e.g. to martensite (cf. point 6 of these remarks).

5. The inelastic part Ψ^p of the Helmholtz free energy is defined in Eq.(3.17.5). It accounts for energy storage due to inelastic deformations, more concretely to combined linear and nonlinear isotropic hardening. q_1 and q_2 are (scalar) internal variables of strain type, such that its number is $n_q = 2$. The evolution will be described below. Note, that there is a technical difference to the presentation in MAHNKEN *et al.* [56], but the sum of the thermodynamical forces Q_1 and Q_2 (cf. Eq.(3.4.1)) finally equals to the single force Q in [56]. Q_0, b and H are positive constants.

6. The term Ψ^{ch} in Eq.(3.17.6) represents the chemically stored energy with respect to phase transformations, which is introduced in MAHNKEN *et al.* [58]. In case of no phase transformations, i.e. for $\underline{z} = \underline{z}_0$, this term does not appear.

3.3.2 Thermodynamic forces

As discussed previously in Section 3.2 the thermodynamic forces are obtained from the relations (3.4). Consequently, from Eq.(3.4.1) and Eq.(3.20) the Mandel stress tensor is

$$
\begin{aligned}
\overline{\mathbf{M}} &= \rho_0 2\overline{\mathbf{C}}_e \cdot \frac{\partial \Psi}{\partial \overline{\mathbf{C}}_e} \\
&= K[\theta] \ln J \mathbf{1} + G[\theta] \text{dev} \ln \left[\overline{\mathbf{C}}_e \right] - 3K[\theta] \left(\alpha[\underline{s}_0](\theta - \theta_0) + \underline{\beta}^T[p_0, \theta_0]\underline{z} \right) \mathbf{1}.
\end{aligned}
\tag{3.21}
$$

The first two terms in Eq.(3.21) represent the spherical and deviatoric stress tensors due to deformations. The third term accounts for thermo-mechanical and chemo-mechanical coupling, respectively.

From the equations (3.4.3-4), (3.20), and (3.17.5-6) we identify the hardening stresses and the chemical forces as

$$
\begin{aligned}
&1.\ Q_1 = \rho_0 \frac{\partial \Psi^p}{\partial q_1} = H_1 q_1, \quad 2.\ Q_2 = \rho_0 \frac{\partial \Psi^p}{\partial q_2} = H_2 q_2, \\
&2.\ Z_i = \rho_0 \frac{\partial \Psi}{\partial z_i} = -K[\theta] \left(\frac{\rho_0}{\rho_i[\theta_0]} - 1 \right) \ln J_e + \rho_0\, \phi_{ch,i}[\theta], \quad i = M, A.
\end{aligned}
\tag{3.22}
$$

Remarks 3.3

1. Applying the "trace-"operator $\mathrm{tr}[\bullet] = \mathbf{1} : [\bullet]$ to Eq.(3.21), renders the pressure as

$$
-3p = \mathrm{tr}\overline{\mathbf{M}} \;=\; 3K[\theta]\left(\ln J - 3\left(\alpha[\underline{s}_0](\theta - \theta_0) + \underline{\beta}^T[p_0, \theta_0]\underline{z} \right) \right)
\tag{3.23}
$$

   which for $p_0 = 0$, $\theta = \theta_0$ is in accordance with Eq.(2.27).

2. As we will see later, the two terms on the right-hand side of Eq.(3.22.1) represent nonlinear and linear isotropic hardening, respectively.

3. For steel (see [58, 59]) and small elastic strains we have

$$
\left(\frac{\rho_0}{\rho_i[\theta_0]} - 1 \right) \approx 0,\ J_e \approx 1\ \Rightarrow K[\theta]\left(\frac{\rho_0}{\rho_i[\theta_0]} - 1 \right) \ln J_e \approx 0\ \Rightarrow Z_i \approx \rho_0\, \phi_{ch,i}[\theta].
\tag{3.24}
$$

4. The chemical force $Z_i \approx \rho_0 \phi_{ch,i}$ can be regarded as (the volume density of) the free enthalpy of the phase z_i. (This fact relies on the Gibbs-Duhem relation, we refer to [66], [29], [68], amongst others).

In the process under consideration with two phases the balance relation (2.18.1) relates the rate of austenite to the rate of martensite as

$$
\dot{z}_A = -\dot{z}_M.
\tag{3.25}
$$

This allows writing

$$
-\sum_{i=1}^{2} Z_i \dot{z}_i = -Z_M \dot{z}_M - Z_A \dot{z}_A = -\left(Z_M - Z_A \right) \dot{z}_M.
\tag{3.26}
$$

Thus, employing the approximation (3.24) for the chemical forces Z_i, the dissipation term related to phase transformations in Eq.(3.5) can be re-written as

$$
-\sum_{i=1}^{2} Z_i \dot{z}_i = -\left(Z_M - Z_A \right) \dot{z}_M \approx -\rho_0 \left(\phi_{ch,M} - \phi_{ch,A} \right) \dot{z}_M.
\tag{3.27}
$$

Analogously to the assumption of MAHNKEN *et al.* [58] a possible relation for the chemical force difference $Z_M - Z_A$ is

$$
Z_M - Z_A = \rho_0(\phi_{ch,M} - \phi_{ch,A}) = \rho_0(\theta - \theta_0^{(M,A)}) \frac{Q_{M,A}^*}{\theta_0^{(M,A)}}.
\tag{3.28}
$$

Here $\theta_0^{(M,A)}$ is defined as the equilibrium temperature, at which the martensitic phase has the same free enthalpy as the austenite. Consequently, the temperature difference $(\theta - \theta_0^{(M,A)})$ is the "undercooling" or the "overheating", respectively. Furthermore, in Eq.(3.28) $Q_{M,A}^*$ is the activation energy for the transformation $M \to A$. It is assumed to be positive, which is a plausible assumption, since a phase transformation only takes place, if the free enthalpy of the parent phase is greater than the free enthalpy of the generated phase. For details we refer to [58]. We will return to this point when discussing thermodynamic consistency of the model in Subsection 3.3.7 as well as when dealing with the special case of the heat-conduction equation in Subsection 3.3.9.

3.3.3 A yield function of Johnson-Cook type

In [44] the following (original) relation is proposed for the von Mises stress σ_v:

$$
\begin{aligned}
1. \quad \sigma_v &= (A + Be_v^n)\left(1 - (\theta^*)^m\right)\left(1 + C \ln\left(\frac{\dot{e}_v}{\dot{\varepsilon}_0}\right)\right), \\
2. \quad \theta^* &= \begin{cases} 0 & \text{for } \theta < \theta^r \\ \dfrac{\theta - \theta^r}{\theta^m - \theta^r} & \text{for } \theta^r \leq \theta \leq \theta^m \\ 1 & \text{for } \theta > \theta^m \end{cases} .
\end{aligned}
\tag{3.29}
$$

Here θ^* is the homologous temperature, θ^r is the room temperature and θ^m is the melt temperature of the material, respectively, and $A, B, n, C, \dot{\varepsilon}_0, m$ are six material parameters. A is the initial yield stress (subsequently denoted as Y_0), and B and n represent the effect of strain hardening. C and ε_0 represent the effect of rate dependency for the yield stress, whereas m represents the effect of adiabatic heating. The above formulation accounts for rate and temperature dependency.

From the original Johnson-Cook function (3.29), we formulate a yield function

$$
\begin{aligned}
1. \quad \phi &= \sigma_v - (Y_0 + Q_1 + Q_2)\mathcal{J} \\
2. \quad \mathcal{J} &= \mathcal{J}^\theta \mathcal{J}^R \\
3. \quad \mathcal{J}^\theta &= (1 - (\theta^*)^m) \\
4. \quad \mathcal{J}^R &= \left(1 + C \ln\left(\left\langle \frac{\dot{e}_v}{\dot{\varepsilon}_0} \right\rangle_1\right)\right),
\end{aligned}
\tag{3.30}
$$

where the von Mises stress is written in terms of the deviatoric part of the Mandel stress tensor as

$$
\sigma_v = \sqrt{\frac{3}{2}}\|\overline{\mathbf{M}}^{dev}\|.
\tag{3.31}
$$

Subsequently, the coefficient $\mathcal{J}$ in Eq. (3.30.2) shall be refered to as the Johnson-Cook coefficient, where $\mathcal{J}^\theta$ and $\mathcal{J}^R$ reflect the dependences of temperature and strain rate, respectively.

Remarks 3.4

1. Comparing Eq.(3.29) and Eq.(3.30) we introduce as a first modification, that the hardening stress Be_v^n in Eq.(3.29) is replaced by the sum of hardening stresses Q_1 and Q_2 introduced in the relations (3.22).

2. Comparing Eq.(3.29) and Eq.(3.30) we introduce as a further (slight) modification the notation $\langle x \rangle_1 = \max\{x, 1\}$. This ensures the relation

$$\mathcal{J} = (1 - (\theta^*)^m)\left(1 + C\ln\left(\left\langle \frac{\dot{e}_v}{\dot{\varepsilon}_0} \right\rangle_1\right)\right) \geq 0 \tag{3.32}$$

for all parameters $C \geq 0$, $\varepsilon_0 > 0$, $m > 0$, and all temperatures $\theta > 0$.

3.3.4 Evolution equations for visco-plasticity

We split the inelastic part $\bar{\mathbf{L}}_i$ of the velocity gradient $\bar{\mathbf{L}}$ in Eq.(2.13) into the sum

$$\bar{\mathbf{L}}_i = \bar{\mathbf{L}}_p + \bar{\mathbf{L}}_t, \tag{3.33}$$

where $\bar{\mathbf{L}}_p$ and $\bar{\mathbf{L}}_t$ represent the visco-plastic and the TRIP part, respectively. In the following we propose evolution equations for both quantities. Within this approach, we extend the well-known Johnson-Cook model in order to take into account asymmetric effects for plasticity, based on the concept of stress-mode related weighting functions introduced in [50].

Stress mode related weighting functions

As introduced in Section 1.1 and 1.2, and following the approach of Mahnken [50] for weighting functions w_i it is stipulated that

$$1.\ \sum_{i=1}^{S} w_i[\overline{\mathbf{M}}] \ = \ 1, \quad 2.\ w_i[\overline{\mathbf{M}}_j] \ = \ \delta_{ij}, \quad 3.\ w_i[\overline{\mathbf{M}}] \ \geq \ 0, \tag{3.34}$$

i.e. the weighting functions w_i are associated to different independent characteristic *stress modes* characterised by stress tensors $\overline{\mathbf{M}}_j$, $j = 1, 2, .., S$. We also remark, that Eq.(3.34.1) can be regarded as a *completeness condition*, whereas Eq.(3.34.2) constitutes a *normalisation condition* for the weighting functions. The specific mathematical structures for weighting functions have been introduced in [50] on the basis of the following quantities:

$$1. \qquad \xi \ = \ \frac{\sqrt{27}}{2}\frac{\overline{M}_{dev}I_3}{(\overline{M}_{dev}I_2)^{3/2}},$$

$$2. \quad \overline{M}_{dev}I_i \ = \ \frac{1}{i}\mathbf{1} : (\overline{\mathbf{M}}^{dev})^i, \qquad i = 2, 3. \tag{3.35}$$

The quantity ξ is refered to as the *stress mode factor* and has the property $-1 \leq \xi \leq 1$. Related graphical interpretations are given in [50].

For the stress modes related to the loading scenarios of tension, compression and shear we set $S = 3$. Then the requirements (3.34) are satisfied by the following weighting functions in terms of the stress mode factor ξ:

$$
\begin{array}{llll}
\text{1.} & \text{tension:} & w_1[\xi] & = \begin{cases} \xi^2, & \text{if} \quad \xi \geq 0 \\ 0, & \text{else} \end{cases} \\[3mm]
\text{2.} & \text{compression:} & w_2[\xi] & = \begin{cases} \xi^2, & \text{if} \quad \xi \leq 0 \\ 0, & \text{else} \end{cases} \\[3mm]
\text{3.} & \text{shear:} & w_3[\xi] & = 1 - \xi^2
\end{array}
\tag{3.36}
$$

For the case, that experimental data are available only for the loadings in tension and compression, with $S = 2$ the following functions are used

$$
\begin{array}{llll}
\text{1.} & \text{tension:} & w_1[\xi] & = \dfrac{1}{2}(1 + \xi) \\[3mm]
\text{2.} & \text{compression:} & w_2[\xi] & = \dfrac{1}{2}(1 - \xi).
\end{array}
\tag{3.37}
$$

Evolution of internal variables

We assume the following evolution equations for the visco-plastic part $\bar{\mathbf{L}}_p$ of the velocity gradient in Eq.(3.33) and the internal variables q_1 and q_2 in the relation (3.17.4)

$$
\begin{array}{llll}
\text{1.} & \bar{\mathbf{L}}_p & = & \dot{\lambda}\sqrt{\dfrac{3}{2}}\mathbf{N}, \quad \text{where} \quad \mathbf{N} = \dfrac{\overline{\mathbf{M}}^{dev}}{||\overline{\mathbf{M}}^{dev}||}, \\[3mm]
\text{2.} & \dot{q}_1 & = & \dot{\lambda}\mathcal{J}\left(1 - c\dfrac{Q_1}{H_1}\right), \\[3mm]
\text{3.} & \dot{q}_2 & = & \dot{\lambda}\mathcal{J},
\end{array}
\tag{3.38}
$$

where $\mathcal{J}$ is the Johnson-Cook coefficient in Eq. (3.32.2). Furthermore, the plastic multiplier $\dot{\lambda}$ is obtained from the loading/unloading conditions, see e.g. [74],

$$
\text{1.} \ \dot{\lambda} \geq 0, \quad \text{2.} \ \phi \leq 0, \quad \text{3.} \ \dot{\lambda}\phi = 0.
\tag{3.39}
$$

Here, we have also introduced the rate of equivalent plastic strain $\dot{e}_v$, defined as $\dot{e}_v^2 = 2/3\ \bar{\mathbf{L}}_p : \bar{\mathbf{L}}_p$, such that by use of Eq.(3.38.1) one obtains the relation

$$
\dot{e}_v = \sqrt{\dfrac{2}{3}\bar{\mathbf{L}}_p : \bar{\mathbf{L}}_p} = \dot{\lambda}\sqrt{\dfrac{2}{3}\dfrac{3}{2}\mathbf{N} : \mathbf{N}} = \dot{\lambda}.
\tag{3.40}
$$

Remarks 3.5

1. The coefficient $c \geq 0$ in Eq. (3.38.2) may depend on the temperature and different quantities, e.g. invariants of the stress tensor.

2. Here, we consider positive constant parameters H_1 and H_2. A dependence on temperature is possible, while a dependence on further quantities would result in more terms in the Clausius-Planck inequality (3.5.1).

3. As explained in [51] an alternative mixed-variant representation of the above flow rule (3.38.1) relative to the reference configuration $\mathcal{B}_0$ is as follows:

$$
\begin{aligned}
1. \quad \mathbf{L}_i &= \mathbf{F}_i^{-1} \cdot \bar{\mathbf{L}}_i \cdot \mathbf{F}_i = -\frac{1}{2}\dot{\mathbf{C}}_i^{-1} \cdot \mathbf{C}_i = \dot{\lambda}\mathbf{N}, \quad \text{where} \\
2. \quad \mathbf{N} &= \frac{\overline{\mathbf{M}}^{dev}}{||\overline{\mathbf{M}}^{dev}||} \\
3. \quad \mathbf{C}_i &= \mathbf{F}_i^t \cdot \mathbf{F}_i,
\end{aligned}
\tag{3.41}
$$

This representation is more convenient with respect to numerical implementation in order to get an objective time-integration scheme [74].

According to the relations (3.22.1),(3.22.2), (3.38.2) and (3.38.3) one obtains

$$
\begin{aligned}
1. \quad &\dot{Q}_1 = H_1\dot{q}_1 = \dot{\lambda}\mathcal{J}\left(H_1 - cQ_1\right) \\
2. \quad &\dot{Q}_2 = H_2\dot{q}_2 = \dot{\lambda}H_2\mathcal{J}.
\end{aligned}
\tag{3.42}
$$

For the special case $\mathcal{J} = 1$, H_1, H_2 and $c > 0$ being constant, and the initial conditions $Q_1(0) = 0$, $Q_2(0) = 0$ one obtains the solutions

$$
\begin{aligned}
1. \quad Q_1(e_v) &= \frac{H_1}{c}(1 - \exp(-ce_v)) \\
2. \quad Q_2(e_v) &= H_2e_v.
\end{aligned}
\tag{3.43}
$$

With the stress mode related weighting functions in the equations (3.35) to (3.37) and evolution of the hardening stresses in (3.42) at hand we are in a position to formulate two extended variations of the original Johnson-Cook model based on Eq.(3.29).

Huh-Kang rate form extended to the SD-effect

The rate form $\mathcal{J}^R$ in Eq.(3.30.4) used to consider strain rate dependency is linear in the logarithm of the strain rate. As mentioned in Section 3.1, based on experiments most materials exhibit a bi-linear or quadratic dependence of strength on the logarithm of the strain rate. As a consequence the Huh-Kang form [37] provides a significant improvement over the standard Johnson-Cook rate form and other forms. It is quadratic in the logarithm of the effective plastic strain rate

$$
\mathcal{J}_{HK}^R = 1 + C_1 \ln\left(\left\langle \frac{\dot{e}_v}{\dot{\varepsilon}_0} \right\rangle_1\right) + C_2 \left(\ln\left(\left\langle \frac{\dot{e}_v}{\dot{\varepsilon}_0} \right\rangle_1\right)\right)^2
\tag{3.44}
$$

with two parameters C_1 and C_2. In order to obtain a better agreement with available experimental results, we replace the term $\mathcal{J}^R$ with $\mathcal{J}^R_{HK}$ within the yield function Eq.(3.30.4).

Concerning the SD-effect, we weight the parameters of the Huh-Kang rate form as

$$1. \;\; C_1 = \sum_{i=1}^{S} w_i C_{1i}, \quad 2. \;\; C_2 = \sum_{i=1}^{S} w_i C_{2i}, \quad 3. \;\; \dot{\varepsilon}_0 = \sum_{i=1}^{S} w_i \dot{\varepsilon}_{0i}, \tag{3.45}$$

where w_i are weighting functions given in Eq.(3.34). C_{1i}, C_{2i} and $\dot{\varepsilon}_{0i}$ are stress mode related parameters with $i = 1 \ldots S$ for S different stress modes.

Summary of the asymmetric visco-plasticity

Table 3.1 summarizes all equations for the first proposel for simulation of asymmetric visco-plasticity: It consists of a flow rule in Eq.I, with flow direction in Eq.II and flow factor in Eq.III. The yield function in Eq IV constitutes a barrier term for the von Mises stress σ_v in Eq.V, written in terms of the Mandel stress tensor $\overline{\mathbf{M}}$. The scalar Y_0 in Eq.IV represents an initial barrier for inelastic behavior, which is increased by the hardening stresses Q_1 and Q_2 in Eq.VI. The total barrier $Y_0 + Q_1 + Q_2$ may be decreased or increased by the Johnson-Cook coefficient $\mathcal{J}$ in Eq.VII. Rate dependence is achieved by the factor $\mathcal{J}^R_{HK}$. The asymmetric effect is obtained by the weighted constants in the equations VIII. All related material parameters are summarized in Eq.IX.

3.3.5 A flow rule for transformation plasticity

A general flow rule for the transformation part $\bar{\mathbf{L}}_t$ occurring in Eq.(3.33) can be written as

$$\bar{\mathbf{L}}_t = \sum_{i=1}^{n_z} \bar{\mathbf{L}}_{t,i}, \tag{3.46}$$

where $\bar{\mathbf{L}}_{t,i}$ represent TRIP-strain velocities due to transformation of the i-th phase, see e.g. [58] for multiple transformations strains. Regarding that TRIP is caused by austenitic transformation as well as by martensitic transformation, we suppose

$$\bar{\mathbf{L}}_t = \begin{cases} \dot{z}_A \dfrac{3}{2} f'_A K_{tpA} \, (\overline{\mathbf{M}}^{dev})^t & \text{for} \;\; \dot{z}_A \geq 0 \\[4mm] \dot{z}_M \dfrac{3}{2} f'_M K_{tpM} \, (\overline{\mathbf{M}}^{dev})^t & \text{for} \;\; \dot{z}_A < 0. \end{cases} \tag{3.47}$$

In this way, the term $\bar{\mathbf{L}}_t$ in Eq.(3.47) generalizes the TRIP approach due to LEBLOND [47] among others within a small strain theory. The scalars K_{tpA} and K_{tpM} in Eq.(3.47) are the Greenwood-Johnson parameters. The saturation function $f_1[z_M]$ in Eq.(3.47) is a heuristic function satisfying

$$1. \; f_1[0] = 0, \qquad 2. \; f_1[1] = 1, \qquad 3. \; f'_1[z] = \frac{df_1}{dz} \geq 0. \tag{3.48}$$

I.	Flow rule	$\bar{\mathbf{L}}_p = \dot{\lambda}\sqrt{\dfrac{3}{2}}\mathbf{N}$
II.	Flow direction	$\mathbf{N} = \dfrac{\overline{\mathbf{M}}^{dev}}{\|\overline{\mathbf{M}}^{dev}\|}$
III.	Flow factor	$\dot{\lambda} = \dot{e}_v = \sqrt{\dfrac{2}{3}\bar{\mathbf{L}}_p : \bar{\mathbf{L}}_p}$
IV.	Yield function	$\Phi = \sigma_v - (Y_0 + Q_1 + Q_2)\,\mathcal{J}$
V.	von Mises stress	$\sigma_v = \sqrt{\dfrac{3}{2}}\|\overline{\mathbf{M}}^{dev}\|$
VI.	Hardening stresses	$\dot{Q}_1 = \dot{\lambda}\mathcal{J}\left(H_1 - cQ_1\right), \quad \dot{Q}_2 = \dot{\lambda}H_2\mathcal{J}$
VII.	JC coefficient	$\mathcal{J} = \mathcal{J}^\theta \mathcal{J}^R_{HK} \geq 0, \quad \mathcal{J}^\theta = (1 - (\theta^*)^m)$
VIII	HK coefficient	$\mathcal{J}^R_{HK} = 1 + C_1 \ln\left(\left\langle\dfrac{\dot{e}_v}{\dot{\varepsilon}_0}\right\rangle_1\right) + C_2\left(\ln\left(\left\langle\dfrac{\dot{e}_v}{\dot{\varepsilon}_0}\right\rangle_1\right)\right)^2$
IX.	Weighted constants	$Y_0 = \sum\limits_{i=1}^{S} w_i Y_{0i}, \quad c = \sum\limits_{i=1}^{S} w_i c_i, \quad C_1 = \sum\limits_{i=1}^{S} w_i C_{1i},$ $C_2 = \sum\limits_{i=1}^{S} w_i C_{2i}, \quad \dot{\varepsilon}_0 = \sum\limits_{i=1}^{S} w_i \dot{\varepsilon}_{0i}, \quad m = \sum\limits_{i=1}^{S} w_i m_i$
X.	Material parameters	$\boldsymbol{\kappa}_{pi} = [Y_{0i}, H_{1i}, H_{2i}, c_i, C_{1i}, C_{2i}, \dot{\varepsilon}_{0i}, m_i]^T, \; i = 1, ..., S$

Table 3.1: Constitutive equations for visco-plasticity combining Huh-Kang rate form to the SD-effect

A possible formulation is given by DENIS [19] as

$$1.\ f[z_A] = (2 - z_A)\,z_A \quad \Rightarrow \quad 2.\ f'[z_A] = 2\left(1 - z_A\right), \quad 3.\ f''[z_A] = -2. \quad (3.49)$$

for austenitic transformation, and

$$1.\ f[z_M] = (2 - z_M)\,z_M \quad \Rightarrow \quad 2.\ f'[z_M] = 2\left(1 - z_M\right), \quad 3.\ f''[z_M] = -2. \quad (3.50)$$

for martensitic transformation. For further discussions and references concerning TRIP we refer to WOLFF *et al.* [90].

3.3.6 Evolution of phase fractions

The cutting forming process under consideration is characterized by two phase transformations generally being dependent of each other: Transformatiom of the martensitic initial state into austenite and retransformation to martensite. There are a lot of different

phenomenological (macroscopic) approaches for phase transformations in steel. For discussion and references we refer Wolff *et al.* [88]. In the following we give some specific formulations for both phases according to the numbering (3.16).

In our setting, austenite can only be formed from the martensitic initial state due to conversion of mechanical dissipation into heat during the cutting process. Thus, we set the initial conditions

$$\underline{z}_0 = [z_{M0}, z_{A0}] = [1, 0]^T. \tag{3.51}$$

As a consequence of Eq.(3.51), the initial density ρ_0 equals to $\rho_M[\theta_0]$. Moreover, in the elastic part $\Psi^{el} = \Psi^{iso} + \Psi^{vol}$ of the free energy (see (Eq.3.17.3)) as well as in Eq.(3.21) and Eq.(3.22) some specifications occur. For instance, Ψ^{el} now reads as

$$\Psi^{el} = \frac{G[\theta]}{4\rho_M[\theta_0]} \left(\text{tr} \left[\ln \hat{\mathbf{C}}_e \right]^2 \right) + \frac{K[\theta]}{2\rho_M[\theta_0]} \left(\ln J - (3\alpha_M[\theta](\theta - \theta_0) + K_{tv} z_A) \right)^2. \tag{3.52}$$

Here the constant

$$K_{tv} = \left(\frac{\rho_M[\theta_0]}{\rho_A[\theta_0]} - 1 \right) \tag{3.53}$$

represents the volume change ratio $\Delta V / V$ after complete transformation for a two phase system, see e.g. [55].

1. Formation of austenite: The heating is very fast and leads to high temperatures. Therefore, for the evolution of the austenite phase fraction z_A we suppose a simple approach due to Leblond and Devaux [46]

$$\dot{z}_A = \mu_{MA} (1 - z_A) H(\theta - A_{c1}), \tag{3.54}$$

where $\mu_{MA} > 0$ is a constant, A_{c1} is the austenite start temperature. The Heaviside function H with $H(s) = 1$ for $s > 0$ and $H(s) = 0$, otherwise, plays the role of a switcher.

2. Formation of martensite: Martensite can only be formed from austenite during rapid cooling due to the contact between work-piece and tool, namely near the surface. We use a rate form of the Koistinen-Marburger approach

$$\dot{z}_M = \left\langle \frac{-\dot{\theta}}{k_\theta} \right\rangle (1 - z_M) H(\theta_{MS} - \theta). \tag{3.55}$$

Here, $k_\theta > 0$ is the Koistinen-Marburger parameter, and θ_{MS} is the martensite start temperature. In Eq.(3.55) we assume, that the total amount of martensite transforms into austenite and thus is available for retransformation into martensite. Otherwise, the term $(1 - z_M)$ could be replaced by $(z_A - z_M)$.

3.3.7 Thermodynamic consistency

For thermodynamic consistency of material behavior under consideration it is sufficient, that the Clausius-Plank inequality (3.5.1) is fulfilled. In the sequel, we basically follow

the approach in [58]. Using the split (3.33), the evolution equations (3.47) for TRIP, (3.38.2), (3.38.3) for the internal variables q_1 and q_2, the Clausius-Planck inequality (3.5.1) re-writes as

$$
\begin{aligned}
\mathcal{D}^i \quad &= \overline{\mathbf{M}} : \bar{\mathbf{L}}_i - Q_1 \dot{q}_1 - Q_2 \dot{q}_2 - \sum_{i=1}^{2} Z_i \dot{z}_i \\
&= \dot{\lambda} \underbrace{\left(\sigma_v - (Q_1 + Q_2)\, \mathcal{J} \right)}_{\geq Y_0 \mathcal{J}} + \dot{\lambda} c \frac{Q_1^2}{H_1} \mathcal{J} \\
&\quad + \begin{cases} \dot{z}_A \dfrac{3}{2} f'_A K_{tpA}\ (\overline{\mathbf{M}}^{dev})^t \quad \text{for}\ \ \dot{z}_A \geq 0 \\[2mm] \dot{z}_M \dfrac{3}{2} f'_M K_{tpM}\ (\overline{\mathbf{M}}^{dev})^t \quad \text{for}\ \ \dot{z}_A < 0 \end{cases} - \sum_{i=1}^{2} Z_i \dot{z}_i \geq 0.
\end{aligned}
\tag{3.56}
$$

Due to $K_{tpA} > 0$ and $K_{tpM} > 0$ the first three terms in (3.56) are non-negative. Therefore, it remains to investigate the last term. Using the approximation (3.24), the assumption (3.28) and re-writing this term in accordance with (3.27), it remains to proof that

$$
- \sum_{i=1}^{2} Z_i \dot{z}_i = -\rho_0 \sum_{i=1}^{2} (\theta - \theta_0^{(i,2)}) \frac{Q_{i,2}^*}{\theta_0^{(i,2)}} \dot{z}_i \geq 0.
\tag{3.57}
$$

Since the activation energies $Q_{i,2}^*$ are assumed to be positive, each summand in (3.57) is non-negative (taking the minus sign in front of the sum into account). Indeed, for the transformation $M \to A$ (initial state to austenite), the temperature θ is higher than the equilibrium temperature $\theta_0^{(i,2)}$ and z_M decreases, i.e. $\dot{z}_M \leq 0$. Contrary, during the transformations $A \to M$ (austenite to martensite), ones has $\theta_0^{(M,A)} > \theta$ and $\dot{z}_M \geq 0$. It is well-known that the formation of martensite is not an equilibrium reaction, and there must be a considerable undercooling. Thus, the martensite-start temperature θ_{MS} is much less than $\theta_0^{(M,A)}$. However, this does not contradict our reasoning at the macroscopic level. Note, the proof can also be found in [88].

Thus, the multi-mechanism model under consideration is thermodynamically consistent. Moreover, this result does not depend on special approaches for the evolution equations for the phase fractions like Leblond-Devaux (3.54) or Koistinen-Marburger (3.55).

3.3.8 Interpretation as a multi-mechanism model

As mentioned in Section 3.2.1 the terminology "multi-mechanism" is used when different behaviors are observed in the material, linked to different strain ranges, different stress ranges, different temperatures, etc. Accordingly, this list of macroscopic effects can extended to compression, tension and torsion modes and moreover to phase transformation, as proposed in our prototype model. Thus, we have $n = S + n_z$ mechanisms corresponding to S stress modes and n_z phase-transformations. According to the overview in Table 3.1, the number of yield criteria is $S = 1$.

To the authors knowledge, up to now the theory of multi-mechanism models has been developed only in the framework of small deformations (see Saï [70]). In this setting, the possible coupling of the mechanisms via the coupling of individual back stresses

is characteristic and allows to describe observable interactions. For an application to steel behaviour we refer to WOLFF *et al.* [91]. A corresponding application to finite deformations with coupled kinematic hardening remains to future work.

3.3.9 Special form of the heat-conduction equation

In our case of two phases involved in the process, we can re-write the heat-conduction equation (3.14), expressing again the austenite rate. This gives

$$
\begin{aligned}
\rho_0\, c_d\, \dot{\theta} + \nabla \mathbf{q}_0 \;=\;\; & \overline{\mathbf{M}} : (\bar{\mathbf{L}}_i + \bar{\mathbf{L}}_\theta + \bar{\mathbf{L}}_z) - \underline{Q}\, \dot{\underline{q}} \\
& + \theta\, \frac{\partial \overline{\mathbf{M}}}{\partial \theta} : \bar{\mathbf{L}}_e + \theta\, \frac{\partial \underline{Q}}{\partial \overline{\theta}}\, \dot{\underline{q}} + \textstyle\sum_{i=1}^{2} L_{i2}\dot{z}_i + \rho_0 r_\theta,
\end{aligned}
\tag{3.58}
$$

where the *latent heat* L_{i2} of the transformation $A \to M$ is introduced as

$$
L_{MA} := \left(-Z_M + Z_A + \theta\, \frac{\partial Z_M}{\partial \theta} - \theta\, \frac{\partial Z_A}{\partial \theta} \right).
\tag{3.59}
$$

Note, as introduced in Eq.(3.16) $i = 1$ and $i = 2$ represent A and M, respectively. Clearly, the relation $L_{AA} = 0$ holds. Using the approximation (3.24) and the assumption (3.28) one gets (in case of constant $Q^*_{i,2}$) from (3.59):

$$
L_{MA} = \rho_0\, Q^*_{M,A}.
\tag{3.60}
$$

Thus, (the volume density of) the activation energy $\rho_0 Q^*_{M,A}$ of the transformation $A \to M$ is the latent heat of the corresponding transformation. This assertion corresponds to the observation, that the formation of martensite is exotherm. Contrary, the formation of austenite is endotherm.

In our case, the isotropic hardening stresses do not depend on temperature. Thus, we can finally write the heat-conduction equation in the following form.

$$
\begin{aligned}
\rho_0\, c_d\, \dot{\theta} + \nabla \mathbf{q}_0 \;=\;\; & \overline{\mathbf{M}} : (\bar{\mathbf{L}}_i + \bar{\mathbf{L}}_\theta + \bar{\mathbf{L}}_z) - \underline{Q}\, \dot{\underline{q}} \\
& + \theta\, \frac{\partial \overline{\mathbf{M}}}{\partial \theta} : \bar{\mathbf{L}}_e + \textstyle\sum_{i=1}^{2} L_{i2}\dot{z}_i + \rho_0 r_\theta,
\end{aligned}
\tag{3.61}
$$

3.3.10 Summary of constitutive equations

The constitutive relations of our multimechanism model are formulated relative to the intermediate configuration $\bar{\mathcal{B}}$ and summarized in Eq. (I) to Eq. (IV) of Table 3.2.

In Table 3.2 also the material parameters are summarized. Note, according to Eq.(3.52), the Eq.(3.21) is updated as Eq.(I.1) with new parameters α_M and K_{tv}. Using the elastic push-forward relations $\mathbf{b}_e = {}_*\Phi_e^\sharp[\overline{\mathbf{G}}^\sharp]$ in Eq.(A.2.2) and rewriting Eq.(A.4.2) as $\mathbf{g}^\flat = {}_*\Phi_e^\flat[\overline{\mathbf{C}}_e]$ renders an elastic push-forward of the mixed variant Mandel stress and the inelastic mixed variant velocity gradient relative to the intermediate configuration

$$
1.\; \mathbf{m} = {}_*\Phi_e'[\overline{\mathbf{M}}], \qquad 2.\; \mathbf{l}_i = {}_*\Phi_e^\backslash[\bar{\mathbf{L}}_i].
\tag{3.62}
$$

I. Mandel stress tensor

1. $$\overline{\mathbf{M}} = K[\theta]\ln J_e \bar{\mathbf{1}}' + G[\theta]\text{dev}\ln\left(\overline{\mathbf{C}}_e\right)$$
$$- K[\theta]\left(3\Delta\theta\,\alpha_M[\theta] + K_{tv}z_A\right)\mathbf{1}$$

2. $$G(\theta) = \frac{2E(\theta)}{1+\nu}, \quad K(\theta) = \frac{E(\theta)}{3(1-2\nu)}, \quad E = E_0 + c_E\left(\theta - \theta_{E_0}\right)$$

II. Inelastic flow

- Additive decomposition

1. $$\bar{\mathbf{L}}_i = \bar{\mathbf{L}}_p + \bar{\mathbf{L}}_t$$

- Visco-plastic flow: see Table 3.1

- TRIP flow

1. $$\bar{\mathbf{L}}_t = \begin{cases} \dot{z}_A\dfrac{3}{2}f_A' K_{tpA}\,(\overline{\mathbf{M}}^{dev})^t & \text{for}\ \ \dot{z}_A \geq 0 \\[2mm] \dot{z}_M\dfrac{3}{2}f_M' K_{tpM}\,(\overline{\mathbf{M}}^{dev})^t & \text{for}\ \ \dot{z}_A < 0 \end{cases}$$

2. $$f[z_A] = (2 - z_A)\,z_A$$

3. $$f[z_M] = (2 - z_M)\,z_M$$

III. Phase transformation (PT) kinetics

- Martensite $\rightarrow$ Austenite $(M \rightarrow A)$:

1. $$\dot{z}_A = \mu_{MA}\left(1 - z_A\right)H(\theta - A_{c1})$$

- Austenite $\rightarrow$ Martensite $(A \rightarrow M)$:

2. $$\dot{z}_M = \left\langle\frac{-\dot{\theta}}{k_\theta}\right\rangle(1 - z_M)H(\theta_{MS} - \theta)$$

IV. Material parameters

1. $$\boldsymbol{\kappa}_{el} = [E_0, c_E, \theta_{E_0}, \nu]^T$$
2. $$\boldsymbol{\kappa}_\theta = [\alpha_M]^T$$
3. $$\boldsymbol{\kappa}_{tp} = [K_{tpA}, K_{tpM}, \mu_{MA}, k_\theta]^T$$
4. $$\boldsymbol{\kappa}_{co} = [\theta^m, \theta^r, \rho_M, \rho_A, A_{c1}, \theta_{MS}]^T$$

Table 3.2: Multimechanism model for visco-plasticity and transformation-induced plasticity at large strains.

Consequently for the quantities in Eq.I and Eq.III in Table 3.2 one obtains the mixed variant Kirchhoff stress tensor and the mixed variant velocity gradient relative to the current configuration

1. $\mathbf{m}$ $=$ $\rho_0 2\mathbf{g}^\flat \cdot \dfrac{\partial \Psi}{\partial \mathbf{g}^\flat}$

   $= K[\theta] \ln J_e \mathbf{1}' + G[\theta] \mathrm{dev} \ln \left[\mathbf{g}^\flat \cdot \mathbf{b}_e \right] - K[\theta] \left(3\Delta\theta\, \alpha_M[\theta] + K_{tv} z_A \right) \mathbf{1}'$

$$(3.63)$$

2. $\mathbf{l}_i$ $=$ $\dot{\lambda} \sqrt{\dfrac{3}{2}} \mathbf{n}^t + \begin{cases} \dot{z}_A \dfrac{3}{2} f'_A K_{tpA} \, (\mathbf{m}^{dev})^t & \text{for } \dot{z}_A > 0 \\[2mm] \dot{z}_M \dfrac{3}{2} f'_M K_{tpM} \, (\mathbf{m}^{dev})^t & \text{for } \dot{z}_A < 0 \end{cases}$, $\qquad \mathbf{n} = \dfrac{\mathbf{m}^{dev}}{||\mathbf{m}^{dev}||}.$

It should also be noted that there are some limitations on the applicability of the equations in Table 3.2 for general loading paths, especially unloading. However, for the sake of simplicity and assuming that for the cutting process more or less proportional loading paths are to be expected, they will serve as a working assumption in this chapter.

3.4 Numerical implementation

The multi-mechanism model developed in Section 3.3 considers thermal problem, mechanical problem and phase transformations, where the heat-conduction equation (3.14) is coupled with the constitutive equations summarized in Table 3.1-3.2. Principally, the coupled problem can be solved in a monolithic way, however, we employ a staggered algorithm, consisting of the solution of the thermal problem, followed by the mechanical and transformational problem at each time step, in contrast to a fully implicit algorithm. The resulting algorithm is very similar to the approaches in [51, 52, 55]. Consequently, in what follows we will concentrate on the numerical integration for the constitutive equations summarized in Table 3.2, where an implicit Euler scheme for time integration is used.

3.4.1 Integration scheme

A *strain-driven* algorithm is considered over a finite time step $\Delta t = {}^{n+1}t - {}^n t$ according to standard integration procedures in finite element techniques. To this end the deformation gradient ${}^{n+1}\mathbf{F}$ and the Jacobian ${}^{n+1}J$ at the actual time step ${}^{n+1}t$ are given. As initial data the internal variables ${}^n q$ and the inverse inelastic right Cauchy Green strain tensor ${}^n \mathbf{C}_i^{-1}$ (defined in Eq.(A.2.1)) at the old time step ${}^n t$ are given too. Additionally we assume, that temperatures ${}^n\theta$, ${}^{n+1}\theta$ are provided as a result of the thermal problem within the staggered algorithm explained above.

The numerical integration is started with the velocity gradient in the reference configuration (see Eq.(2.15.2))

$$\mathcal{B}_0: \quad \mathbf{L}_i = \ {}^*\Phi_i^\backslash[\bar{\mathbf{L}}_i] \ = \ \mathbf{F}_i^{-1} \cdot \bar{\mathbf{L}}_i \cdot \mathbf{F}_i \ = \ -\frac{1}{2} \dot{\mathbf{C}}_i^{-1} \cdot \mathbf{C}_i. \tag{3.64}$$

and where ${}^{*}\Phi_{i}^{\backslash}[.]$ is an inelastic pull-back operator. Then we multiply the two sides of Eq.(3.64) with $2\mathbf{C}_{i}^{-1}$ and obtain

$$\dot{\mathbf{C}}_{i}^{-1} = -2\,\mathbf{L}_{i}\cdot\mathbf{C}_{i}^{-1}. \tag{3.65}$$

Applying an exponential map integrator to the above flow rule (3.65) and using the transformation rule Eq.(A.8), we obtain (see e.g. [85], [23], [73])

$$
\begin{aligned}
{}^{n+1}\mathbf{C}_{i}^{-1} &= \exp\left[-2\,{}^{n+1}\mathbf{L}_{i}\right]\cdot{}^{n}\mathbf{C}_{i}^{-1} \\
&= \exp\left[-2\,{}^{n+1}\mathbf{F}^{-1}\cdot\,\mathbf{l}_{i}\cdot\,{}^{n+1}\mathbf{F}\right]\cdot{}^{n}\mathbf{C}_{i}^{-1}.
\end{aligned}
\tag{3.66}
$$

In order to integrate the plastic strain rate growth in Eq.(III) and the hardening stresses in Eq.(VI) of Table 3.1, we use an Euler backward rule

$$
\begin{aligned}
{}^{n+1}e_{v} &= {}^{n}e_{v} + \Delta e_{v}, \\
{}^{n+1}Q_{1} &= {}^{n}Q_{1} + \Delta Q_{1}, \\
{}^{n+1}Q_{2} &= {}^{n}Q_{2} + \Delta Q_{2}
\end{aligned}
\tag{3.67}
$$

with

$$
\begin{aligned}
\Delta e_{v} &= \Delta\lambda, \\
\Delta Q_{1} &= \frac{\Delta\lambda\left(H_{1} - c^{n}Q_{1}\right)\mathcal{J}}{1 + \Delta\lambda c}, \\
\Delta Q_{2} &= \Delta\lambda H_{2}\mathcal{J}.
\end{aligned}
\tag{3.68}
$$

Here $\Delta\lambda$ is obtained from the loading/unloading conditions of Eq.(3.39).

The martensite phase fraction z_{M} and its increment Δz_{M} at the new time step ${}^{n+1}t$ can be obtained from Eq.(III.2) of Table 3.2 for given temperature ${}^{n+1}\theta$

1. ${}^{n+1}z_{M} = \Delta z_{M} + {}^{n}z_{M},$

2. $\Delta z_{M} = \begin{cases} \dfrac{{}^{n}\theta - {}^{n+1}\theta}{k_{\theta}\Delta t}\left(1 - {}^{n}z_{M}\right), & \text{for } \theta(t) \leq \theta_{MS} \text{ and } {}^{n+1}\theta < {}^{n}\theta \\ -\Delta z_{A}, & \text{else} \end{cases}$ $\quad\cdot$ (3.69)

In the same way the austenite fraction ${}^{n+1}z_{A}$ can be calculated as

1. ${}^{n+1}z_{A} = \Delta z_{A} + {}^{n}z_{A},$

2. $\Delta z_{A} = \begin{cases} \mu_{MA}\left(1 - {}^{n}z_{A}\right), & \text{for } \theta(t) \geq A_{c1} \\ -\Delta z_{M}, & \text{else} \end{cases}$ $\quad\cdot$ (3.70)

From now on, we neglect the index $n+1$ referring to the actual time step for simplicity. Inserting Eq.(3.66) into (A.2.2) and using the relation $\exp\left[\mathbf{F}^{-1}\cdot\mathbf{A}\cdot\mathbf{F}\right] = \mathbf{F}^{-1}\cdot\exp\left[\mathbf{A}\right]\cdot\mathbf{F}$ we obtain

$$\mathbf{b}_{e} = \mathbf{F}\cdot\mathbf{C}_{i}^{-1}\cdot\mathbf{F}^{t} = \exp\left[-2\mathbf{l}_{i}\right]\cdot\mathbf{b}^{tr}, \quad \text{where } \mathbf{b}^{tr} = \mathbf{F}\cdot{}^{n}\mathbf{C}_{i}^{-1}\cdot\mathbf{F}^{t}. \tag{3.71}$$

Here $\mathbf{b}^{tr}$ is referred to as the left elastic Cauchy Green trial tensor. Then, $\mathbf{b}_e$ is decomposed into a volumetric and a deviatoric part according to Eq.(A.6). Taking the logarithm we obtain the spatial logarithmic Hencky strains

$$
\begin{aligned}
&1. \quad \ln J_e \;=\; \ln J^{tr}, &&\text{where } J^{tr} = \det[\mathbf{b}^{tr}]^{1/2} \\
&2. \quad \ln \hat{\mathbf{b}}_e \;=\; \ln \hat{\mathbf{b}}^{tr} - 2\mathbf{g}^{\sharp} \cdot \mathbf{l}_i^t, &&\text{where } \hat{\mathbf{b}}^{tr} = J^{tr\,-2/3}\mathbf{b}^{tr}.
\end{aligned}
\tag{3.72}
$$

Following Eq.(2.30), Eq.(2.33), Eq.(3.63.1) and Eq.(3.63.2), the Kirchhoff stress tensor $\boldsymbol{\tau}$ renders

$$
\begin{aligned}
&1. \quad \boldsymbol{\tau} \;=\; \mathbf{g}^{\sharp} \cdot \mathbf{m} = \boldsymbol{\tau}^{vol} + \boldsymbol{\tau}^{dev}, \quad \text{where} \\[4pt]
&2. \quad \boldsymbol{\tau}^{vol} \;=\; K[\theta]\ln J^{tr}\mathbf{g}^{\sharp} - K[\theta]\left(3\Delta\theta\,\alpha_M[\theta] + K_{tv}z_A\right)\mathbf{g}^{\sharp} \\[8pt]
&3. \quad \boldsymbol{\tau}^{dev} \;=\; \boldsymbol{\tau}^{dev,tr} - 2G\Delta\lambda\sqrt{\frac{3}{2}}\frac{\boldsymbol{\tau}^{dev}}{||\boldsymbol{\tau}^{dev}||} \\[8pt]
&\qquad\qquad\qquad -3G\boldsymbol{\tau}^{dev}\begin{cases} f'[z_A]\Delta z_A K_{tpA} & \text{for } \dot{z}_A \geq 0 \\[6pt] f'[z_M]\Delta z_M K_{tpM} & \text{for } \dot{z}_A < 0 \end{cases},
\end{aligned}
\tag{3.73}
$$

where

$$
\boldsymbol{\tau}^{dev,tr} = G\mathrm{dev}\ln\mathbf{b}^{tr}.
\tag{3.74}
$$

From Eq.(3.73.3) we conclude, that $\boldsymbol{\tau}^{dev,tr}$ and $\boldsymbol{\tau}^{dev}$ are coaxial, such that the equations (3.73) can be rewritten as

$$
\begin{aligned}
&1. \quad \boldsymbol{\tau} \;=\; \boldsymbol{\tau}^{vol} + \boldsymbol{\tau}^{dev}, \quad \text{where} \\[4pt]
&2. \quad \boldsymbol{\tau}^{vol} \;=\; \frac{1}{3}\,{}^{\tau}I_1\mathbf{g}^{\sharp}, \quad \frac{1}{3}\,{}^{\tau}I_1 = K[\theta]\ln J^{tr} - K[\theta]\left(3\Delta\theta\,\alpha_M[\theta] + K_{tv}z_A\right) \\[6pt]
&3. \quad \boldsymbol{\tau}^{dev} \;=\; \frac{1}{C_p}\left(\boldsymbol{\tau}^{dev,tr} - 2G\sqrt{\frac{3}{2}}\Delta\lambda\mathbf{n}\right), \quad \mathbf{n} = \frac{\boldsymbol{\tau}^{dev,tr}}{||\boldsymbol{\tau}^{dev,tr}||}, \\[8pt]
&4. \quad C_p \;=\; 1 + 3G\begin{cases} f'[z_A]\Delta z_A K_{tpA} & \text{for } \dot{z}_A \geq 0 \\[6pt] f'[z_M]\Delta z_M K_{tpM} & \text{for } \dot{z}_A < 0 \end{cases}.
\end{aligned}
\tag{3.75}
$$

3.4.2 Spectral decomposition

Due to the fact that $\mathbf{b}^{tr}$ and $\boldsymbol{\tau}$ have identical principal axes, and using a spectral decomposition of the left elastic Cauchy Green trial tensor $\mathbf{b}^{tr}$, we have

$$
1.\ \mathbf{b}^{tr} = \sum_{A=1}^{3}\left(\lambda_A^{tr}\right)^2 \mathbf{m}_A \quad \Longrightarrow \quad 2.\ \boldsymbol{\tau} = \sum_{A=1}^{3}\beta_A\mathbf{m}_A.
\tag{3.76}
$$

Here $\left(\lambda_A^{tr}\right)^2$ and $\mathbf{m}_A$, $A = 1,2,3$ are the eigenvalues and eigenbasis of $\mathbf{b}^{tr}$, respectively. β_A, $A = 1,2,3$ are the principal values of the Kirchhoff stresses which by use of the

vector/matrix notations

$$
\underline{\varepsilon}^{tr} := \begin{bmatrix} \ln \lambda_1^{tr} \\ \ln \lambda_2^{tr} \\ \ln \lambda_3^{tr} \end{bmatrix} , \quad \underline{\beta} := \begin{bmatrix} \beta_1 \\ \beta_2 \\ \beta_3 \end{bmatrix} . \tag{3.77}
$$

$\underline{\beta}$ can also be decomposed as

$$
\begin{aligned}
1. \quad & \underline{\beta} &=& \underline{\beta}^{vol} + \underline{\beta}^{dev} \\
2. \quad & \underline{\beta}^{vol} &=& \frac{1}{3} \, {}^{\beta}I_1 (\beta_1 + \beta_2 + \beta_3)\underline{1} = (K[\theta]\underline{1} \cdot \underline{\varepsilon}^{tr} - K[\theta] \, (3\Delta\theta \, \alpha_M[\theta] + K_{tv}z_A))\, \underline{1} \\
3. \quad & \underline{\beta}^{dev} &=& \frac{1}{C_p} \left(\underline{\beta}^{dev,tr} - 2G\sqrt{\frac{3}{2}}\Delta\lambda\underline{\nu} \right), \quad \underline{\nu} = \frac{\underline{\beta}^{dev,tr}}{||\underline{\beta}^{dev,tr}||}
\end{aligned} \tag{3.78}
$$

with vector/matrix notations

$$
\underline{1} := \begin{bmatrix} 1 \\ 1 \\ 1 \end{bmatrix} , \quad \underline{I}_3 := \begin{bmatrix} 1 & & \\ & 1 & \\ & & 1 \end{bmatrix} , \quad \underline{I}_3^{dev} := \underline{I}_3 - \frac{1}{3}\underline{1} \otimes \underline{1}. \tag{3.79}
$$

These sets of equations can be regarded as the counterpart of the relations (3.75) in principal directions. Note, that the above structure is completely identical to the update scheme presented in MAHNKEN *et al.* [56] within a geometrically linear theory, see also SIMO [73]. The yield function defined in Eq.IV of Table 3.1 is written in terms of principal stresses as

$$
1. \quad \phi = \sigma_v - (Y_0 + Q_1 + Q_2)\,\mathcal{J}, \quad \text{where} \quad 2. \quad \sigma_v = \sqrt{\frac{3}{2}}||\underline{\beta}^{dev}||. \tag{3.80}
$$

3.4.3 Local iteration

Due to the fact that the resulting system of equations (3.78) is completely identical to the structure of the geometrically linear case, the results of MAHNKEN *et al.* [56] can directly be transferred. From Eq.(3.78.3) we obtain the scalar relation

$$
\left\| \underline{\beta}^{dev} \right\| = \frac{\left\| \underline{\beta}^{dev,tr} \right\| - 2G\sqrt{\frac{3}{2}}\Delta\lambda}{C_p}, \tag{3.81}
$$

where C_p is formulated in (3.78.4). Next, by use of the result (3.81) the yield condition (3.80.1) is written as a residual

$$
\Phi[\Delta\lambda] = \sqrt{\frac{3}{2}}\frac{\left\| \underline{\beta}^{dev,tr} \right\| - 2G\sqrt{\frac{3}{2}}\Delta\lambda}{C_p} - \left(Y_0 + {}^{n+1}Q_1 + {}^{n+1}Q_2 \right)\mathcal{J} = 0. \tag{3.82}
$$

In this way the discretized rate equations (3.65) and (3.67.1) are reduced to a one-dimensional problem, which is completely formulated in terms of the plastic multiplier $\Delta\lambda$. For its solution a Newton method can be used as follows

$$
\begin{aligned}
1. \quad \Delta\lambda_{(k+1)} &= \Delta\lambda_k - \frac{\Phi[\Delta\lambda_k]}{J[\Delta\lambda_k]}, \quad k = 0, 1, 2, \ldots, \quad \text{where} \\
2. \quad J[\Delta\lambda] &= \frac{\partial\Phi[\Delta\lambda]}{\partial\Delta\lambda} = -\left(\frac{3G}{C_p} + \frac{\partial\Delta Q_1}{\partial\Delta\lambda} + \frac{\partial\Delta Q_2}{\partial\Delta\lambda}\right) \\
&= -\left(\frac{3G}{C_p} + \frac{(H_1 - c^n Q_1)\,\mathcal{J}}{(1 + \Delta\lambda c)^2} + H_2\mathcal{J}\right),
\end{aligned}
\tag{3.83}
$$

and where the index k refers to the iteration number.

3.4.4 Spatial algorithmic tangent operator

According to SIMO [73] the spatial algorithmic tangent operator $\mathbb{c} = 2\partial\boldsymbol{\tau}/\partial\mathbf{g}^\flat$ required for the iterative solution of the finite-element equilibrium iteration, is calculated as

$$
\mathbb{c} = \sum_{A=1}^{3}\sum_{B=1}^{3} \frac{d\beta_A}{d\varepsilon_B^{tr}}\mathbf{m}_A \otimes \mathbf{m}_B + \sum_{A=1}^{3} 2\beta_A \frac{d\mathbf{m}_A}{d\mathbf{g}^\flat},
\tag{3.84}
$$

where the result for $d\mathbf{m}_A/d\mathbf{g}^\flat$ is given in [73]. The quantities $d\beta_A/d\varepsilon_B^{tr}$ and $d\beta_A/dJ$ are obtained by straightforward differentiation of β_A in Eq.(3.78). Using the vector notation introduced in Section 3.4.2 we have

$$
\begin{aligned}
\frac{d\underline{\beta}}{d\underline{\varepsilon}^{tr}} &= K\underline{1} \otimes \underline{1} + \frac{2G}{C_p}\underline{I}_3^{dev} - \sqrt{\frac{3}{2}}\Delta\lambda\frac{(2G)^2}{C_p}\frac{1}{\left\|\underline{\beta}^{dev,tr}\right\|}\left(\underline{I}_3^{dev} - \underline{1} \otimes \underline{1}\right) \\
&\quad - \sqrt{\frac{3}{2}}\left(\frac{2G}{C_p}\right)^2\frac{1}{J[\Delta\lambda]}\underline{1} \otimes \underline{1},
\end{aligned}
\tag{3.85}
$$

where $J[\Delta\lambda]$ is defined in Eq.(3.83).

3.5 Representative examples

In this section two numerical examples are presented. In the ensuing subsection 3.5.1 experimental data for a steel AISI 52100 in a Hardness of 62 HRC are used for parameter identification of the constitutive equations of the previous Section 3.2. In a second example the material model is applied in subsection 3.5.2 in order to investigate a cutting process.

3.5.1 Steel AISI 52100 under tension, compression and shear as well as phase-transformation

This section exhibits simulations of the material behavior for steel AISI 52100 with our multi-mechanism modell. The chemical composition of this material is listed in Table 3.3.

As a main goal the corresponding material parameters are identified. To this end two sets of experimental data have been used:

1. Thermal-mechanical tests: This set of experiments takes into account different temperatures, strain rates and stress modes (e.g. tension, compression and torsion). However, only data for temperatures below A_{c3} are available, and thus only valid for pure martensite.

2. Dilatometer tests: The second set of experiments covers a broad temperature range - above and below the martensitic start temperature M_s - thus taking into account the TRIP effect. However, stresses are below the yield stress of the two phase material. Furthermore, we note, that the behaviour of phase transformation subjected to the conditions of high rates, as in the cutting process has not been considered so far experimetally.

C %	Si %	Mn %	P %	S %	Cr %	Mo %	Ni %	Al %	Cu %	Ti %
$0.93 - 1.05$	0.19	0.41	0.01	0.01	1.43	0.05	0.10	0.01	0.11	< 0.001

Table 3.3: Chemical composition of AISI 52100

For parameter identification based on experimental testing a least-squares functional is considered as an identification criterion in order to minimize the distance of the simulated data to the experimental data. The least-squares problem reads:

$$f(\kappa) = \tfrac{1}{2}||\mathbf{d}(\kappa) - \overline{\mathbf{d}}||_2^2 \to \min(\kappa \in \mathcal{K}), \quad \text{where}$$
$$\mathcal{K} = \prod_{i=1}^{n_p} \mathcal{K}_i, \quad \mathcal{K}_i := \{a_i \le \kappa_i \le b_i\}$$

(3.86)

Here, $\mathbf{d}(\kappa)$ are the simulated data, which depends on the parameters κ. $\overline{\mathbf{d}}$ are the experimental data. a_i, b_i are lower and upper bounds for the material parameters. n_p represents the number of the parameters which are needed to be identified.

A general framework and technical details for the minimization of the least-squares functional is presented elsewhere, see e.g. [53, 54] for more details.

Thermal-mechanical tests

Thermal-mechanical tests were performed at different strain rates and different temperatures in order to account for rate and temperature dependency. Concerning specimen geometry and performance of the experiments we refer to HALLE [33]. So far experimental results are available with data according to the nomenclature in Table 3.4. There are different strain rates and temperatures for different loading types applied. The strain rate $\dot{\varepsilon}$ can be approximately respected as the time derivation of the equivalent plastic strain of Eq.(3.44) with $\dot{\varepsilon} \approx \dot{e}_v$.

All specimens used in the experiments were made and all tests were performed by the company Nordmetall, Adorf, Germany. In the sequel we give a brief overview on performence of the experiments.

Notation	Strain rate $\dot{\varepsilon}$ $[s^{-1}]$	Tension (t) /Compression (c) /Shear (s)	Temperature θ $[^{o}C]$
T-R0001-T20	0.001	Tension	20
T-R1000-T20	1000	Tension	20
T-R100-T200	100	Tension	200
T-R100-T400	100	Tension	400
T-R100-T600	100	Tension	600
C-R0001-T20	0.001	Compression	20
C-R01-T20	0.1	Compression	20
C-R184-T20	184	Compression	20
C-R1890-T20	1890	Compression	20
C-R183-T400	183	Compression	400
C-R185-T600	185	Compression	600
S-R01-T20	0.1	Shear	20
S-R100-T200	100	Shear	200
S-R100-T400	100	Shear	400

Table 3.4: Summary of mechanical tests for AISI 52100

Tension tests: The quasi-static tensile tests at strain rates of 0.001 s^{-1} and at room temperature are performed using a mechanical universal testing machine with a maximum load of 100 kN. The dynamic-impact tensile tests are performed using a rotating wheel machine. Figure 3.1.a shows the schematic illustration of the testing device. It consists of a flywheel, in which a claw is locked at the beginning of the test. The flywheel is accelerated with an electrical drive to the required speed $\dot{\varphi}$. If the testing velocity is reached, the claw is released and is aligned due to the acting centrifugal force. As the lower part of the specimen is fixed in a pile, the specimen is deformed abruptly, when the claw impacts the pile. Due to the high energy capacity of the flywheel machine, the material is deformed until failure without a significant loss of the impact velocity.

Compression tests: For the investigations under compressive loading, specimens with a diameter of ϕ6 mm and a height of 6.5 mm are used. The quasi-static and quasi-dynamic tests at strain rates of 0.001 and 0.1 s^{-1} are performed on a universal testing machine with a maximum load of 100 kN. Forces were measured using a calibrated load cell. The impact dynamic compression tests at strain rates of ca. 10^2 s^{-1} are performed using a drop weight machine. A schematic illustration of the testing device is shown in Figure 3.1.b. A falling mass (B) of 600 kg is guided in a four column frame (A). The punch (C) is mounted on the lower side of the falling mass and impacts the specimen (E), which is

adjusted to an anvil (D). After the deformation of the specimen, the mass is stopped by mechanical stopping devices (F) and caught by a hydraulic brake. Using this technique, a second impact of the mass to the specimen is avoided and the deformed specimen can be used for further investigations, e.g. microstructure analysis. The dynamic force is measured directly on the punch (C). The dynamic deformation is measured using an electro-optical gage (G). Beside room temperature testing, the drop weight machine was also used for dynamic compression tests at elevated temperatures. The specimens were heated up using an inductive coil setup.
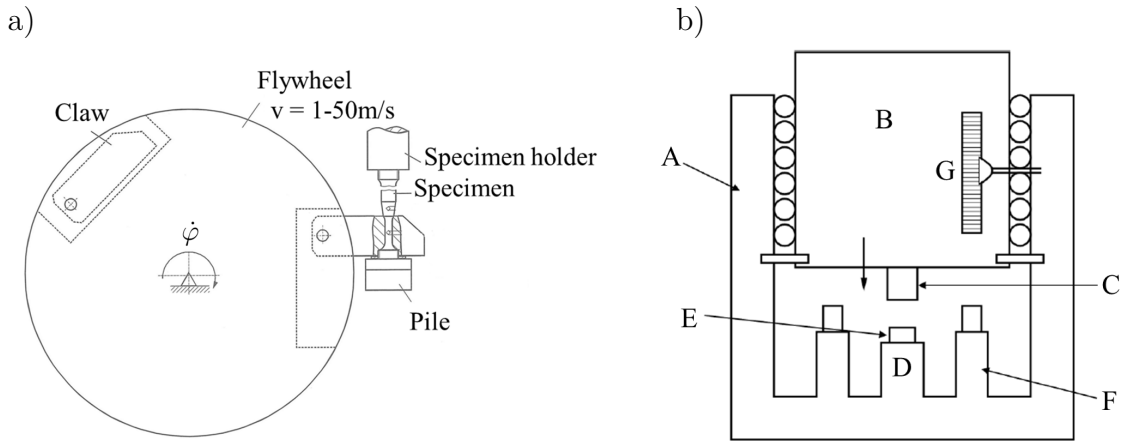
Figure 3.1: Test devices: a) Principle of high-rate tensile testing with flywheel setup [7], b) Scheme of a drop weight machine used for dynamic compression loading: A) frame, B) drop weight, C) punch, D) anvil, E) specimen, F) stopping device, and G) incremental gage [7].

High dynamic compression tests at strain rates greater than 10^3 s^{-1} were performed using a Split-Hopkinson-Pressure-Bar setup (SHPB), which is schematically shown in Figure 3.2. A striker bar impacts an incident bar and an elastic pressure wave is developed. The pressure wave propagates through the incident bar and reaches the specimen, which is located between the incident and the transmitter bar. As the amplitude of the incoming pressure wave is larger than the yield strength of the specimen, the specimen is deformed plastically. Hence, a part of the incoming stress wave is transmitted to the transmitter bar and the other part is reflected as a tensile stress wave in the incident bar. Applying the principles of one dimensional elastic wave propagation in slim bars, the stress-strain response of the material can be calculated.

Torsion tests: Experimental investigations under torsion loading are performed using a high rate testing machine, which is available at Chemnitz University of Technology, see Figure 3.3. The machine is developed for experimental investigations of materials under monotonic and cyclic torsion loading. Furthermore, a wide range of strain rates from 10^{-3} to 10^2 s^{-1} can be realized in the machine. For the dynamic tests at strain rates of 10^2 s^{-1}, the specimen is fixed at the lower end of a Hopkinson bar. According to the principle of a flywheel machine, a flywheel mass is accelerated. If the required testing velocity is
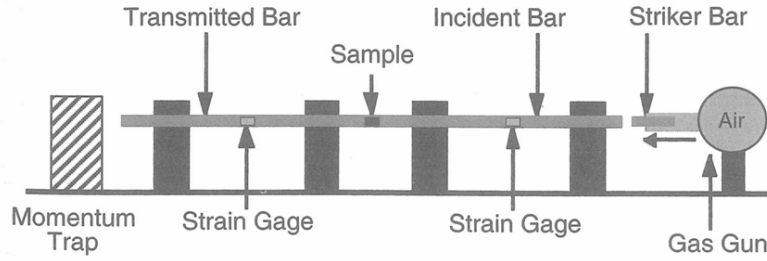
Figure 3.2: Schematic of a compression Split-Hopkinson-Pressur-Bar (SHPB) [7]

reached, the specimen is impact loaded up to failure using a thread-quick-coupling device. Applying the Hopkinson principle, the torque of the specimen is measured using the Hopkinson bar. At room temperature, the transition from elastic to elastic-plastic flow of the specimen is measured with a strain gage applied directly on the specimen. Higher plastic deformations and the plastic deformation at high temperature torsion tests are calculated from the torsion angle. The specimens were heated using an inductive heating device.
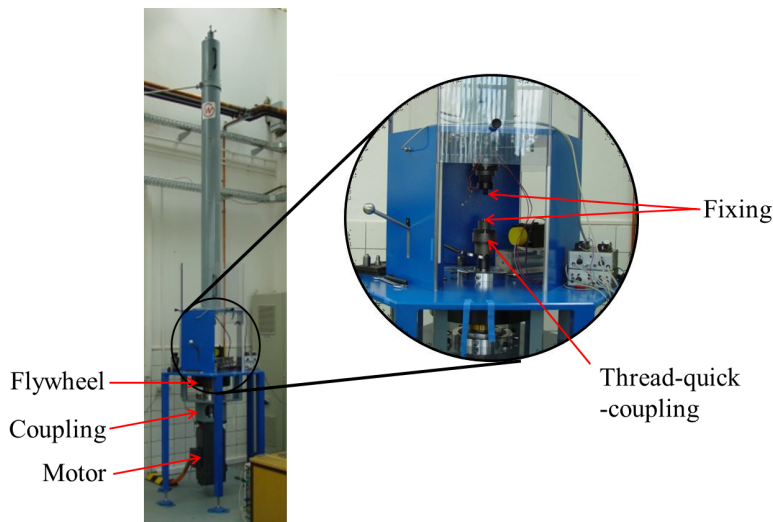
Figure 3.3: Torsion test machine

Using the experimental data at room temperature but different strain rates (C-R0001-T20, C-R01-T20, C-R184-T20 and C-R1890-T20) we can study the dependence of the strength on the logarithm of strain rate and prove the improvement by using Huh-Kang form of Eq.(3.44). Figure 3.4 shows the effective stresses dependent on the strain rates. Each point represents the effective stresses at different strain rates with 5% effective plastic strain. These points exhibit a clear bi-linear dependence of the effective stresses on the logarithm of strain rate. The straight line represents the simulated result of Johnson-Cook rate form of Eq.(3.30.4) and the curved line exhibits the result of Huh-Kang form of Eq.(3.44). In comparison, the Huh-Kang form provides a perfect agreement

between simulated and experimental data. As a consequence, an essential improvement is achieved by using the Huh-Kang form.
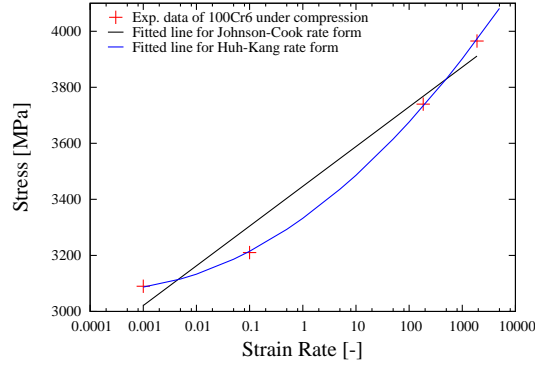
Figure 3.4: Strain rate data for AISI 52100 under compression (Chauchy stress and strain)

Using the same conditions (strain rate, temperature and loading type) of the tests summarized in Table 3.4, simulations of the visco-plasticity model (Table 3.1) are investigated. Figure 3.5 and 3.6 illustrate the resulting stress strain curves of the experimental and the simulated data. The results in Figure 3.5.a show an identical elastic behavior and a different inelastic behavior for the tensile tests T-R01-T20 and T-R1000-T20 as well as for the compressive tests C-R0001-T20, C-R01-T20, C-R184-T20 and C-R1890-T20 with the same temperature but different strain rates. A strong strain rate dependency can be seen. In addition, the temperature dependence is illustrated in Figure 3.5.b for tension as well as for compression, where the experimental tests T-R100-T200, T-R100-T400 and T-R100-T600 for tension as well as C-R184-T20, C-R183-T400 and C-R185-T600 for compression are used.

Furthermore, all tensile and compressive curves of the above tests are summarized in Figure 3.6.a. As can be seen, the stress level under tension is clearly lower than under compression. Moreover, Figure 3.6.b shows the results of torsion tests and simulations, where the inelastic behavior for torsion is different in comparison to tension and compression. These two figures also verify the existence of the SD-effect that was considered in our model by using the concept of the weighting functions Eq.(3.45)

The constitutive equations of Section 3.3 for the visco-plastic model of Table 3.1 have been used by setting $S = 3$ thus referring to three types of experiments in tension, compression and shear. Analogously to the procedure in MAHNKEN [50] the material parameters listed in this table were obtained in a consecutive manner. The tension-compression data were used to obtain parameters of $\boldsymbol{\kappa}_{p1}$ for tension as well as $\boldsymbol{\kappa}_{p2}$ for compression. In a second phase the shear data were added thus obtaining $\boldsymbol{\kappa}_{p3}$ to the final results summarized in Table 3.5.
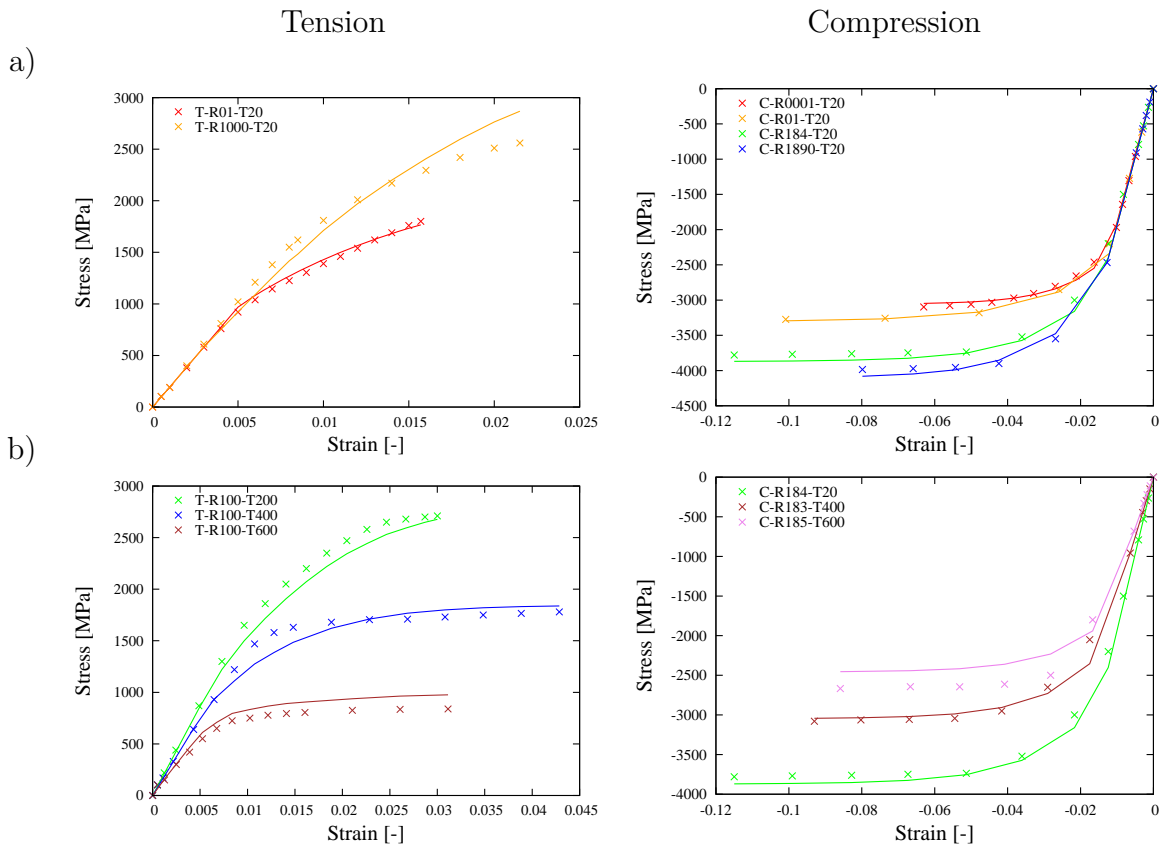
Figure 3.5: Steel AISI 52100: Chauchy Stress-strain curves a) with same temperature, different strain rates, b) different temperatures, almost same strain rate. Symbols refer to experiment, solid lines to simulation.
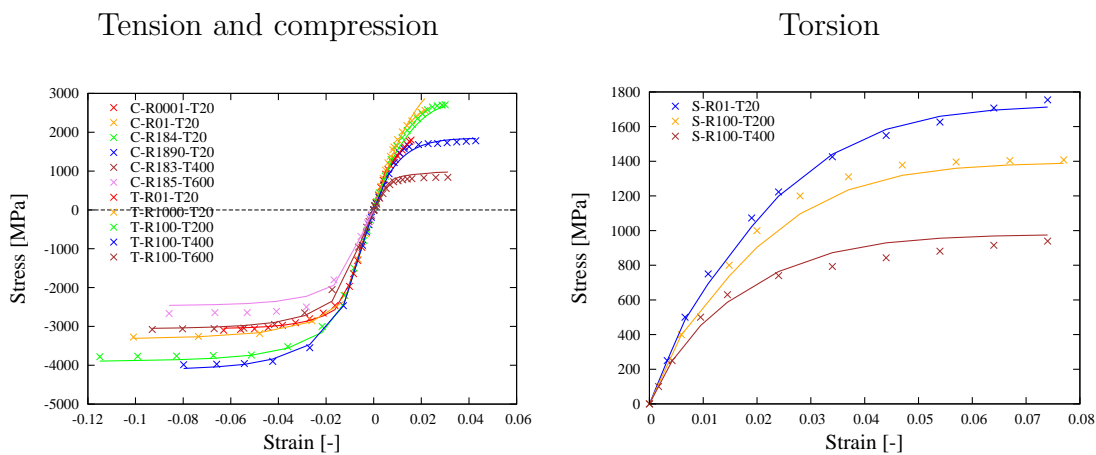
Figure 3.6: Steel AISI 52100: Chauchy Stress-strain curves under tension, compression and torsion. Symbols refer to experiment, solid lines to simulation

$\boldsymbol{\kappa}_{el}$:	E_0 [MPa]	ν [$-$]	$c_E[\frac{\text{MPa}}{°\text{C}}]$	θ_{E_0} [°C]
	1.96E+05	0.28	113.35	20
$\boldsymbol{\kappa}_{pl}$:	Y_{01} [MPa]	Y_{02} [MPa]	Y_{03} [MPa]	H_{11} [MPa]
	1.475E+03	2.0953E+03	1.7066E+03	1.4875E+05
	H_{12} [MPa]	H_{13} [MPa]	H_{21} [MPa]	H_{22} [MPa]
	1.4875E+05	1.4875E+05	1.97E-02	1.97E-02
	H_{23} [MPa]	c_1 [$-$]	c_2 [$-$]	c_3 [$-$]
	1.97E-02	2.61E+02	2.61E+02	2.61E+02
	C_{11} [$-$]	C_{12} [$-$]	C_{13} [$-$]	C_{21} [$-$]
	2.91E-02	2.55E-02	2.39E-02	1.1E-03
	C_{22} [$-$]	C_{23} [$-$]	$\dot{\varepsilon}_{01}$ [$-$]	$\dot{\varepsilon}_{02}$ [$-$]
	8.1E-04	5.1E-04	1.0E-05	1.0E-05
	$\dot{\varepsilon}_{03}$ [$-$]	m_1 [$-$]	m_2 [$-$]	m_3 [$-$]
	1.0E-05	7.23E-01	1.1E+00	0.7E-01
$\boldsymbol{\kappa}_{\theta}$:	α_M [$\frac{1}{°\text{C}}$]			
	0.884e-5			
$\boldsymbol{\kappa}_{tp}$:	K_{tpA} [$\frac{1}{\text{MPa}}$]	K_{tpM} [$\frac{1}{\text{MPa}}$]	μ_{MA} [$-$]	k_{θ} [$\frac{1}{°\text{C}}$]
	1.37E-04	1.03E-04	4.857	0.013
$\boldsymbol{\kappa}_{co}$:	θ^m [°C]	θ^r [°C]	ρ_M [$\frac{\text{kg}}{\text{mm}^3}$]	ρ_A [$\frac{\text{kg}}{\text{mm}^3}$]
	1420	20	7.765	8.03
	A_{c1} [°C]	θ_{MS} [°C]		
	504	211		

Table 3.5: Material parameters for steel AISI 52100

The comparison of the simulated data to the experimental data is also shown in Figure 3.5 and Figure 3.6, where the solid lines refer to simulated data. In all diagrams, a good agreement between experiment and simulation is obtained. However, we are aware, that more tests are required for a convincing parameter-identification.

Dilatometer tests for TRIP

For determination of the material parameters of κ_θ and κ_{tp} in Table 3.2 representing the stress-strain response of the heating martensite and the under cooled austenite and the TRIP part of the material AISI 52100 (1.3505), so called dilatometer tests are used, which were performed by the Leibniz-Institut für Werkstofforientierte Technologien (IWT), University of Bremen. The thermo-mechanical simulator Gleeble(R) 3500 is used which combined the properties of a hydraulic testing machine with those of a quenching dilatometer. The machine was upgraded by a laser extensometer which allows the measurement of longitudinal and transversal strains. There were different types of dilatometer tests investigated with respect to austenitization and martensitic transformation. For both types of tests the specimens have the same geometry as illustrated in Figure 3.7. On details for specimen preparation and the loading process we refer to AHRENS [3].
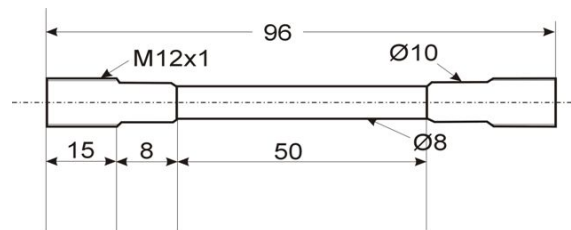
Figure 3.7: Dilatometer tests for AISI 52100: Geometry of the specimen.

Austenitization: In order to determine the material parameters of κ_{tp} in Table 3.2 related to austenitization and its TRIP, dilatometer tests are investigated under different stress loadings during heating. The tests are summarized with the following nomenclature:

Notation	Stress σ_A [MPa]
A − 5	−5
A0	0
A5	5
A10	10
A15	15
A20	20
A25	25

The specimens fully consist of martensite (62 HRC). They were heated up to $\theta_{max} = 1000°C$ with a constant heating rate 20K/s, where the longitudinal and radial strain are

measured. A schematic illustration of the temperature θ and the loaded stresses σ_A in time is shown in Figure 3.8. For details of the testing construction and process we refer to AHRENS [3] and MAHNKEN *et al.* [55].
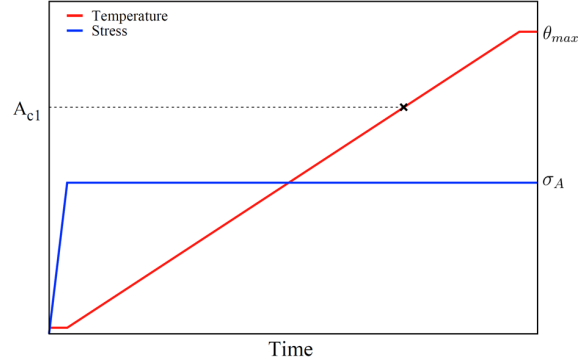
Figure 3.8: Dilatometer tests for AISI 52100: Schematic of temperature and stress loading with respect to austenitization

Figure 3.9.a shows the longitudinal strains under different stress loadings over the temperature. According to the phase transformations the curves are decomposed into five phases illustrated in Fig. 3.9.b. In order to express the difference between loaded and unloaded cases we compare the two curves A0 and A5 in this diagram. In phase I, the specimens are heated from room temperature (ca. 15 °C) to 420 °C. The strain curve A0 without stress loading is linear due to a pure thermal loading. In comparison the curve A5 with stress loading has not only thermal strain but also an additional creep strain because of 5 MPa stress loading. Phase II begins with tempering at ca. 420 °C and ends at ca. 460 °C, the slopes of both curves are smaller due to volume reduction of the tempering. In phase III, analogously to phase I, because of the additional creep strain on A5 the curves A0 and A5 separate further from each other. In phase IV, the large volume reduction indicates that the martensite transforms into austenite (from ca. 760 °C to 770 °C). In phase V, transformation is finished and the specimens are heated further (from ca. 770 °C to 1000 °C).

According to the above explanations, the strain change $\Delta\varepsilon_i^{IV}$ of Ai in phase IV is expressed as

$$\Delta\varepsilon_i^{IV} = \Delta\varepsilon_i^{\theta} + \Delta\varepsilon_i^{cr} + \Delta\varepsilon_i^{tv} + \Delta\varepsilon_i^{tp}, \quad i = -5, 5, 10, 20, 25 \tag{3.87}$$

where $\Delta\varepsilon_i^{\theta}$, $\Delta\varepsilon_i^{cr}$, $\Delta\varepsilon_i^{tv}$ and $\Delta\varepsilon_i^{tp}$ represent the strain changes due to heating, creep, volume change of phase transformation and TRIP under i MPa stress loading, respectively.

According to Eq.(3.47) TRIP-strain can not be induced without stress loading, therefore, the strain change of A0 in phase IV $\Delta\varepsilon_0^{IV}$ reads

$$\Delta\varepsilon_0^{IV} = \Delta\varepsilon_0^{\theta} + \Delta\varepsilon_0^{tv}, \tag{3.88}$$

where $\Delta\varepsilon_0^{\theta}$ and $\Delta\varepsilon_0^{tv}$ represent the strain change due to heating and volume change of phase transformation for the curve A0. Since the stress loading does not affect the
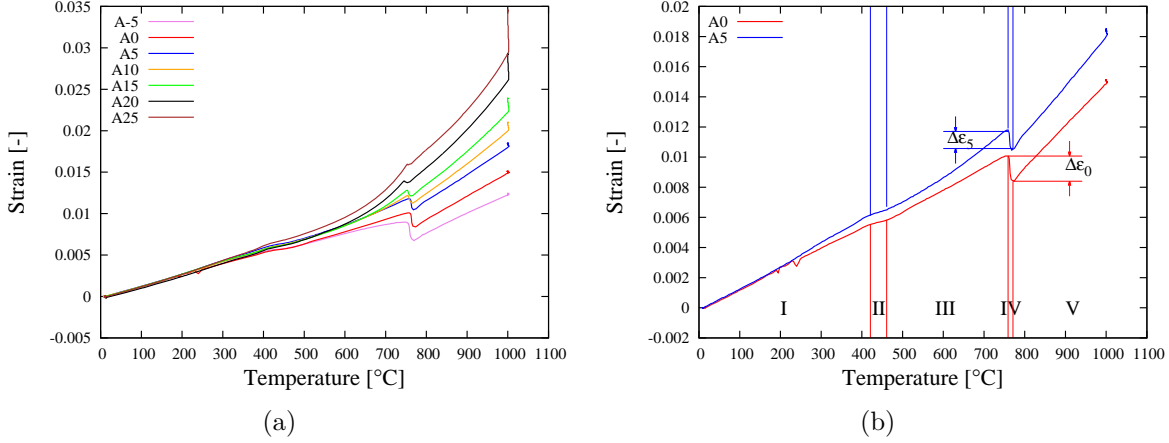
Figure 3.9: Phase transformation for AISI 52100: a) longitudinal strain-temperature curves; b) Decomposition of the transformation in five phases.

thermal strain and volume change of phase transformation, the following relations hold

$$1.\ \Delta\varepsilon_i^\theta = \Delta\varepsilon_0^\theta, \qquad 2.\ \Delta\varepsilon_i^{tv} = \Delta\varepsilon_0^{tv}, \quad \text{where} \quad i = -5, 5, 10, 20, 25. \tag{3.89}$$

Inserting Eq.(3.88) and Eq.(3.89) into Eq.(3.87) solving for $\Delta\varepsilon_i^{tp}$ we obtain

$$\Delta\varepsilon_i^{tp} = \Delta\varepsilon_i^{IV} - \Delta\varepsilon_0^{IV} - \Delta\varepsilon_i^{cr}, \quad i = -5, 5, 10, 20, 25, \tag{3.90}$$

where the creep strain $\Delta\varepsilon_i^{cr}$ can be approximated as

$$\Delta\varepsilon_i^{cr} \approx \Delta\theta \cdot (K_i - K_0), \quad i = -5, 5, 10, 20, 25. \tag{3.91}$$

Here $\Delta\theta$ is the temperature increase in phase IV, K_i and K_0 are the slopes of the curves Ai and A0 at the beginning of the phase V. Note, the thermal expansion α_M in Eq.(I.1) of Table 3.2 can be determined as $\alpha_M = K_0 = 8.84\text{E-6 }^\circ\text{C}^{-1}$.

According to the relations Eq.(3.87-3.91) the TRIP strains $\Delta\varepsilon_i^{tp}$, $i = -5, 5, 10, 20, 25$ are calculated and illustrated in Figure 3.10.a. As shown, the higher the stress σ_A, the larger the TRIP strains. All curves have the same austenite start temperature $A_{c1} = 762°$ C.

Analogously to the procedure in MAHNKEN *et al.* [56] and using the data illustrated in Figure 3.10.a the parameter μ_{MA} in Eq.(3.54) for austenitization and the parameter K_{tpA} in Eq.(3.47) for TRIP of austenitization are obtained as $\mu_{MA} = 4.857$ and $K_{tpA} = 1.37\text{E-3 MPa}^{-1}$. The resulting simulations for the TRIP-temperature curves under stress loadings are shown in Figure 3.10.b. A satisfying agreement with experimental data is obtained.

We are aware that the austenitization start temperature A_{c1} is much lower than 762 °C due to an intense mechanical loading in a cutting process. The new austenitization start temperature A_{c1} can be calculated by a so called Clausius-Clayperon equation proposed by GRIFFITHS [28] and used by RAMESH *et al.* [69]

$$1.\ A_{c1} = A_{c1} + \Delta A_{c1}, \quad 2.\ \Delta A_{c1} = \frac{\sigma_v A_{c1}^{nom} \Delta V_{tr}}{\Delta H_{tr}}, \quad 3.\ \Delta V_{tr} = \frac{M}{\rho_A} - \frac{M}{\rho_M}, \tag{3.92}$$
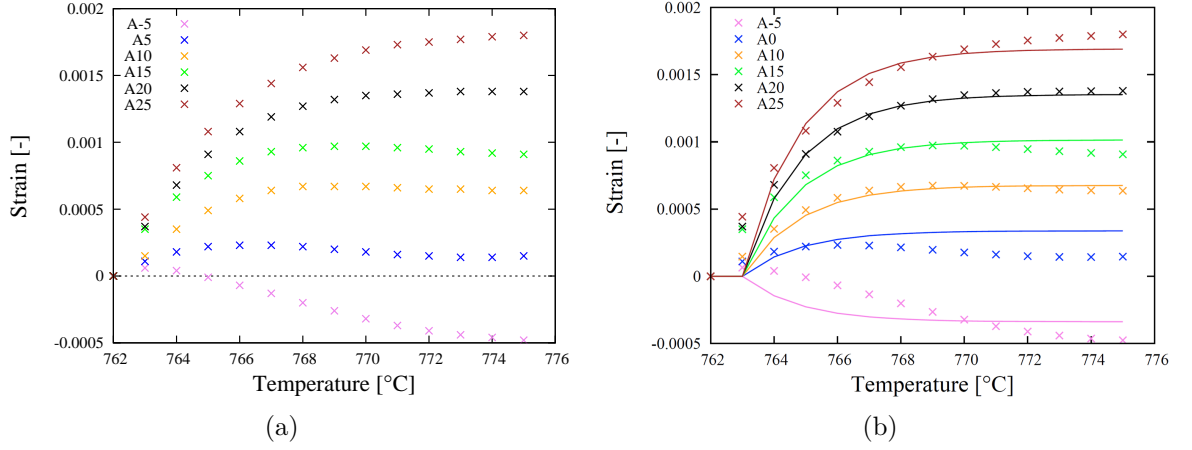
Figure 3.10: TRIP-strains $\Delta\varepsilon_i^{tp}$ for different stress loadings: (a) Experimental data (b) Simulated data (symbols refer to experiment, solid lines refer to simulation)

where ΔV_{tr} is the volume change per mole due to transformation and M is the molar weight. ΔH_{tr} is the heat of transformation involved in the austenitization. According to RAMESH *et al.* [69], the following values are given

1. $\Delta H_{tr} = 215 \text{ cal} = 215 \cdot 41.3 \text{ cm}^3\text{atm} = 8879.5\text{cm}^3\text{atm}$

2. $M = 55.85\text{g}$ \hfill (3.93)

3. $\sigma_v = 1300 \text{ MPa} = 1.28 \cdot 10^4 \text{ atm},$

where the equivalent stress σ_v is assumed to be constant in the shear plane. Furthermore the densities of the austenite and the martensite are determined by ACHT *et al.* [2] $\rho_A = 8.03\text{g/cm}^3$, $\rho_M = 7.765\text{g/cm}^3$. ΔA_{c1} is calculated as

$$\Delta A_{c1} = \frac{1.28 \cdot 10^4 \text{ atm} \cdot 762 \text{ °C} \cdot 55.85\text{g}\left(\frac{1}{8.03\text{g/cm}^3} - \frac{1}{7.765\text{g/cm}^3}\right)}{8879.5\text{cm}^3\text{atm}} = -258 \text{ °C} \quad (3.94)$$

The austenitization temperature A_{c1} for cutting with martensite as the initial phase is reduced to $A_{c1} = 504$ °C. The above identified parameters related to the austenitic transformation are summarized in Table 3.5.

Martensitic transformation: In order to determine the material parameters k_θ, θ_{MS} and K_{tpM} in Table 3.2 related to martensitic transformation, dilatometer tests are investigated under different stress loadings. Different to austenization, the specimens are not hardened in these tests. A schematic illustration of temperature and stress loading with respect to time is shown in Figure 3.11.a. The specimens are heated with constant heating speed 6.2 K/s to arrive the austenitizing temperature $\theta_{max} = 850$°C. For the homogenization of the specimens in the measured length this temperature stays constant for $t_{hold} = 10$ minutes. After that the specimens are cooled with quenching gas (-170 °C), thus resulting into complete martensitic transformation. In order to study the effects of external stresses on the phase transformation behavior, stresses $\sigma_M = -50, 5, 50, 72, 100$

MPa are applied during under cooling. These are applied, when the temperature is approximately 100 °C to 150 °C above the martensitic start temperature. The testing device allows a simultaneous strain measurement in the longitudinal and radial direction. With these data the martensitic Trip-strain related to its velocity $\bar{\mathbf{L}}_t$ and the martensitic fraction z_M in Eq.(3.47) can be calculated, see AHRENS [3] and IRRETIER [39]. Figure 3.11 shows longitudinal strain-temperature curves under tension and compression for experimental results. So far experimental results are available with data according to the following nomenclature:

Notation	Stress σ_M [MPa]
M − 50	−50
M5	5
M50	50
M72	72
M100	100

Analogously to the procedure in MAHNKEN *et al.* [56] the parameters k_θ and θ_{MS} in Eq.(3.55) for the martensitic transformation and K_{tpM} in Eq.(3.47) for TRIP are obtained and summarized in Table 3.5. The resulting simulations for the longitudinal strain-temperature curves under tension and compression are also shown in Figure 3.11. A satisfying agreement with experimental data is obtained.
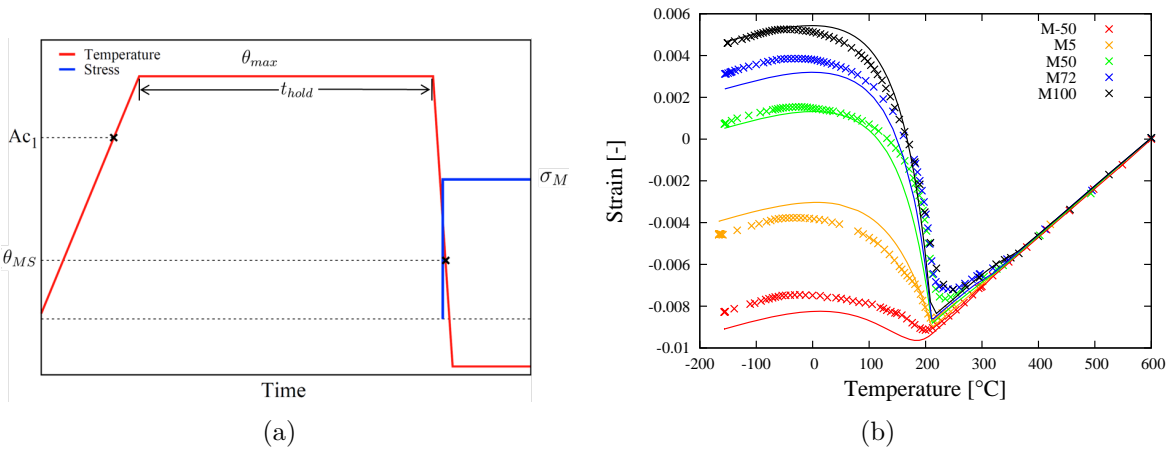
Figure 3.11: a) Phase transformation for AISI 52100: schematic of temperature and stress loading with respect to time; b) Phase transformation for AISI 52100: longitudinal strain-temperature curves. Comparison of experimental and computed results (symbols refer to experiment, solid lines refer to simulation)

3.5.2 Simulation of a cutting process

In this example some cutting simulations are investigated in order to test the material model developed in Section 3.3. To this end, the commercial FEM-software ABAQUS v6.14 is used.

The geometry and the finite-element discretization are shown in Figure 3.12. The dimensions of the workpiece (2D) are the length 500 μm, the height 400 μm. In order to get a realistic chip formation we define a separation layer on the workpiece with a cutting depth d = 100 μm as shown in Figure 3.12. To this layer we assign a simple failure criterion $e_v \leq \mathrm{e}_v^f$ (e_v^f is a constant) in dependence of the effective plastic strain e_v for separating the chip from the workpiece. In this way the separation layer can be deleted during the simulation, which means, that the surface of separation is prescribed. Above the separation layer the meshing is very fine and uniform. Furthermore, a non-uniform meshing is used for the elements below the separation layer, since the elements at the bottom area are not deformed. It can be seen, that the meshing near the separation layer is more fine than that away from it.

Boundary conditions are applied at the bottom and the cutting face of the workpiece as well as the left side and the right side below the cutting surface, while the tool moves in horizontal direction with a constant velocity v. For simplicity, the elements below the separation layer can not move vertically. The initial conditions assume the room temperature (20 °C), and a conventional cooling condition is applied over the surfaces of the workpiece. A 4-node plane strain thermally coupled quadrilateral element (CPE4RT) is used for the workpiece. To model the material behavior of the workpiece the constitutive equations in Section 3.3 and the parameters in Table 3.5 were used, where the equations are implemented as a user-defined material subroutine (VUMAT) for explicit calculations.
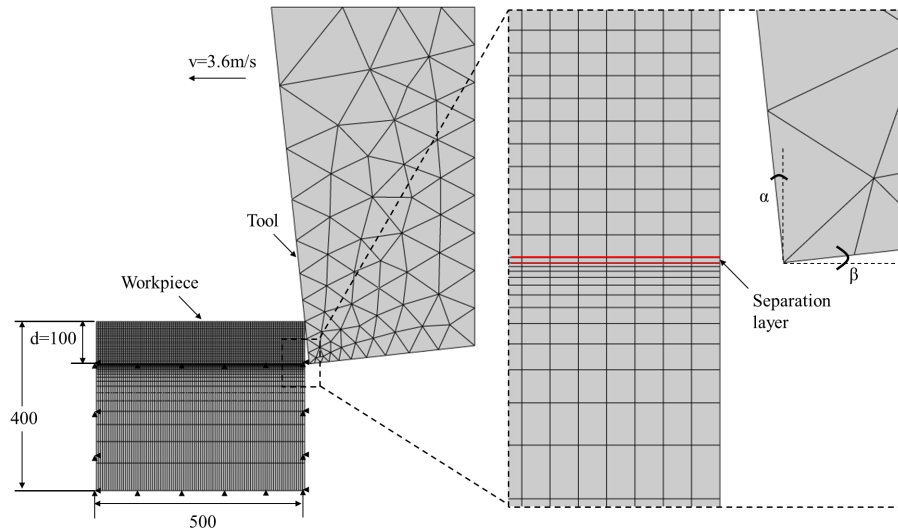
Figure 3.12: Cutting simulation: Geometry and finite-element discretization (dimensions in μm)

The tool is modeled as purely elastic with high elastic modulus, which has a negative rake angle $\alpha = -6°$ and a clearance angle $\beta = 6°$. The element type CPE3T (a 3-node plane strain thermally coupled triangle element) is used. The friction between the workpiece and the tool is quantitatively controlled with a Coulomb friction coefficient f.

Concerning the special scenarios of the cutting process and the mechanisms of the material model, the testing simulations concentrate on the following items:

1. The friction between the workpiece and the tool is an important factor for the cutting process. Its influence on temperature evolution and therefore on white layer formation will be studied.

2. The cutting speed may affect the chip formation and the process temperature, whose influence will also be studied.

3. As a result of the phase transformation and an important part in our model, the influence of the TRIP part $\bar{\mathbf{L}}_t$ of Eq.(3.33) will be studied.

A reference cutting simulation with the friction coefficient $f = 1.5$, cutting speed $v = 3.6$ m/s is selected. Furthermore, the term C_p of Eq.(3.75) is set as $C_p = 1$ while deactivating the TRIP part.

Influence of friction

In order to study the influence of the friction between the tool and the workpiece on the cutting process, another simulation with $f = 0.7$ is investigated and compared to the reference simulation. The comparison is performed for von-Mises stress, temperature, equivalent plastic strain, austenite mass fraction and stress mode factor. The post processing results are shown at time instants $1.14 \cdot 10^{-6}$ s, $2.584 \cdot 10^{-5}$ s, $5.054 \cdot 10^{-5}$ s and $7.6 \cdot 10^{-5}$ s in Figure 3.13, 3.14, 3.15, 3.16 and 3.17, respectively. It is obvious that for both simulations continuous chips are deformed, and the chip for the one with smaller cutting friction, $f = 0.7$, is more blended.

Figure 3.13 shows that the von-Mises stress of both simulations concentrate on the shear zone. The stress has almost no difference in the cutting zone. On the contact surface, due to temperature difference (see Figure 3.14) the stress with lower friction is higher than the one with higher friction. This can be explained using the temperature dependence of the yield function (3.30.1). Due to mechanical dissipation the temperature locates near the tool tip in the deformation zone of the workpiece. It is disclosed that the temperature in this area the temperature of the one with $f = 1.5$ is higher than one with $f = 0.7$ (see Figure 3.14). Furthermore, the quantity of the mechanical dissipation can be measured by the equivalent plastic strain as shown in Figure 3.15. Because of the temperature difference, the evolutions of austenitic transformation for both simulations show different contours at the time $t = 7.6 \cdot 10^{-5}$ s on the chip top (see Figure 3.16). Moreover, Figure 3.17 shows the contours of the stress mode factor ξ which is described in Eq.(3.35) for indicating the stress modes. The colours red, blue and green represent the zones under tension, compression and shear, respectively.

Next, we plot some important variables like von-Mises stress, temperature, maximal plain strain and the phases (austenite and martensite) over the time for two representative elements, one over and another below the separation layer named element A (E-A) and element B (E-B1), see Figure 3.18 and 3.19. As shown in Figure 3.18.a) the plastic deformation of the selected element starts at time $2.5 \cdot 10^{-5}$ s. At the same time the temperature raises and the stress goes down. Once the start temperature of austenitization $A_{c1} = 504$ °C is reached ($t = 3.8 \cdot 10^{-5}$ s), the initial martensite begins to transform into austenite. At the time $t = 5.5 \cdot 10^{-5}$ s, due to the applied cooling condition the temperature starts to sink. In comparison with Figure 3.18.b), the one with smaller friction has lower maximal plain strain and lower temperature. However, the quantity of the formed austenite has almost no difference between E-A and E-B1.

In comparison to E-A (Figure 3.18), E-B1 (Figure 3.19) has generally lower plastic deformation and therefore lower temperature. Because of the short duration of heating, the austenite fractions of E-B1 (Figure 3.19) are much lower than that for E-A (Figure 3.18). Then we compare temperature and austenite fraction between the one with $f = 1.5$ (Figure 3.19.a) and $f = 0.7$ (Figure 3.19.b). For $f = 1.5$ both temperature and austenite are greater than that for $f = 0.7$. Due to rapid cooling all obtained austenite for both simulations with $f = 1.5$ and $f = 0.7$ retransforms back into martensite once the martensite start temperature M_s is reached, where he new martensite can be expressed as

$$z_M^n = z_A^{max} - z_A. \tag{3.95}$$

Therefore, the one with $f = 1.5$ obtains more new formed martensite than that with $f = 0.7$. Moreover, simulations with more different frictions are investigated. The obtained new martensite related to the frictions is given in Figure 3.20. As we can see, the lower the friction, the less the new formed martensite. Due to the fact that the new martensite dominates the white layer formation ([69]), reducing the friction coefficient is a way to minimize the white layer formation.

Influence of cutting speed

In order to study the influence of cutting speeds, simulations with different cutting speeds $v = 3.6$, 3.2, 3, 2.9, 2.7 and 2.5 m/s, and with identical friction coefficient $f = 1.5$ are investigated. The results of the von-Mises stress, temperature, austenite and new martensite are shown in Figure 3.21, 3.22, 3.23 and 3.24, respectively. In order to obtain the same cutting length for all simulations, the cutting times are fitted as $t = 7.6 \cdot 10^{-5}$ s for $v = 3.6$ m/s, $t = 8.55 \cdot 10^{-5}$ s for $v = 3.2$ m/s, $t = 9.12 \cdot 10^{-5}$ s for $v = 3$ m/s, $t = 9.43 \cdot 10^{-5}$ s for $v = 2.9$ m/s, $t = 10.13 \cdot 10^{-5}$ s for $v = 2.7$ m/s and $t = 10.94 \cdot 10^{-5}$ s for $v = 2.5$ m/s. As we can see, all simulations obtain the same chip form. This means that the cutting speed has no influence on the chip formation. Furthermore, the von-Mises stress (Figure 3.21) with higher cutting speed is higher than that with lower cutting speed, especially in the cutting zone (see Figure 3.21). The temperature has the same tendency (see Figure 3.22). Due to the different duration of the simulations, the austenite fraction shows difference too (Figure 3.23). The one with longer duration (lower speed) obtains

more austenite than the one with shorter duration (higher speed). However, the new martensite shows the opposite tendency (Figure 3.24). The higher the cutting speed, the more the new martensite.

Using the same comparisons we have done for studying influence of the friction, we also plot the important variables e.g. von-Mises stress, temperature, maximal plain strain and the phases over the time for the elements above (E-A) and below the separation layer (E-B1 and E-B2) (see Figure 3.25, 3.26 and 3.27). We compare Figure 3.25.a with 3.25.b, and can find that the equivalent plastic strain has almost no difference. The temperature for lower cutting speed is lower, the von-Mises stress and austenite fraction for lower cutting speed are higher. The comparison results pass to the above contour comparisons in Figure 3.21 to 3.23. Furthermore, two elements (E-B1 and E-B2) of different depths below the separation layer are analysed. As shown in Figure 3.26 for E-B1 all variables show almost no difference due to different cutting speeds. For the deeper element E-B2 (Figure 3.27) the differences on the phase fractions are clear. Due to the lower temperature at lower cutting speed, the austenitic transformation dosen't occur, thus no new martensite is formed. In summary, besides the friction the cutting speed plays an important role for the white layer formation. The lower the cutting speed, the less the white layer.

Influence of the TRIP-strains

In order to study the influence of the TRIP-strains, the reference simulation with $f = 1.5$ and $v = 3.6$ m/s are performed, where the TRIP-strain is activated and deactivated. The contours of austenite, von-Mises stress and temperature at time $t = 7.6 \cdot 10^{-5}$ s for both simulations are shown in Figure 3.28. In comparison, there is no difference on the contours of the austenite and the temperature between both simulations (Figure 3.28 a und c). Some differences of the von-Mises stress are marked on the cutting chip as well as in the cutting zone in Figure 3.28 b. Next, the important variables for the two elements are also plotted as above. As shown in Figure 3.29 the equivalent plastic strain, the temperature and the austenite fraction have no difference between the two cases for the element on the cutting chip. However, we can find some differences on the von-Mises stress curve during the austenitization starting at $t = 3.8 \cdot 10^{-5}$ s. The same occurs on the element below the separation layer (see Figure 3.30). There is still no difference for the equivalent plastic strain, the temperature and the phases. But some differences can be found on the contour of the von-Mises stress when phase changes occur.

Next, we define a scalar TRIP-factor

$$
w_A = 3G \begin{cases} f'[z_A]\Delta z_A K_{tpA} & \text{for } \dot{z}_A \geq 0 \\[2mm] f'[z_M]\Delta z_M K_{tpM} & \text{for } \dot{z}_A < 0 \end{cases} \tag{3.96}
$$

from Eq. (3.75.4) in order to represent the quantity of TRIP-strains. As shown in Figure 3.31 the value of w_A is very small at the area where the austenitization occurs and shows a stress dependency due to the stress-dependent parameters K_{tpA} and K_{tpM}. In summary, TRIP-strains only affect the von-Mises stress and whose influence is very small.

$f = 1.5$, $v = 3.6$m/s
(Reference solution)

$f = 0.7$, $v = 3.6$m/s

$t = 1.14 \cdot 10^{-6}$ s

$t = 1.14 \cdot 10^{-6}$ s

$t = 2.584$E-5

$t = 2.584 \cdot 10^{-5}$ s

$t = 5.054 \cdot 10^{-5}$ s

$t = 5.054 \cdot 10^{-5}$ s

$t = 7.6 \cdot 10^{-5}$ s

$t = 7.6 \cdot 10^{-5}$ s
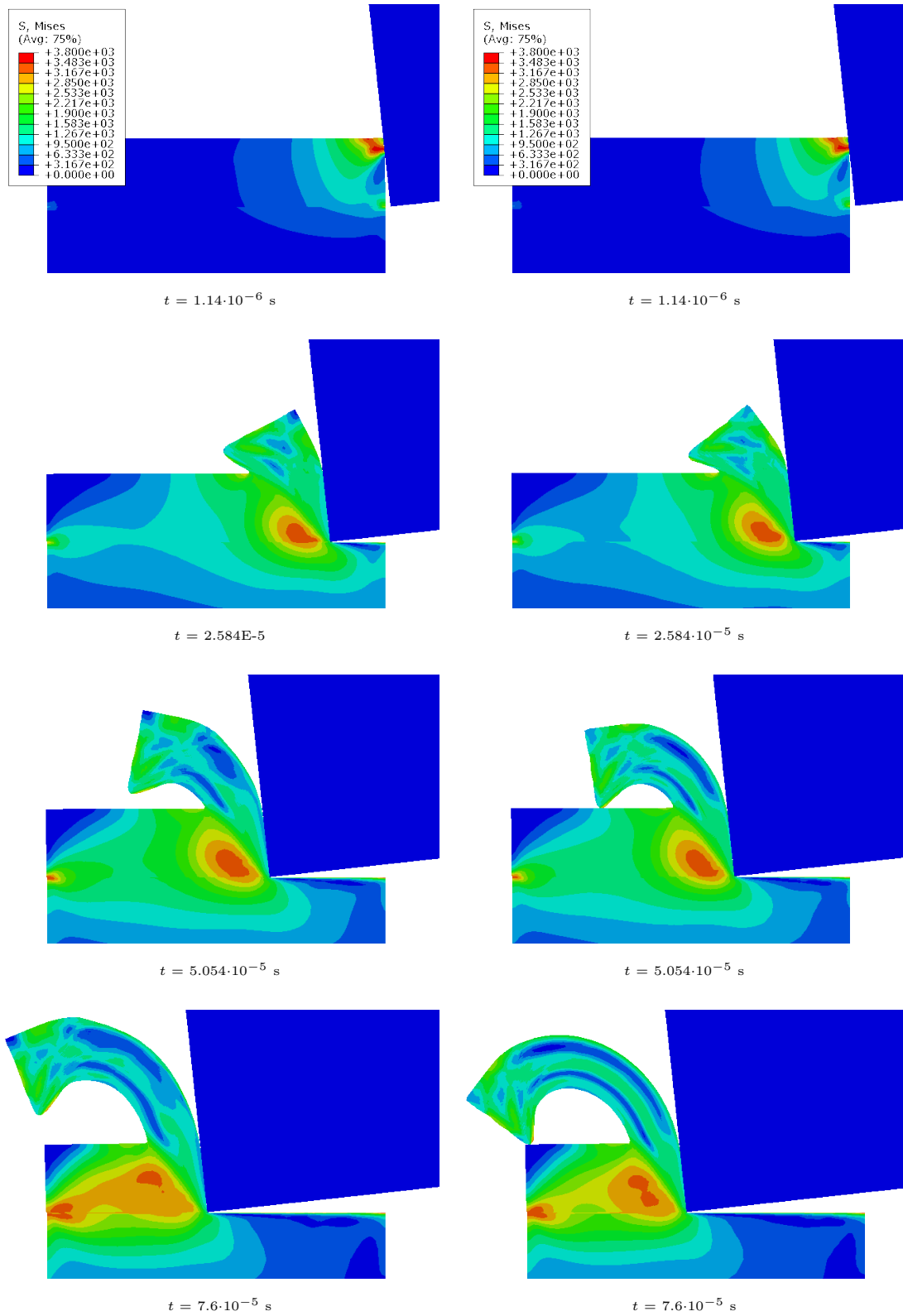
Figure 3.13: Cutting simulation: Contours of von-Mises stress for different friction coefficients $f = 1.5$ (left) and $f = 0.7$ (right)

54

$f = 1.5$, $v = 3.6$m/s
(Reference solution)

$f = 0.7$, $v = 3.6$m/s

$t = 1.14 \cdot 10^{-6}$ s

$t = 1.14 \cdot 10^{-6}$ s

$t = 2.584 \cdot 10^{-5}$ s

$t = 2.584 \cdot 10^{-5}$ s

$t = 5.054 \cdot 10^{-5}$ s

$t = 5.054 \cdot 10^{-5}$ s

$t = 7.6 \cdot 10^{-5}$ s

$t = 7.6 \cdot 10^{-5}$ s
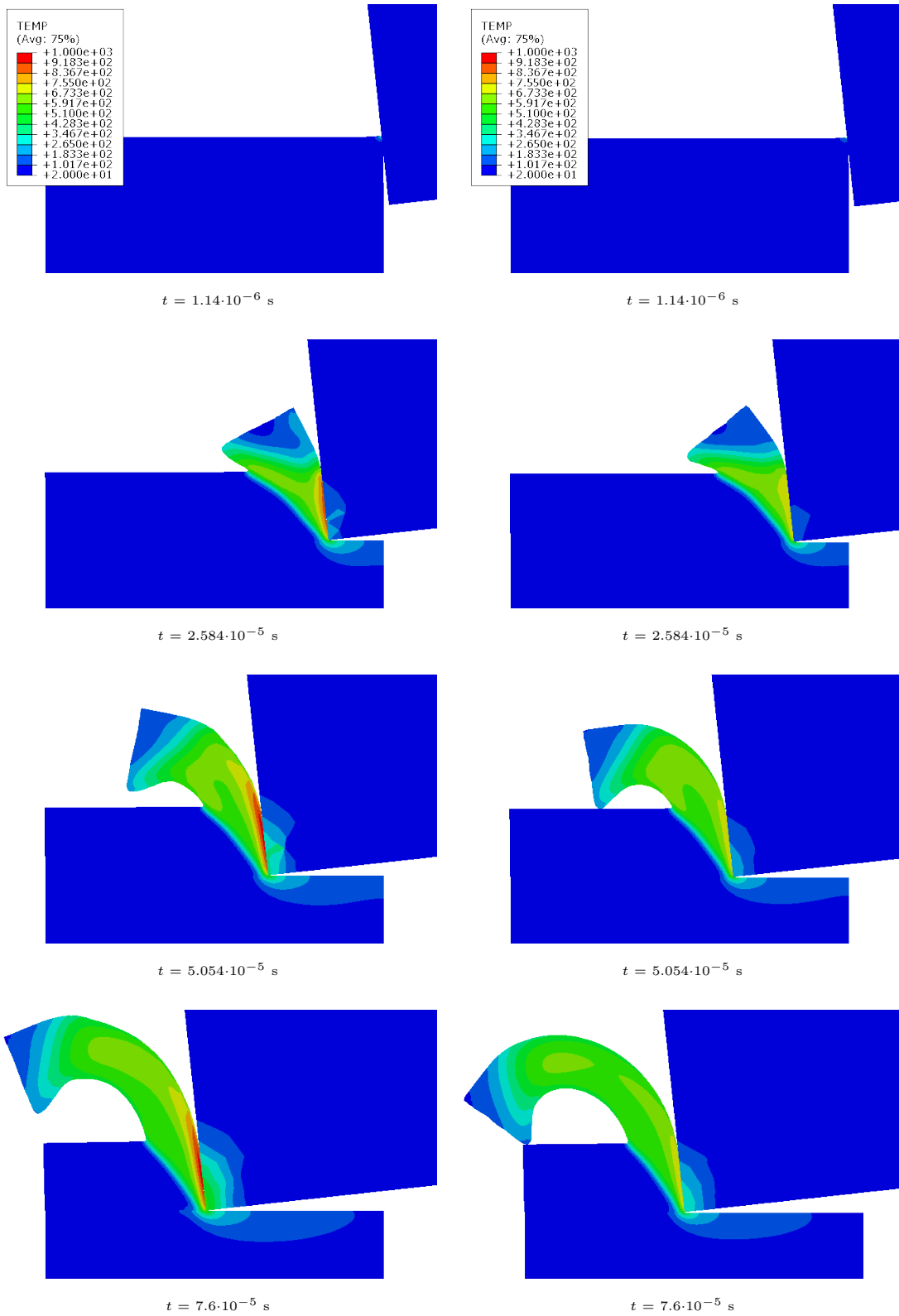
Figure 3.14: Cutting simulation: Contours of temperature for different friction coefficients $f = 1.5$ (left) and $f = 0.7$ (right)

$f = 1.5$, $v = 3.6$m/s
(Reference solution)

$f = 0.7$, $v = 3.6$m/s

$t = 1.14 \cdot 10^{-6}$ s

$t = 1.14 \cdot 10^{-6}$ s

$t = 2.584 \cdot 10^{-5}$ s

$t = 2.584 \cdot 10^{-5}$ s

$t = 5.054 \cdot 10^{-5}$ s

$t = 5.054 \cdot 10^{-5}$ s

$t = 7.6 \cdot 10^{-5}$ s

$t = 7.6 \cdot 10^{-5}$ s
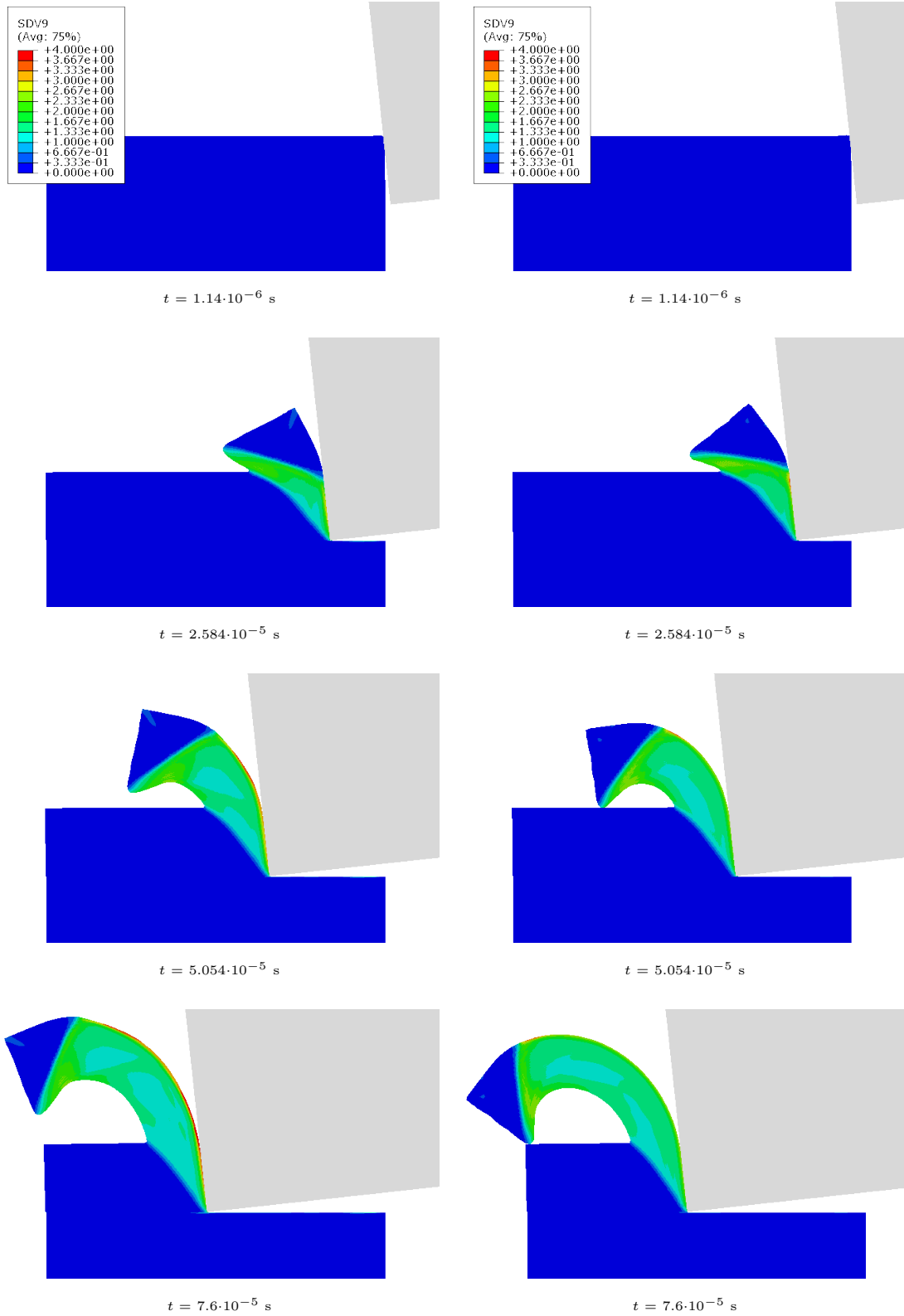
Figure 3.15: Cutting simulation: Contours of equivalent plastic strain for different friction coefficients $f = 1.5$ (left) and $f = 0.7$ (right)

56

$f = 1.5$, $v = 3.6$m/s
(Reference solution)

$f = 0.7$, $v = 3.6$m/s

$t = 1.14 \cdot 10^{-6}$ s

$t = 1.14 \cdot 10^{-6}$ s

$t = 2.584 \cdot 10^{-5}$ s

$t = 2.584 \cdot 10^{-5}$ s

$t = 5.054 \cdot 10^{-5}$ s

$t = 5.054 \cdot 10^{-5}$ s

$t = 7.6 \cdot 10^{-5}$ s

$t = 7.6 \cdot 10^{-5}$ s
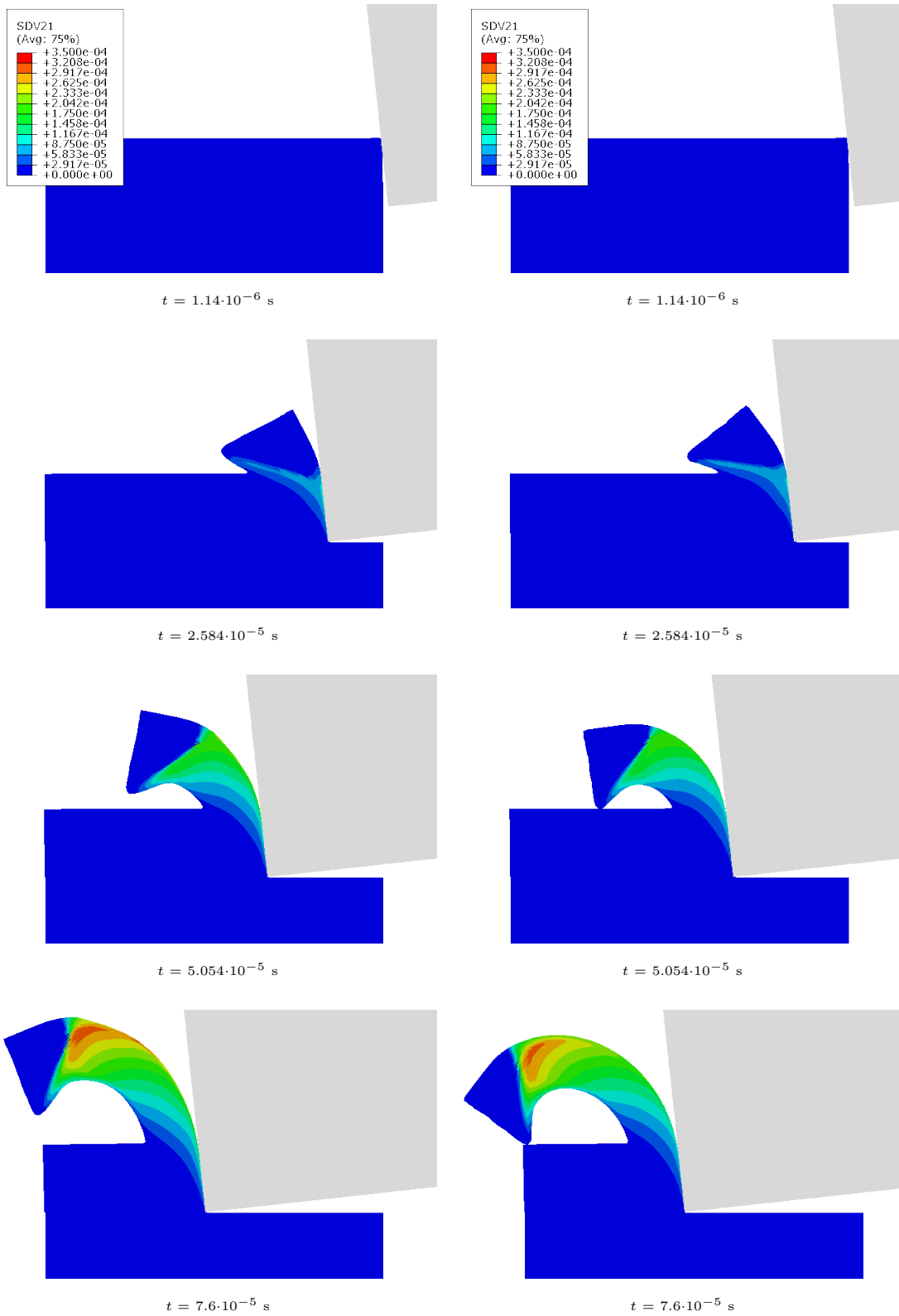
Figure 3.16: Cutting simulation: Contours of austenite z_A for different friction coefficients $f = 1.5$ (left) and $f = 0.7$ (right)

$f = 1.5$, $v = 3.6$m/s
(Reference solution)

$f = 0.7$, $v = 3.6$m/s

$t = 1.14 \cdot 10^{-6}$ s

$t = 1.14 \cdot 10^{-6}$ s

$t = 2.584 \cdot 10^{-5}$ s

$t = 2.584 \cdot 10^{-5}$ s

$t = 5.054 \cdot 10^{-5}$ s

$t = 5.054 \cdot 10^{-5}$ s

$t = 7.6 \cdot 10^{-5}$ s

$t = 7.6 \cdot 10^{-5}$ s
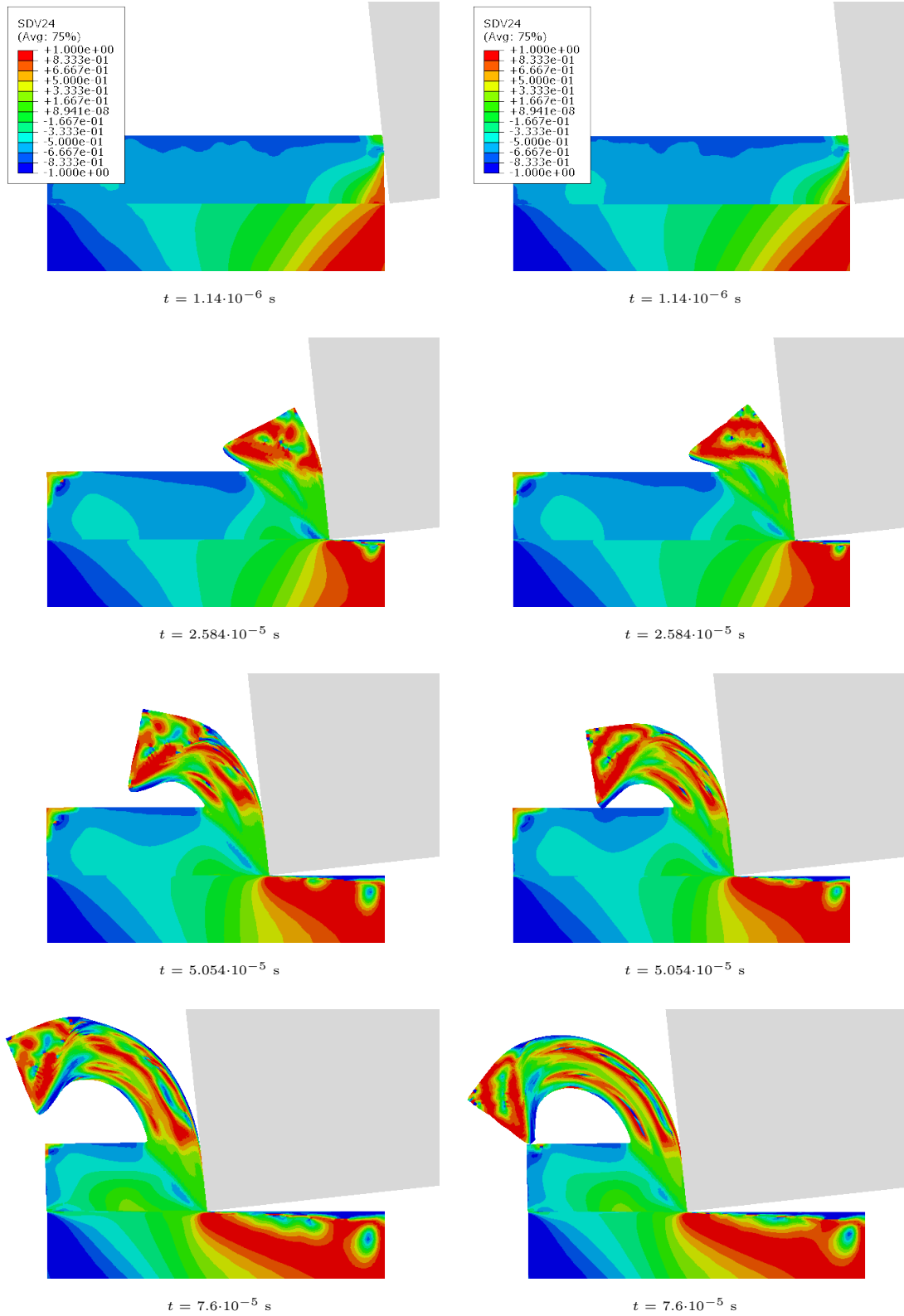
Figure 3.17: Cutting simulation: Contours of stress mode factor ξ for different friction coefficients $f = 1.5$ (left) and $f = 0.7$ (right)

58
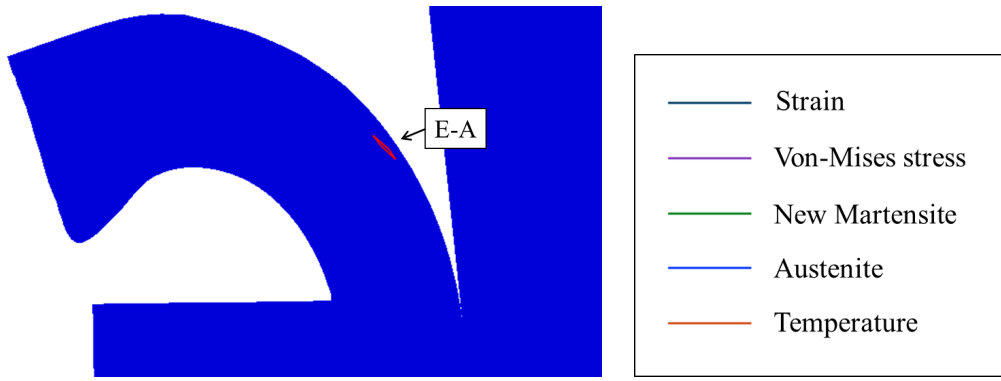
a) $f = 1.5$, $v = 3.6$ m/s
(Reference solution)
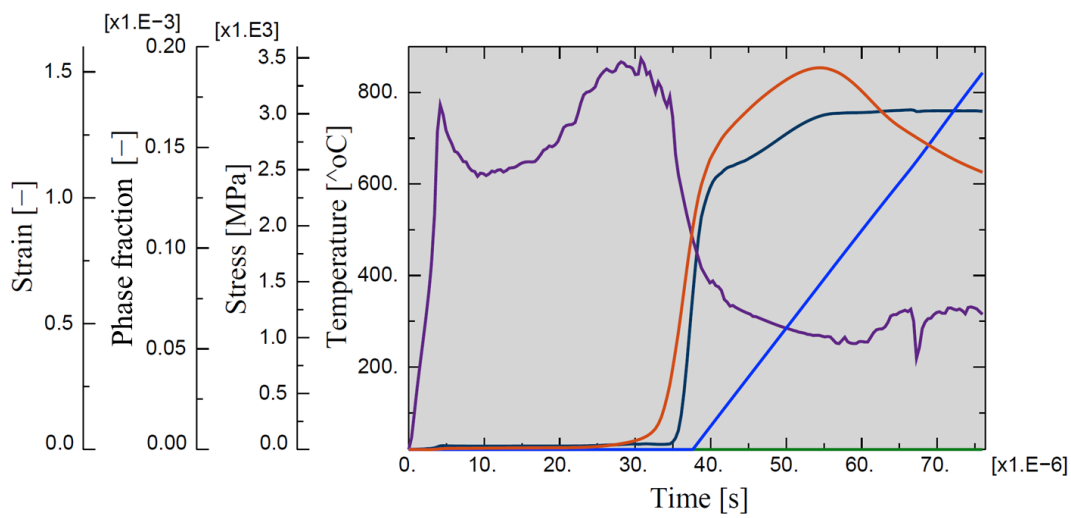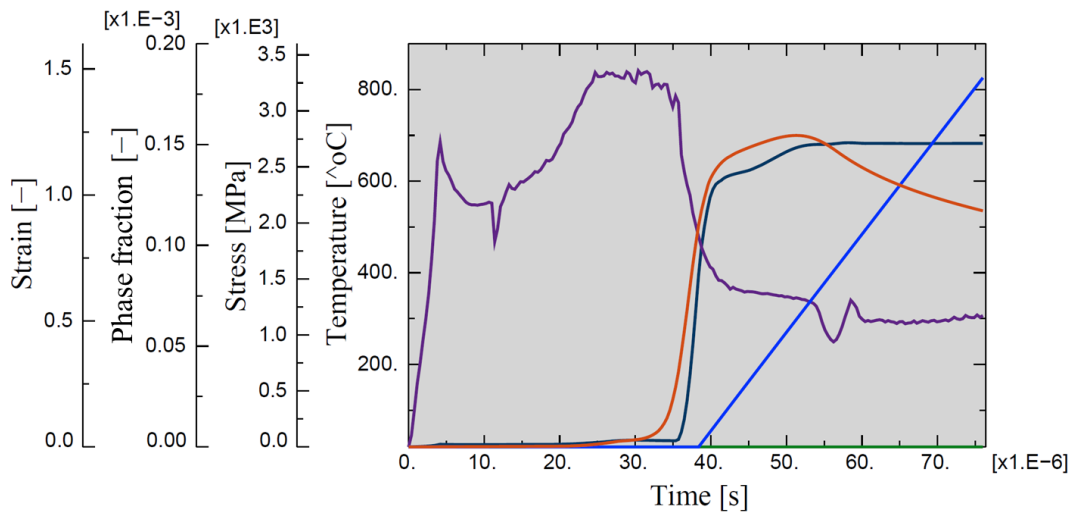
b) $f = 0.7$, $v = 3.6$ m/s

Figure 3.18: Cutting simulation: Variables of the plotted element E-A
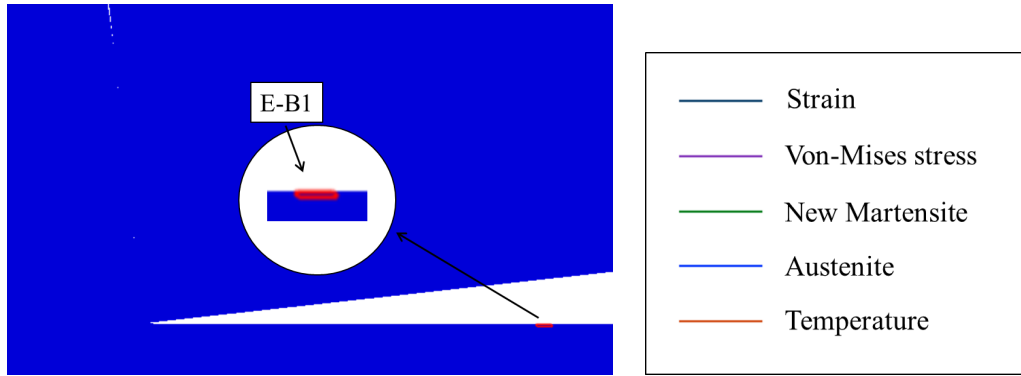
a) $f = 1.5$, $v = 3.6$ m/s
(Reference solution)
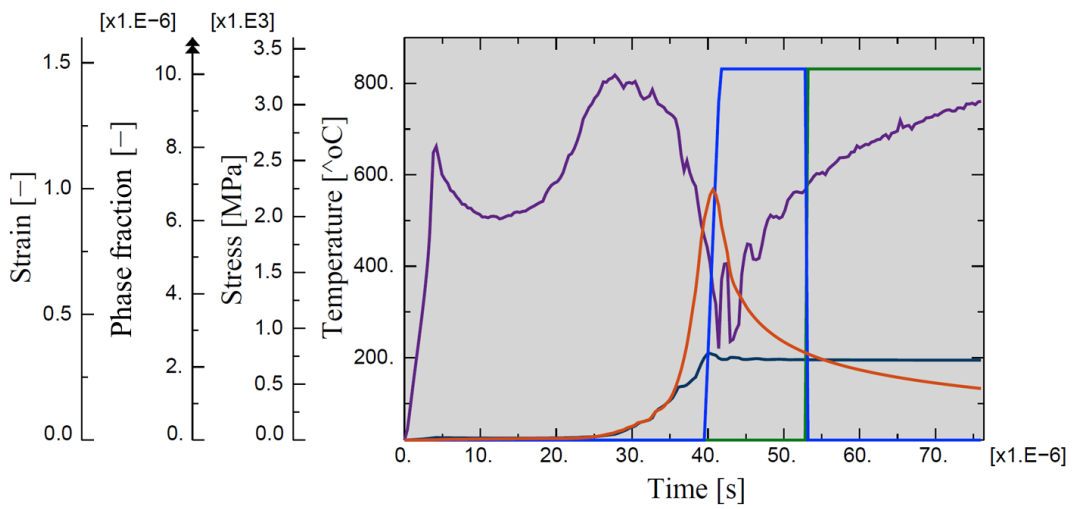
b) $f = 0.7$, $v = 3.6$ m/s
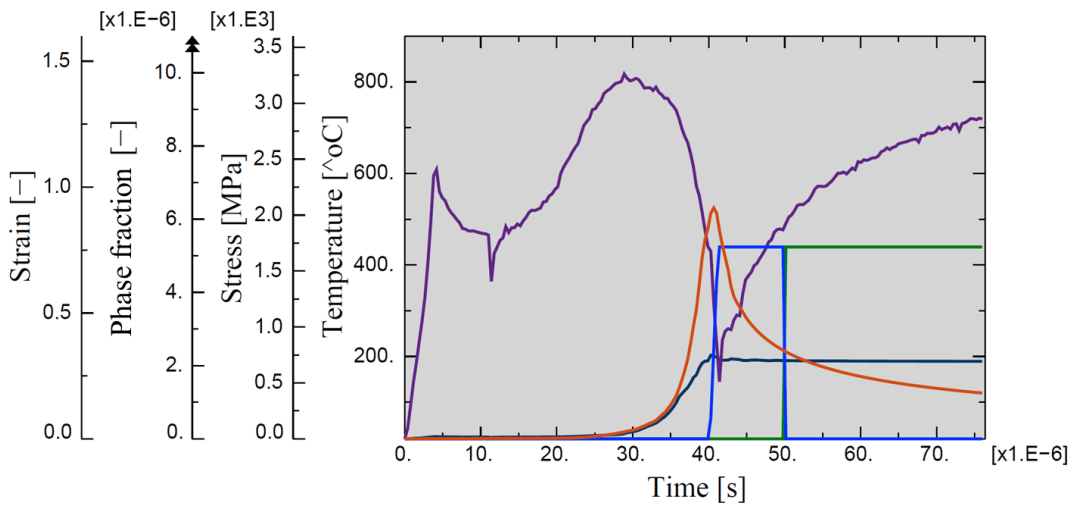
Figure 3.19: Cutting simulation: Variables of the plotted element E-B1
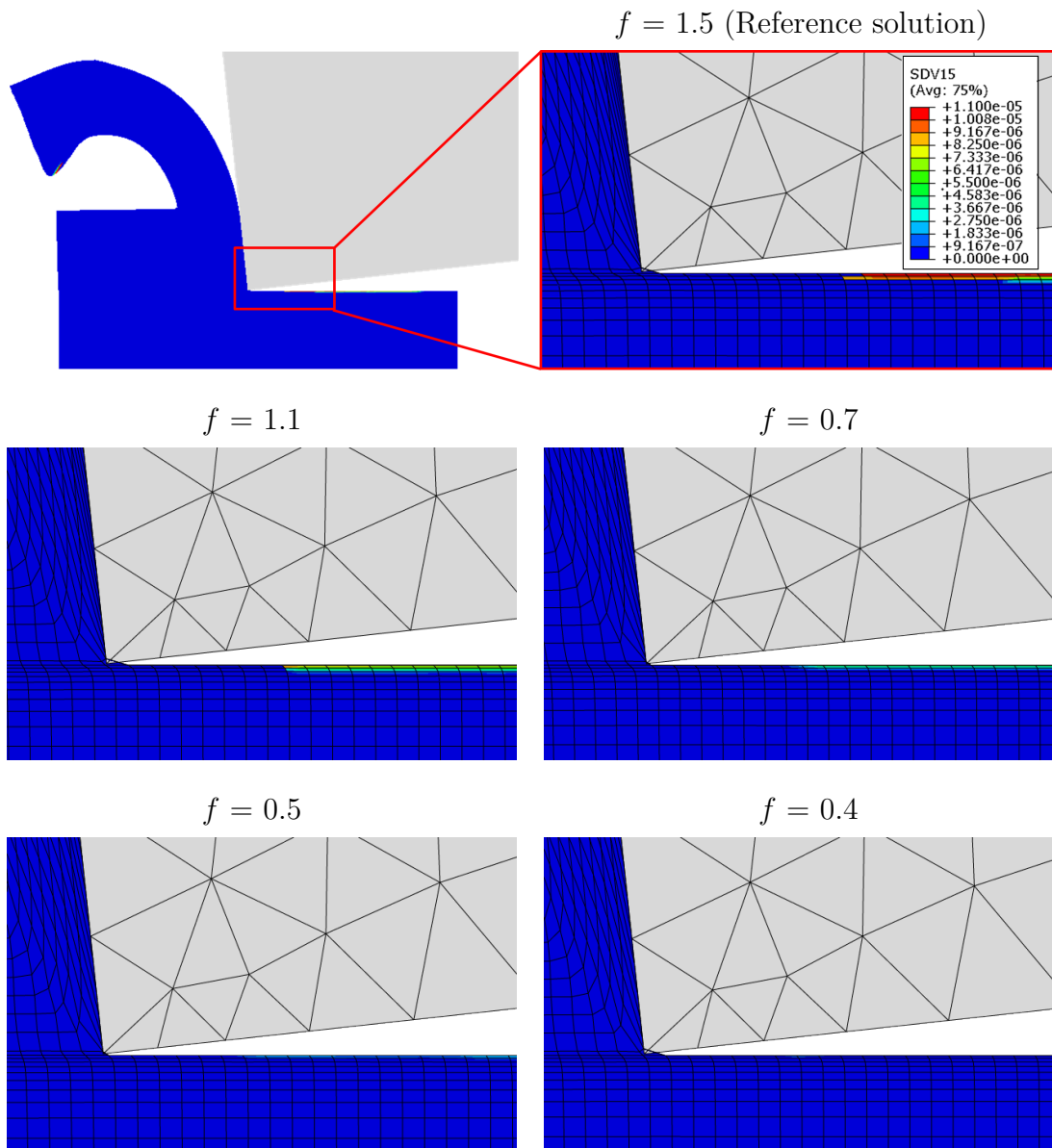
Figure 3.20: Cutting simulation: Contours of new martensite z_M^n for different friction coefficients ($v = 3.6$ m/s, $t = 7.6 \cdot 10^{-6}$ s)

$v = 3.6$ m/s
(Reference solution)
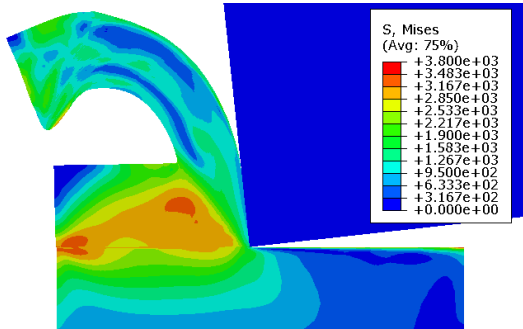
$v = 3.2$ m/s

$t = 7.6 \cdot 10^{-5}$ s
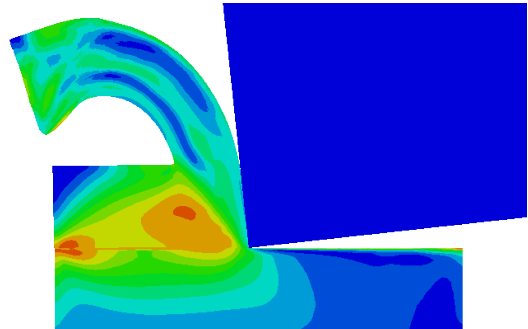
$t = 8.55 \cdot 10^{-5}$ s

$v = 3$ m/s
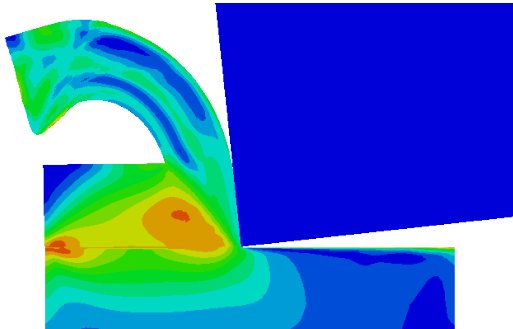
$v = 2.9$ m/s

$t = 9.12 \cdot 10^{-5}$ s
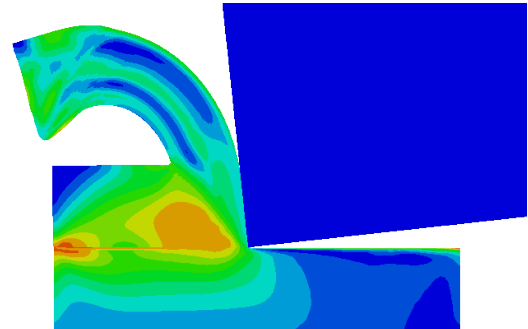
$t = 9.43 \cdot 10^{-5}$ s

$v = 2.7$ m/s
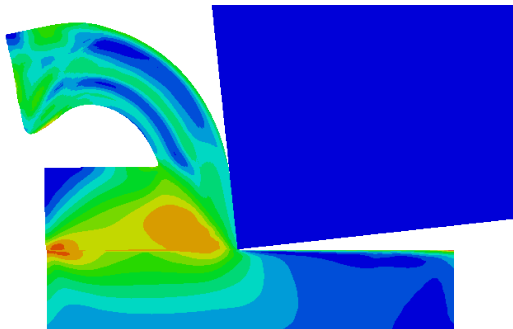
$v = 2.5$ m/s

$t = 10.13 \cdot 10^{-5}$ s
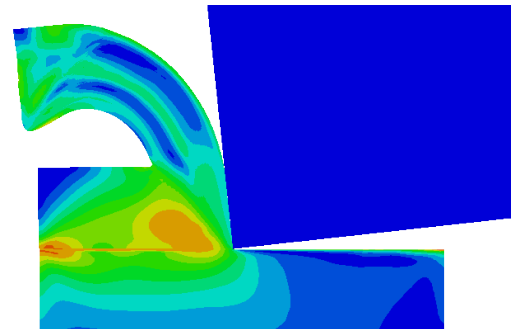
$t = 10.94 \cdot 10^{-5}$ s

Figure 3.21: Cutting simulation: Contours of von-Mises stress for different cutting speeds ($f = 1.5$)

$v = 3.6$ m/s
(Reference solution)

$t = 7.6 \cdot 10^{-5}$ s

$v = 3.2$ m/s

$t = 8.55 \cdot 10^{-5}$ s

$v = 3$ m/s

$t = 9.12 \cdot 10^{-5}$ s

$v = 2.9$ m/s

$t = 9.43 \cdot 10^{-5}$ s

$v = 2.7$ m/s

$t = 10.13 \cdot 10^{-5}$ s

$v = 2.5$ m/s

$t = 10.94 \cdot 10^{-5}$ s
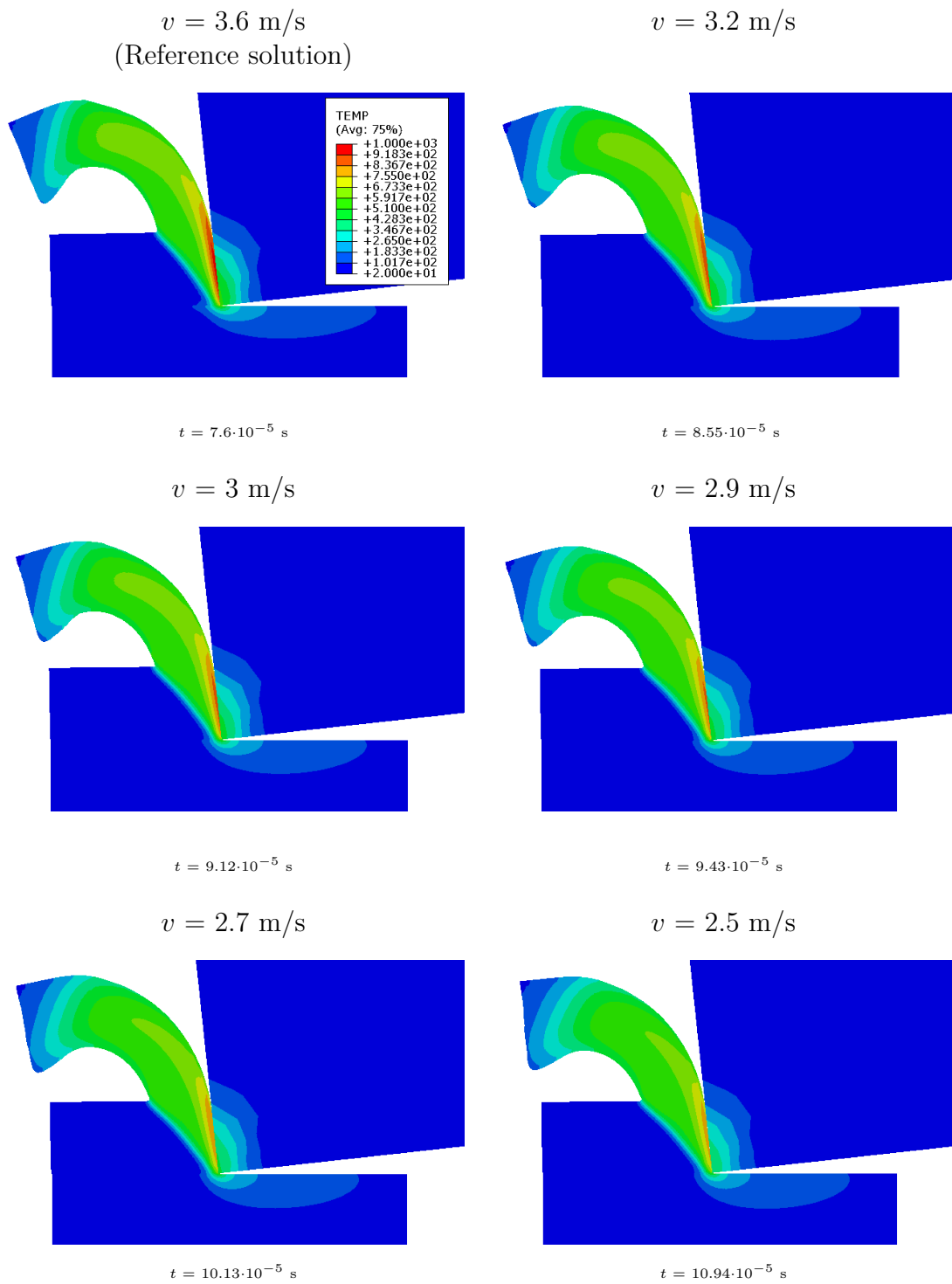
Figure 3.22: Cutting simulation: Contours of temperature for different cutting speeds ($f = 1.5$)

$v = 3.6$ m/s
(Reference solution)

$v = 3.2$ m/s

$t = 7.6 \cdot 10^{-5}$ s

$t = 8.55 \cdot 10^{-5}$ s

$v = 3$ m/s

$v = 2.9$ m/s

$t = 9.12 \cdot 10^{-5}$ s

$t = 9.43 \cdot 10^{-5}$ s

$v = 2.7$ m/s

$v = 2.5$ m/s

$t = 10.13 \cdot 10^{-5}$ s

$t = 10.94 \cdot 10^{-5}$ s
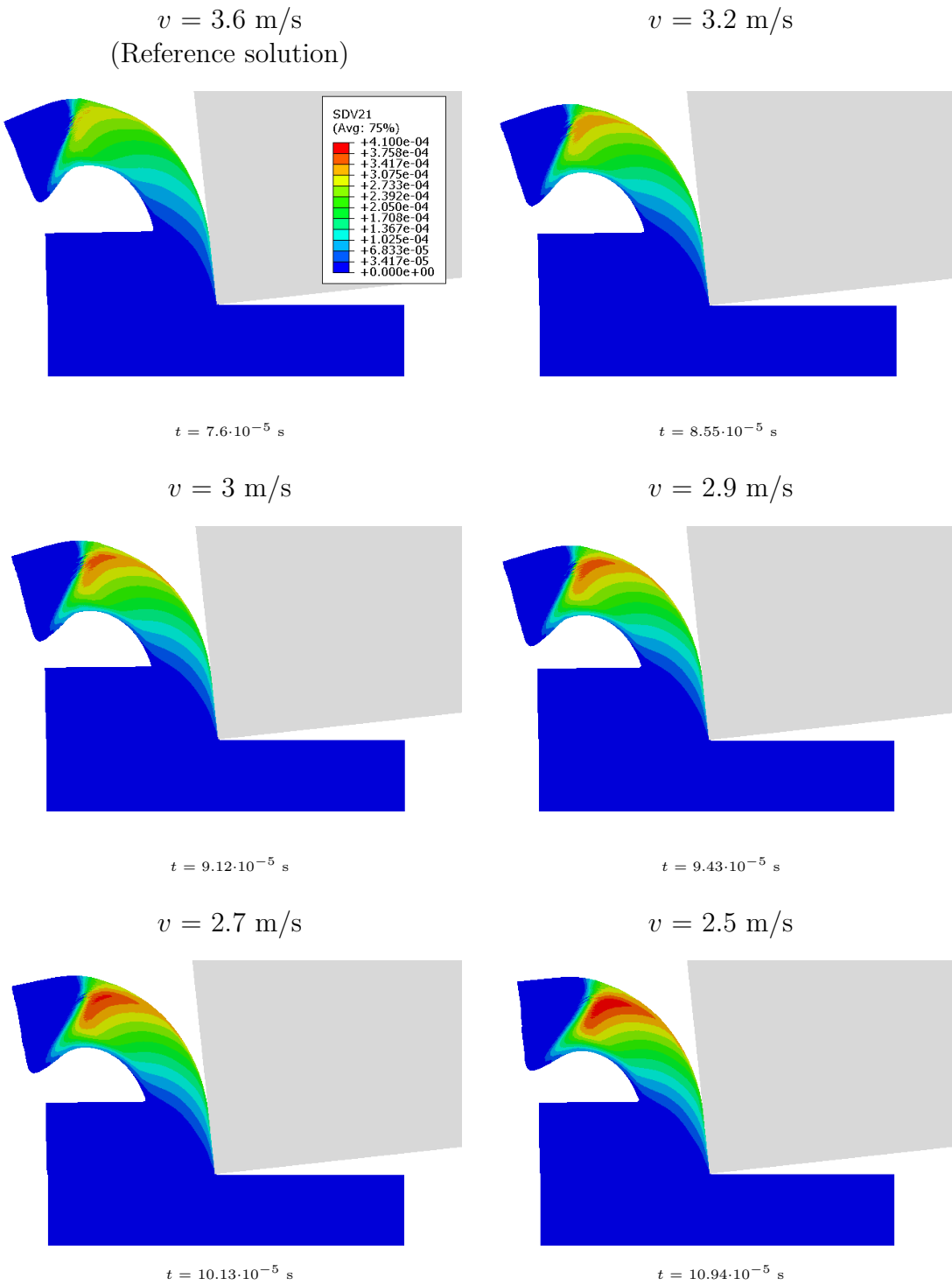
Figure 3.23: Cutting simulation: Contours of austenite z_A for different cutting speeds ($f = 1.5$)

$v = 3.6$ m/s
(Reference solution)

$t = 7.6 \cdot 10^{-5}$ s

$v = 3.2$ m/s

$t = 8.55 \cdot 10^{-5}$ s

$v = 3$ m/s

$t = 9.12 \cdot 10^{-5}$ s

$v = 2.9$ m/s

$t = 9.43 \cdot 10^{-5}$ s

$v = 2.7$ m/s

$t = 10.13 \cdot 10^{-5}$ s

$v = 2.5$ m/s

$t = 10.94 \cdot 10^{-5}$ s
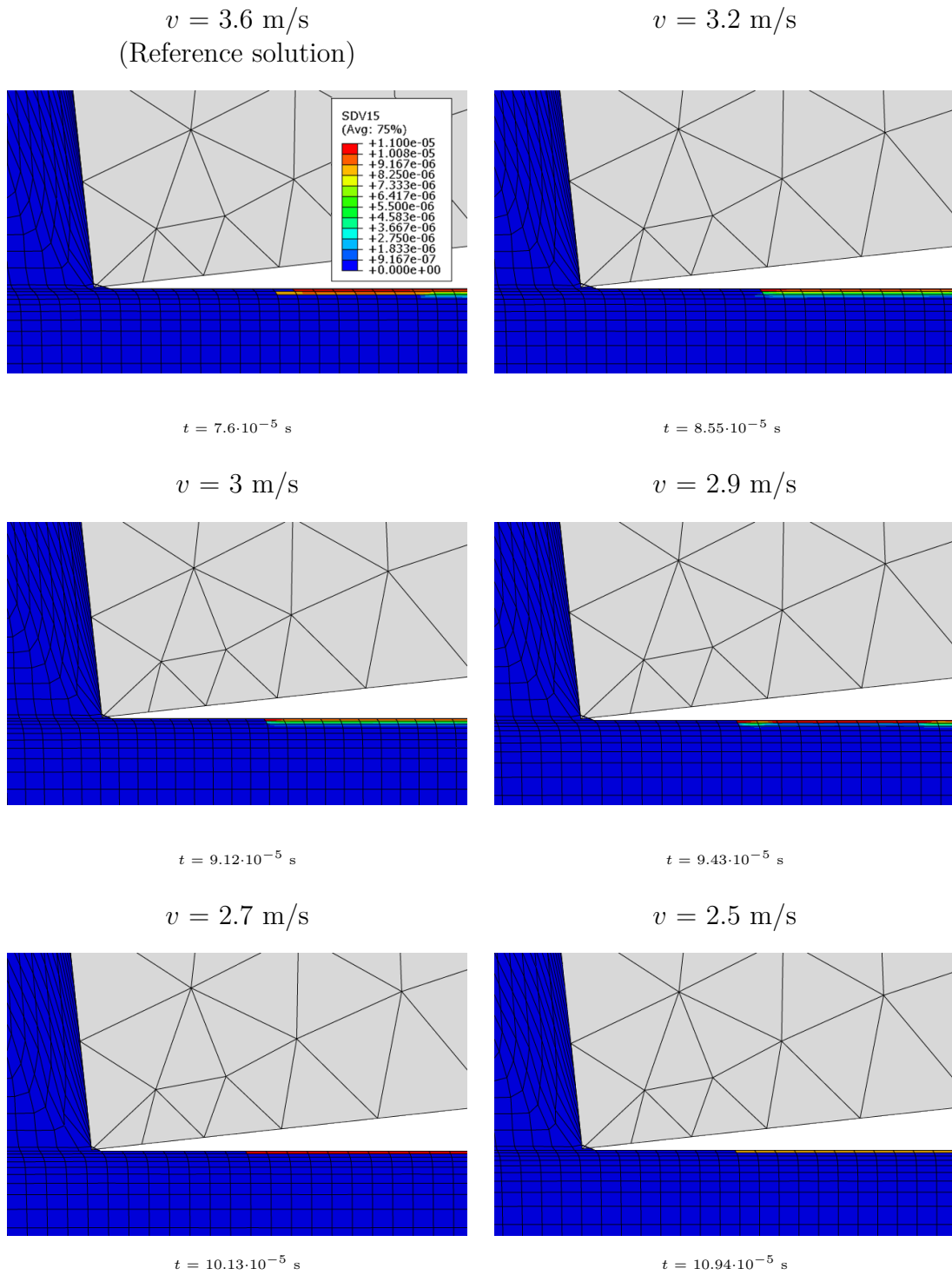
Figure 3.24: Cutting simulation: Contours of new martensite z_M^n for different cutting speeds ($f = 1.5$)
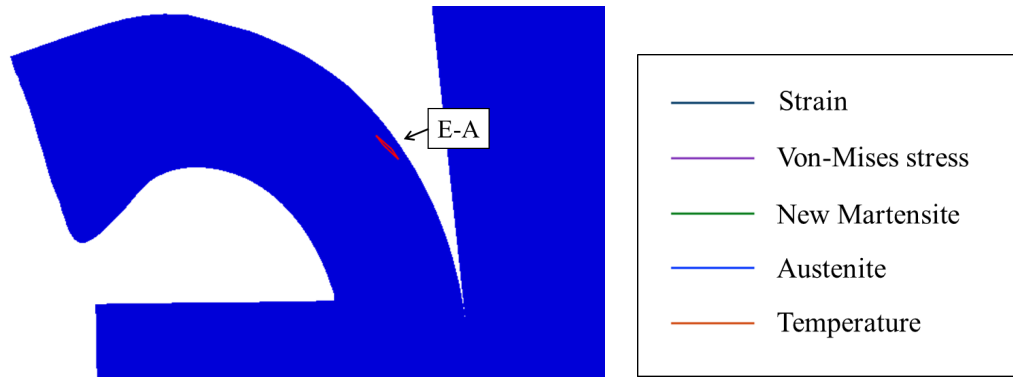
a) $f = 1.5$, $v = 3.2$ m/s
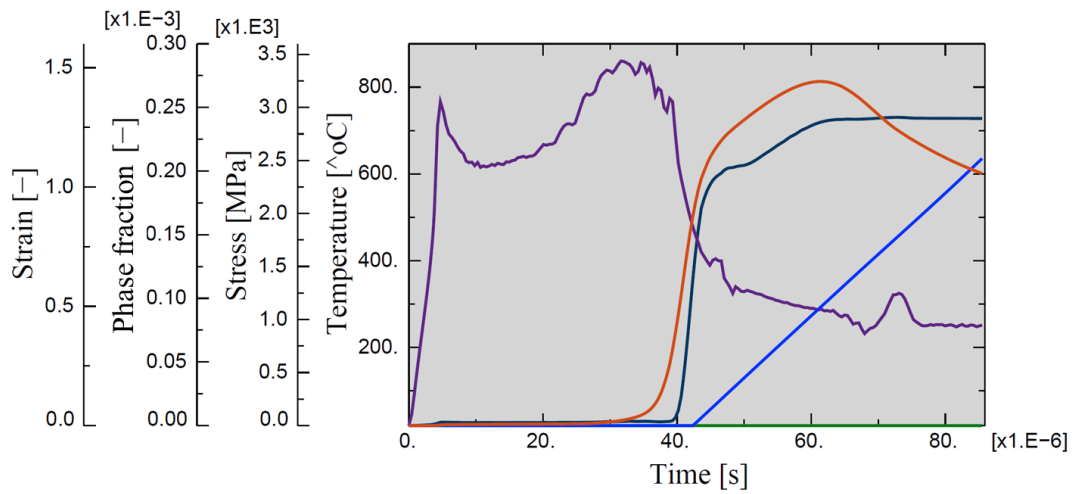
b) $f = 1.5$, $v = 2.5$ m/s
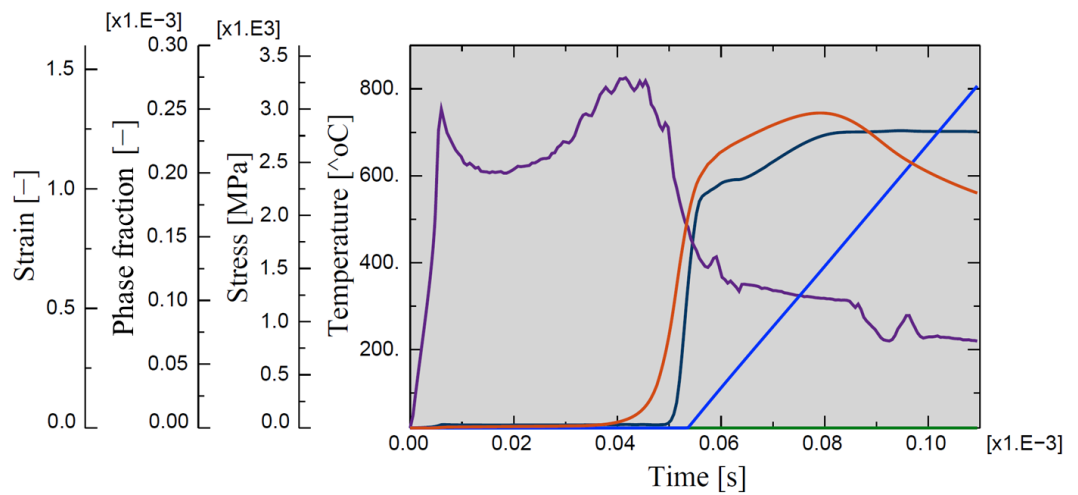
Figure 3.25: Cutting simulation: Variables of the plotted element for different cutting speeds E-A
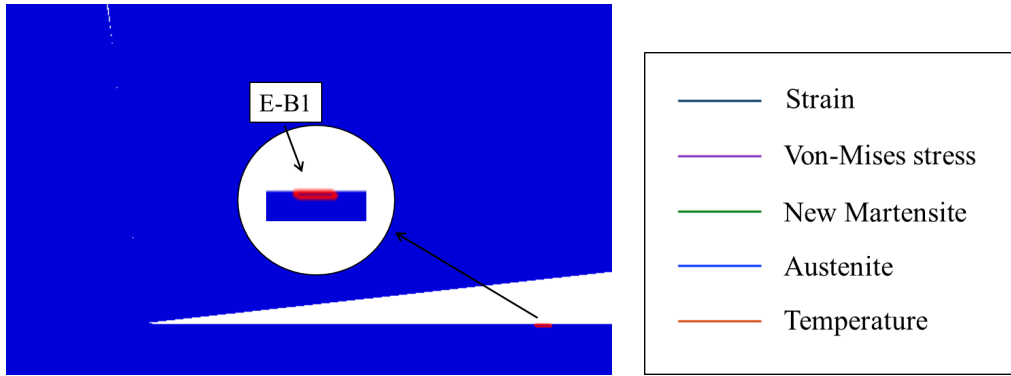
a) $f = 1.5$, $v = 3.2$ m/s
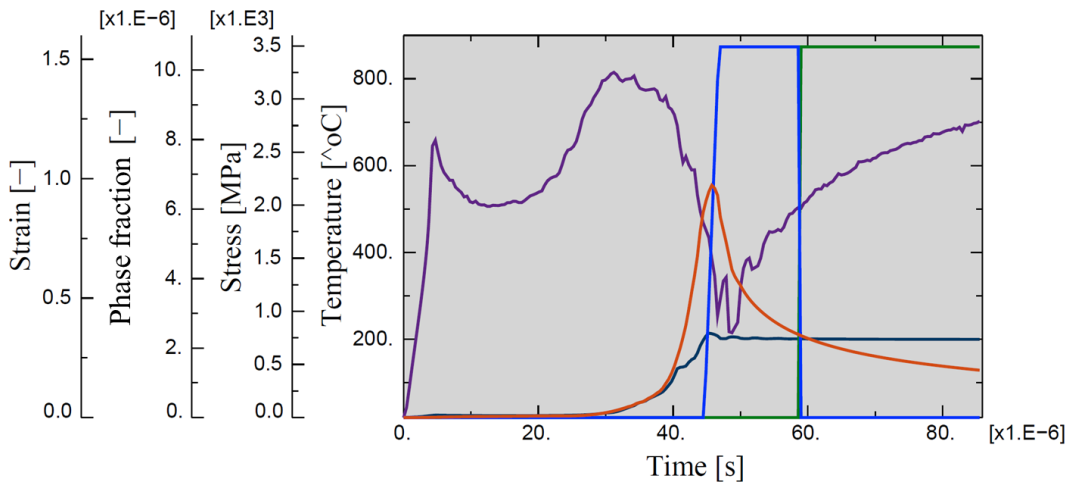
b) $f = 1.5$, $v = 2.5$ m/s
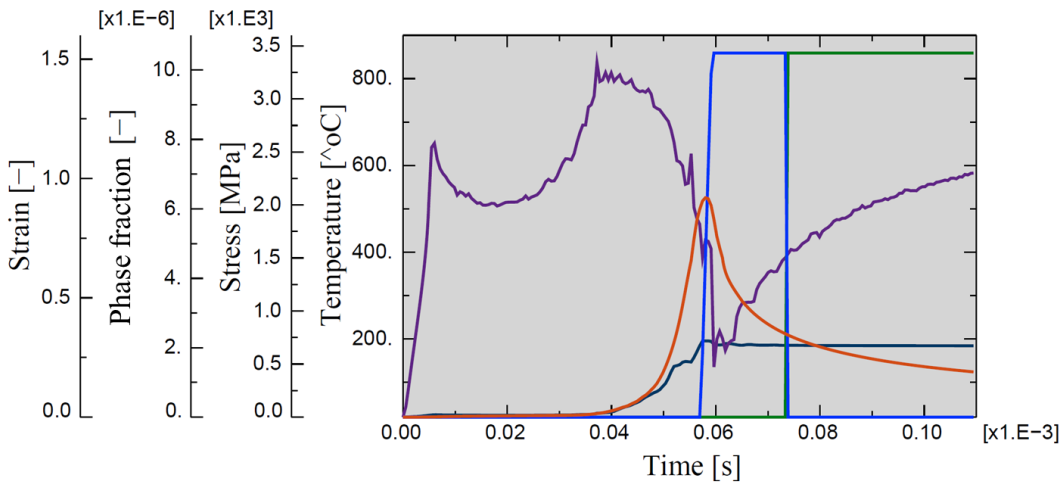
Figure 3.26: Cutting simulation: Variables of the plotted element for different cutting speeds E-B1
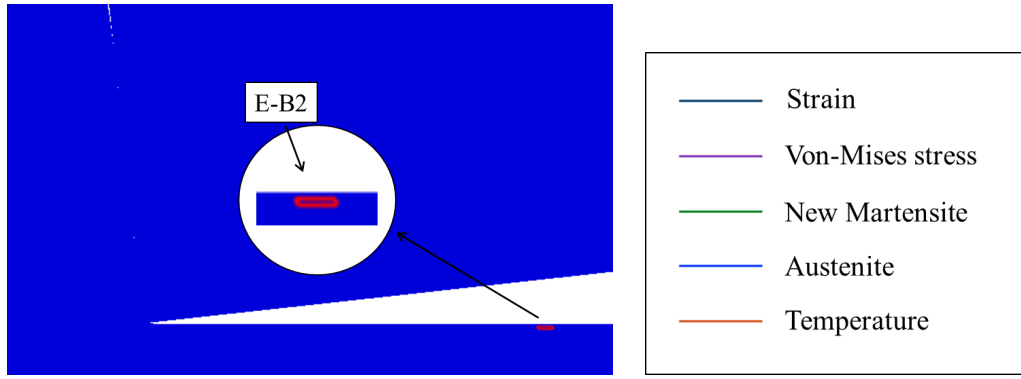
a) $f = 1.5$, $v = 3.2$ m/s
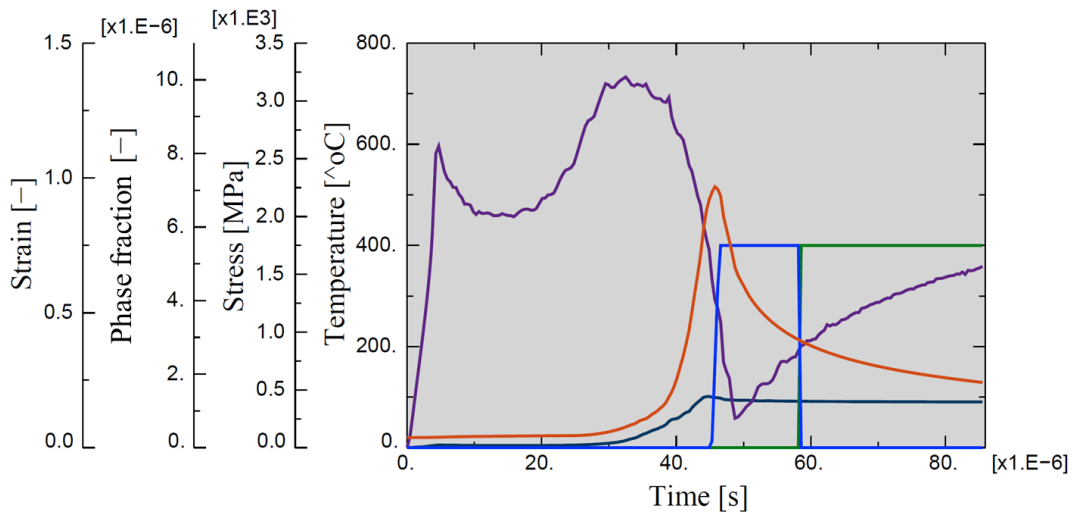
b) $f = 1.5$, $v = 2.5$ m/s
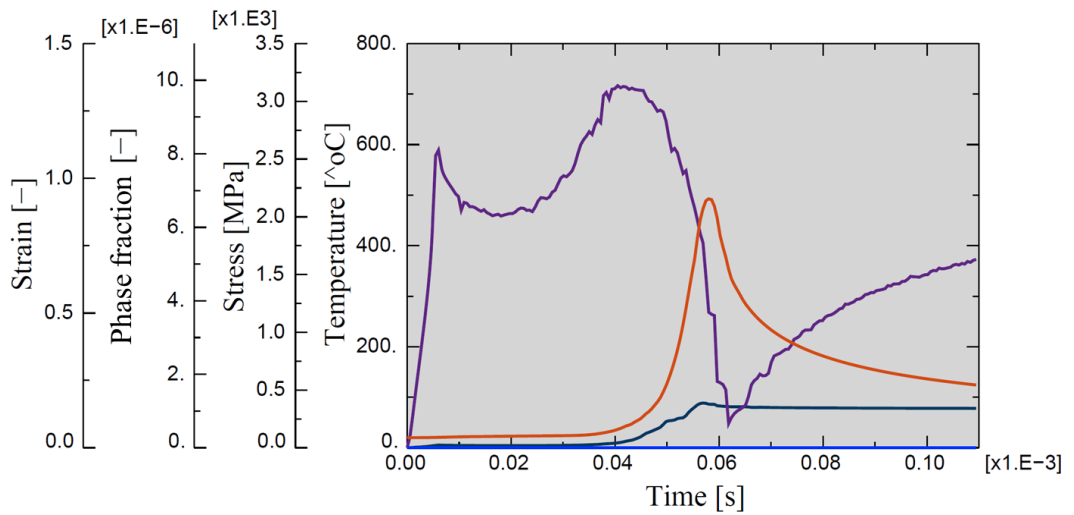
Figure 3.27: Cutting simulation: Variables of the plotted element for different cutting speeds E-B2

TRIP-strain activated   TRIP-strains deactivated

a)

$t = 7.6 \cdot 10^{-5}$ s $t = 7.6 \cdot 10^{-5}$ s

b)

$t = 7.6 \cdot 10^{-5}$ s $t = 7.6 \cdot 10^{-5}$ s

c)

$t = 7.6 \cdot 10^{-5}$ s $t = 7.6 \cdot 10^{-5}$ s
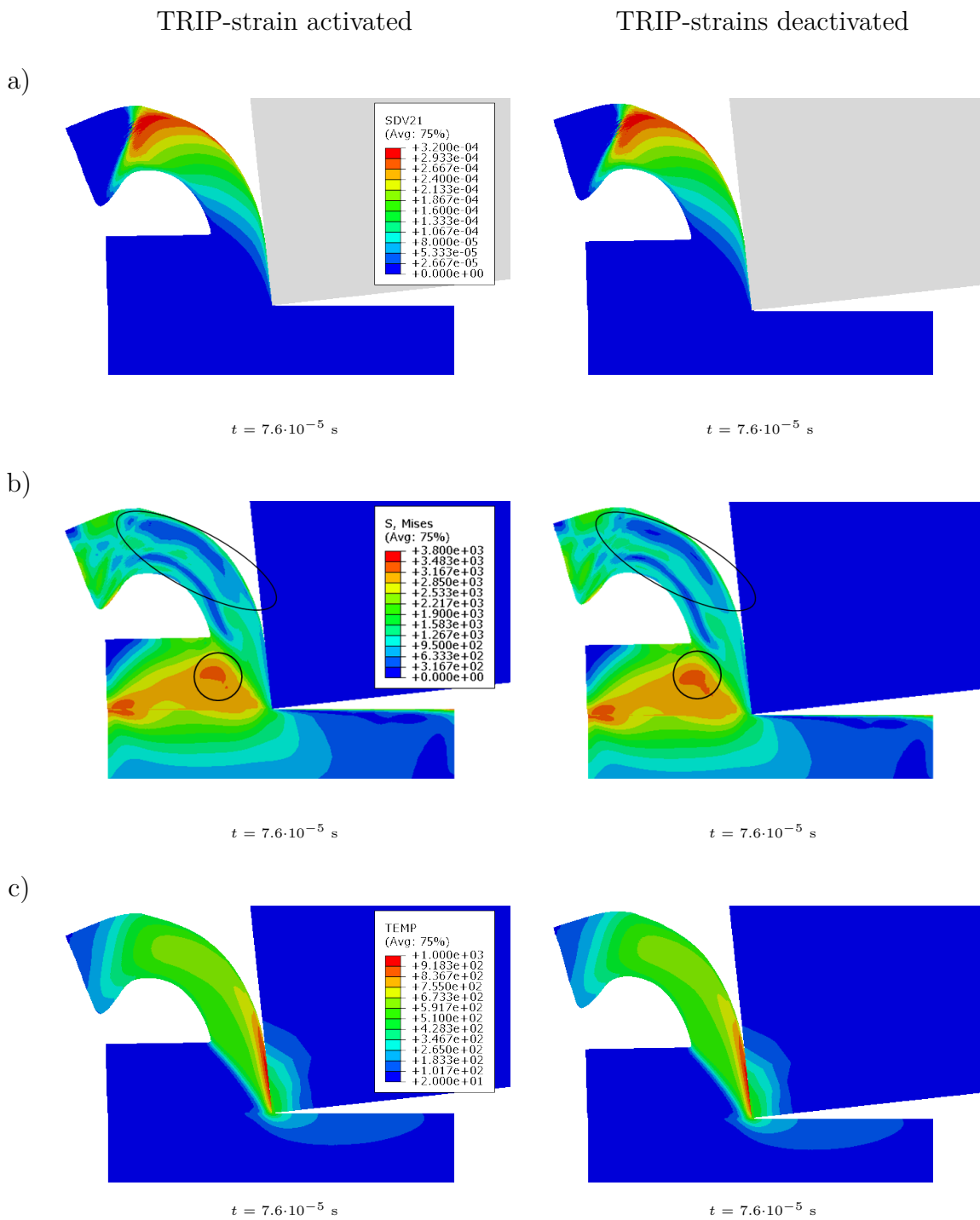
Figure 3.28: Cutting simulation: Contours of a) austenite, b) von-Mises stress, c) temperature for the influence of the TRIP-strain
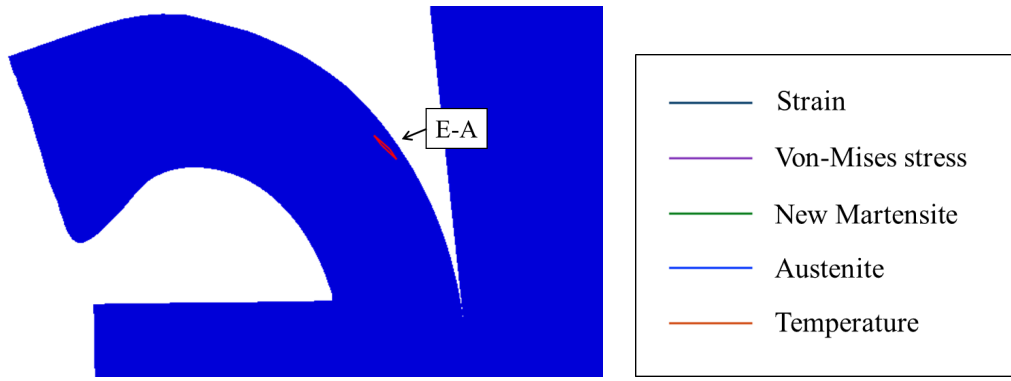
a) TRIP-strains activated
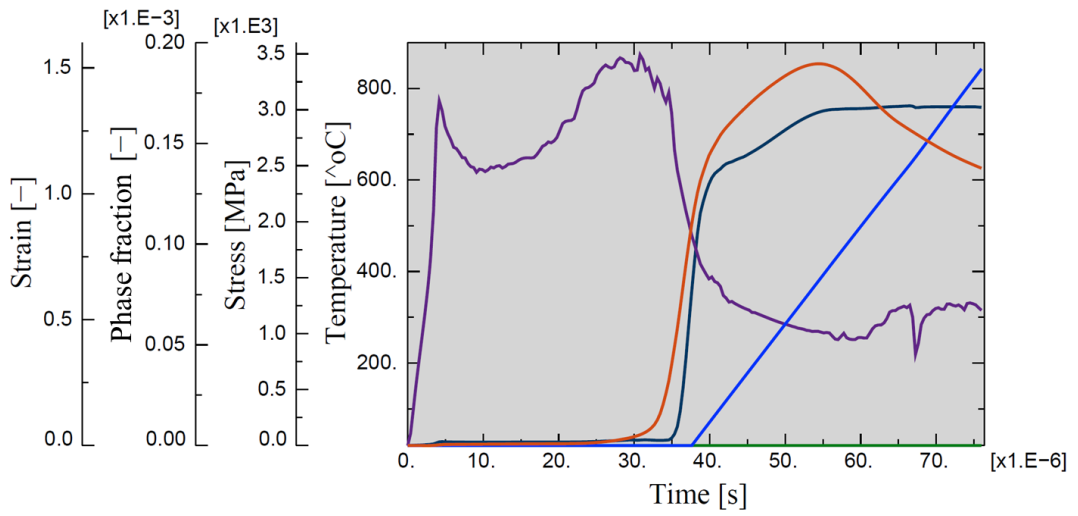
b) TRIP-strains deactivated
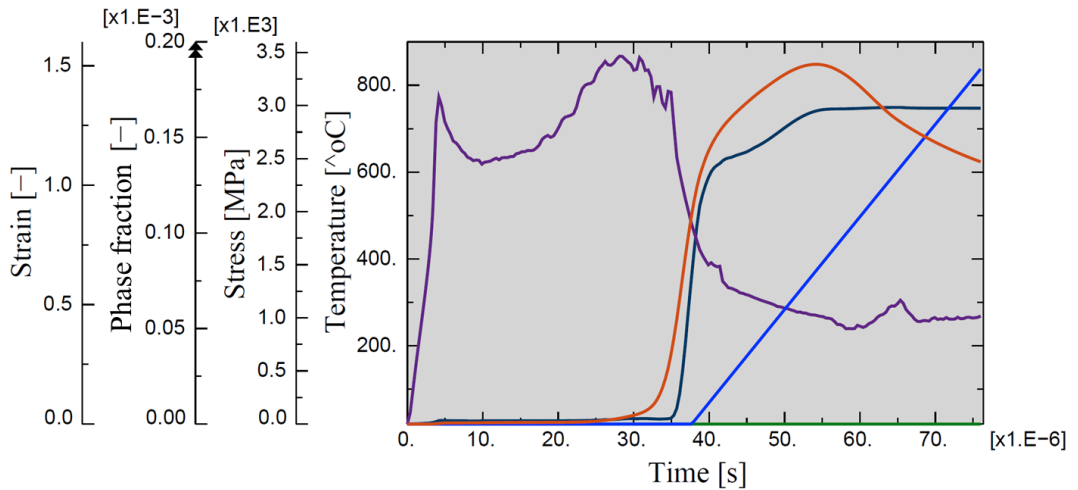
Figure 3.29: Cutting simulation: Variables of the plotted element with influence of the TRIP-strain
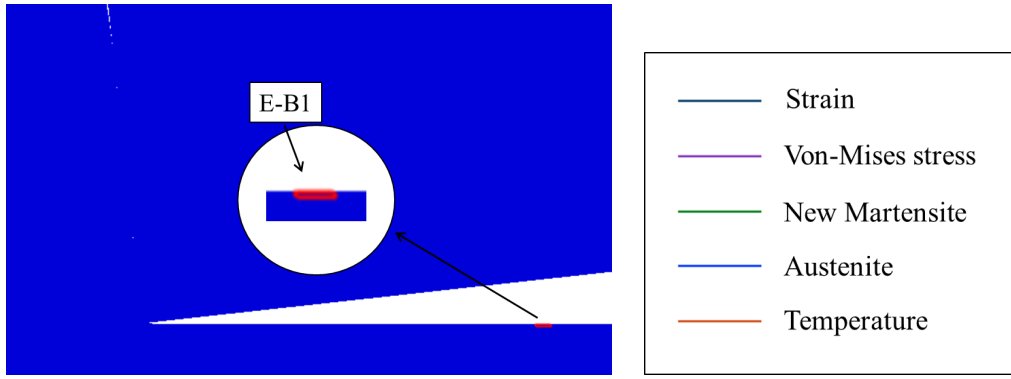
a) TRIP-strains activated
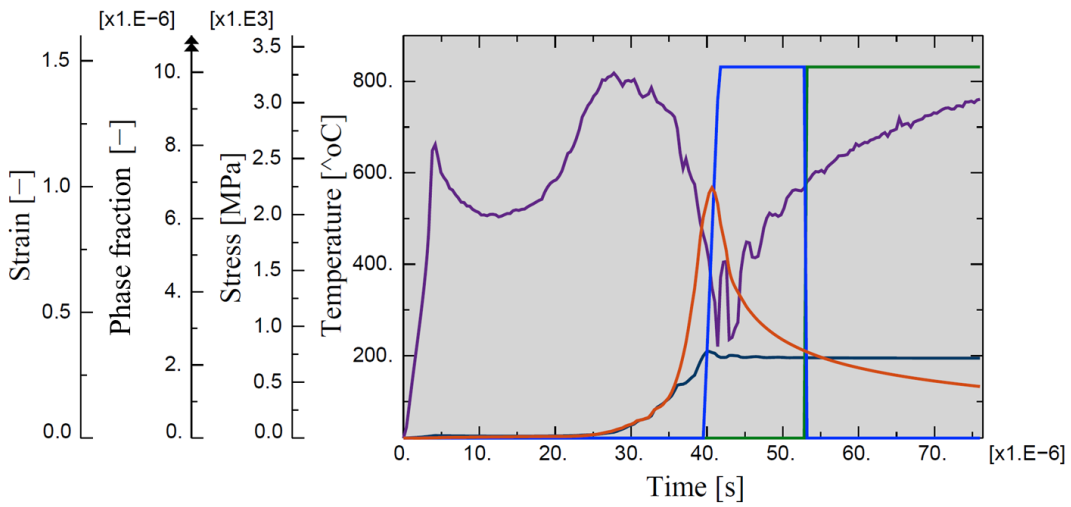
b) TRIP-strains deactivated
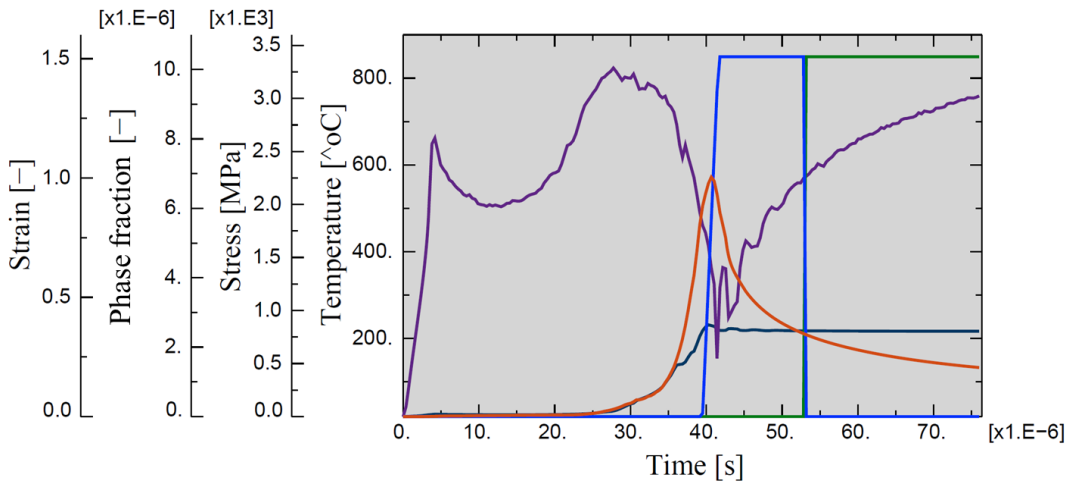
Figure 3.30: Cutting simulation: Variables of the plotted element with influence of TRIP-strains
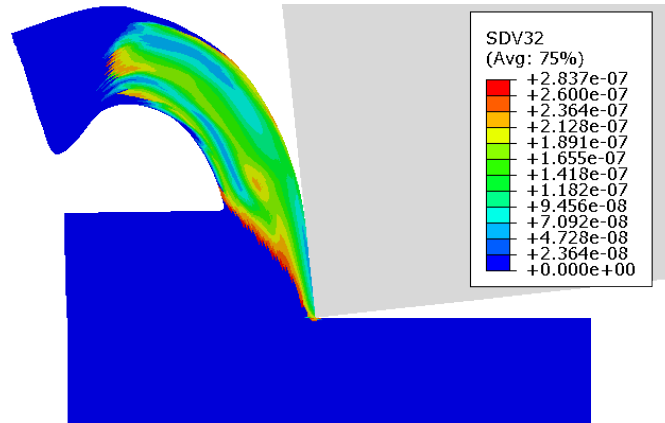
$t = 7.6 \cdot 10^{-5}$ s

Figure 3.31: Cutting simulation: Contours of the TRIP-factor w_A

3.6 Summary

In this chapter we have developed a multimechanism model for simulation of visco-plastic material behavior accompanied by phase transformations. The model is formulated within a thermodynamic framework for large strains. This general model has been specialized and applied to a cutting process in steel production. To this end, the Johnson-Cook yield function is extended to take into account visco-plastic asymmetric effects and transformation induced plastictiy. For a better description of the strain rate dependence, the original Johnson-Cook strain rate form has been replaced by the Huh-Kang rate form, which is quadratic dependent on the logarithmic strain rate. We are aware of its weakness, since it is not based on underlying physics such as dislocation theory. As a consequence, it should not be used outside the domain, where data exist. In the future, the methology developed on a thermodynmics framework should be extended to different models, such as the Zerilli-Armstrong model [92].

The phase transformations under consideration are: Transformation of the martensitic initial state into austenite, then retransformation to martensite. Thermodynamic consistency of the model developed has been proven. Moreover, this result does not depend on possible modifications within the evolution equations of phase transformations and of TRIP.

The finite-element simulation of mechanical behavior and phase transformations in a cutting process demonstrates the capability of the developed model to simulate realistically this process.

Chapter 4

Extension of the multi-mechanism model with a gradient of the austenite phase fraction based on the concept of generalized stresses

4.1 Introduction

In hard turning the workpiece is machined under high speed causing high strain rates and temperature, which can change material microstructure in workpiece surfaces affecting physical effects such as elasticity, plasticity, phase transformation and transformation induced plasticity (TRIP). In Chapter 3 we developed a multi-mechanism model based on the well-known Johnson-Cook model [44] and extended the inelastic behavior by an asymmetric effect. Concerning the rapid thermal-mechanical loading and cooling in cutting processes, we have taken into account phase transformations, where the martensitic initial state transforms into austenite and retransforms back to martensite. The martensitic retransformation is combined with a TRIP-strain. In this chapter, we go a step further and extend the multi-mechanism model according to the following items: **Extended continuum mechanics:** The consideration of the microstruture within material behavior is a big challenge for material modelling. *Extended continuum models* or (*generalized continua*, [63]) have been developed in the last century to account for size effects on the material's response. To physically motivate the size effect, the microstructure of steel AISI 52100 after hard turning is shown in Figure 4.1. In comparison to the bulk material, different microstructures are formed, one called white layer and another dark layer. The white layer forms due to the so-called reverse martensite transformation, which is schematically illustrated in Figure 4.2. In comparison, the microstructure of the new formed martensite is circular, which is much smaller than the initial martensite with acicular microstructure. Due to this size effect we have two type of interfaces: I. Interface between initial martensite and austenite. II. Interface between new formed martensite and austenite. Thus we have two type of surface energies, which leads to different macroscopic free energies. The size effect and the difference of the free energies can be considered in cutting simulations.

In order to account for the size effect and the difference of the free energies of two
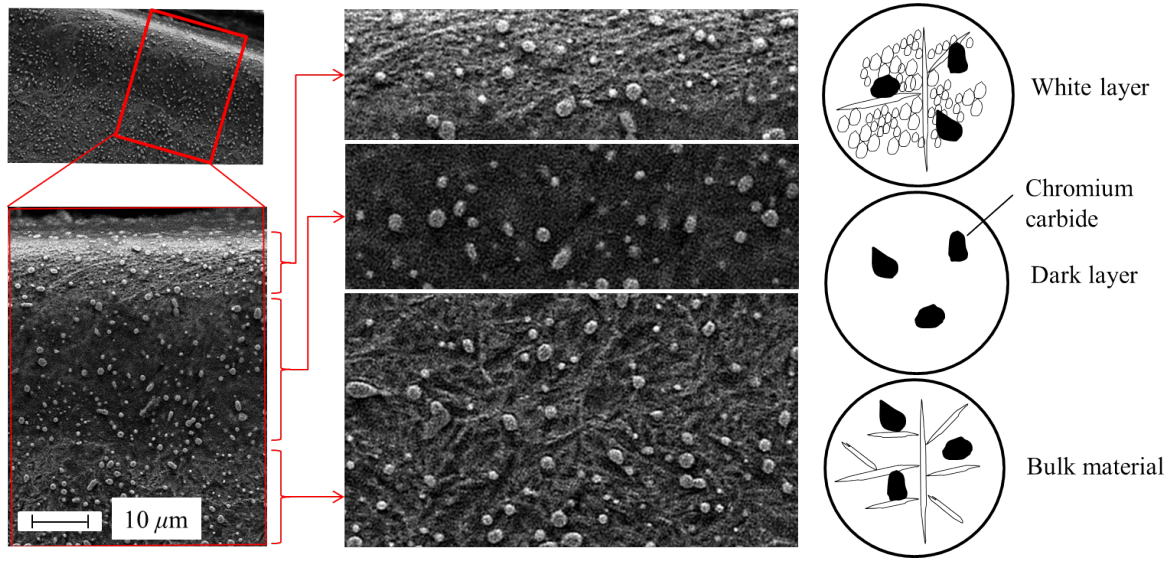
Figure 4.1: Microstructure of steel AISI 52100 after hard turning with formation of white layer and dark layer (LWK, University of Paderborn).
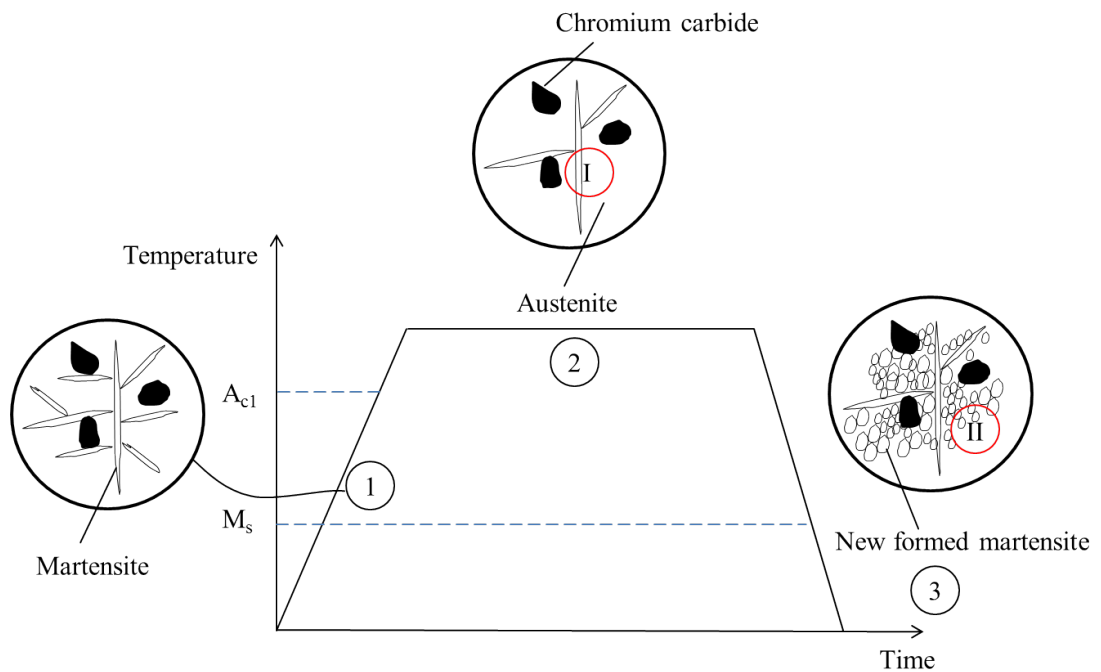
Figure 4.2: Schematic illustration of phase transformations with different interface types: I. Interface between initial martensite and austenite; II. Interface between new formed martensite and austenite.

type interfaces due to white layer formation, the multi-mechanism mode of Chapter 3 is extended with a phase gradient term based on the so-called concept of generalized stresses initially introduced by Gurtin [31] and extended by Forest, Ammar and Appolaire [27, 5].

Asymmetric hardness dependency: Guo *et al.* [30] study the influence of hardness of the material DIN 100Cr6 on material behavior under tension and find out that the yield stress and the tensile strength increase or decrease following a change of hardness. To describe this relationship, Umbrello *et al.* [80] propose a linear hardness-dependent function, which can be integrated into a flow function. In this chapter, instead of only studying the hardness dependency under tension, we also take compressional and torsional cases into account, where the concept of weighting functions introduced in [50] is used to model this asymmetric hardness dependency. Furthermore, experimental tests are investigated under tension, compression and shear at different hardened states for indicating the asymmetric hardness dependency and to identify related parameters.

Hardness modification due to white layer formation: As mentioned in Section 3.1 the white layer is induced due to austenitization and martensitic retransformation. Umbrello *et al.* [82] study the hardness of the white layer, and find that it is harder than the bulk material. They propose an empirical function, which takes the white layer formation and the influence of maximal reached temperature into account, to describe the hardness modification. In this chapter, we consider the hardness modification and integrate the empirical function into our multi-mechanism model.

This chapter is organized as follows:

- Section 4.2 presents a general setting and a constitutive framework based on the concept of generalized stresses. In the general setting we derive the balance relations for the macro and the micro scale by using the generalized principle of virtual power. In the constitutive framework we formulate the Clausius-Duhem inequality, which is split into an inelastic, a chemical and a thermal part. At the end of this section we derive the heat-conduction equation.

- In Section 4.3, we propose a Helmholtz energy and a prototype model. To this end, thermodynamic forces and evolution equations are formulated. For the visco-plastic part a new flow rule concerning hardness dependent bahavior is proposed, where the hardness modification is also taken into account. For the evolutions of the phases, both evolutions for austenite and martensite of Chapter 3 are extended with the phase gradient term. Finally, we prove the thermodynamic consistency of the model.

- In Section 4.4 some numerical aspects will shown on an element level due to the extended phase gradient, which is treated as an extra degree of freedom.

- In Section 4.5, further mechanical experiments are performed for parameter identification related to the hardness dependency. The tests are investigated under tension, compression and shear using different hardened specimens. Furthermore, some representative finite-element cutting simulations are investigated for testing our

model regarding the extensions, where the model is implemented as a user-defined element subroutine (VUEL) and linked to ABAQUS v6.14.

4.2 A thermodynamic framework based on the concept of generalized stresses

4.2.1 The concept of generalized stresses - general setting

Based on the theory of GURTIN [31] and FOREST [27], the classical continua used in Chapter 3 is extended to a non-classical continua. For the non-classical continua the placement $\mathbf{x}$ of Eq.(2.1) is complemented by additional *degrees of freedom* (DOF), which can represent scalars, vectors, tensors etc. In our case, the mass phase fractions z_i introduced in Eq.(2.17) are regarded as the additional DOFs. According to Gurtin's theory [31] a first gradient theory can be built with the sets

$$1. \ \text{DOF} = \{\mathbf{x}, \ \underline{z}\}, \qquad 2. \ \text{STRAIN} = \{\mathbf{F}, \ \underline{z}, \ \nabla \underline{z}\}, \tag{4.1}$$

where $\underline{z}$ are the additional DOFs in comparison to the classical continua. $\underline{z}$ and $\nabla \underline{z}$ are the additional STRAINs. Following [27], depending on the invariance properties the additional degrees of freedom $\underline{z}$ can contribute to the work of internal forces together with its gradient $\nabla \underline{z} \in I\!\!R^{n_z} \times \mathcal{E}^3$. This is a main contrast to internal variables and also to the placement $\mathbf{x}$ itself, since it is not an objective vector. Related to the STRAIN-set in Eq.(4.1.2) we introduce work conjugated (dual) STRESS-sets, such that the virtual power of internal forces is extended to the virtual power done by the additional degrees of freedom and its first gradient:

$$
\begin{aligned}
&1. \ \text{STRESS}^{(i)} = \{\mathbf{P}, -\underline{\pi}, \boldsymbol{\xi}\} &&\implies&& p^{(i)}[\delta \mathbf{x}, \delta \underline{z}] = \mathbf{P} : \delta \mathbf{F} - \underline{\pi} \cdot \delta \underline{z} + \boldsymbol{\xi} : \delta \nabla \underline{z} \\
&2. \ \text{STRESS}^{(e)} = \{\mathbf{f}, \underline{\pi}^e, \boldsymbol{\xi}^e\} &&\implies&& p^{(e)}[\delta \mathbf{x}, \delta \underline{z}] = \mathbf{f} \cdot \delta \mathbf{x} + \underline{\pi}^e \cdot \delta \underline{z} + \boldsymbol{\xi}^e : \delta \nabla \underline{z} \\
&3. \ \text{STRESS}^{(c)} = \{\mathbf{t}, \underline{\pi}^c, \boldsymbol{\xi}^c\} &&\implies&& p^{(c)}[\delta \mathbf{x}, \delta \underline{z}] = \mathbf{t} \cdot \delta \mathbf{x} + \underline{\pi}^c \cdot \delta \underline{z} + \boldsymbol{\xi}^c : \delta \nabla \underline{z}.
\end{aligned}
\tag{4.2}
$$

Here, $p^{(i)}$, $p^{(e)}$ and $p^{(c)}$ represent the *virtual power densities of internal, external* and *contact generalized forces*, respectively. $\mathbf{P}$ and $\mathbf{t}$ are the first Piola-stress tensor and the macro traction vector introduced in Eq.(2.29), respectively. $\mathbf{f}$ is the body force introduced in Eq.(2.34.1). $\underline{\pi} \in I\!\!R^{n_z}$ and $\boldsymbol{\xi} \in I\!\!R^{n_z} \times \mathcal{E}^3$ are generalized forces and stresses, work conjugate to the additional degrees of freedom $\underline{z}$ and its gradients $\nabla \underline{z}$. The generalized body forces $\underline{\pi}^e$ and $\boldsymbol{\xi}^e$ and traction forces $\underline{\pi}^c$ and $\boldsymbol{\xi}^c$, work conjugate to $\underline{z}$ and $\nabla \underline{z}$, respectively, are assumed to be $\underline{\pi}^e = \underline{\pi}^c = \underline{0}$ and $\boldsymbol{\xi}^e = \boldsymbol{\xi}^c = \mathbf{0}$ for simplicity in our case. Note, the stress $\mathbf{P}$, the forces $\mathbf{f}$ and $\mathbf{t}$ belong to the classical continua, the rest of the STRESS in Eq.(4.2) are additional stresses or forces for the non-classical continua.

Upon introducing the virtual powers in global form, for internal, external and contact

generalized forces with respect to the reference configuration $\mathcal{B}_0$

$$
\begin{aligned}
1.\ \mathcal{P}^{(i)} &= -\int_{\mathcal{B}_0} p^{(i)}[\delta\mathbf{x}, \delta\underline{z}]dV, \\
2.\ \mathcal{P}^{(e)} &= \int_{\mathcal{B}_0} p^{(e)}[\delta\mathbf{x}, \delta\underline{z}]dV, \\
3.\ \mathcal{P}^{(c)} &= \int_{\partial\mathcal{B}_0} p^{(c)}[\delta\mathbf{x}, \delta\underline{z}]dA
\end{aligned}
\tag{4.3}
$$

and assuming that no inertial microforces exist, the generalized principle of virtual power reads [5]

$$
\mathcal{P}^{(i)} + \mathcal{P}^{(e)} + \mathcal{P}^{(c)} = 0 \qquad \forall\delta\mathbf{x}, \forall\delta\underline{z}, \forall\mathcal{B}_0. \tag{4.4}
$$

Inserting the relations (4.3) into Eq.(4.4) and applying the divergence theorem one obtains

$$
\begin{aligned}
&\int_{\mathcal{B}_0}(\mathbf{P}\cdot\nabla + \mathbf{f})\cdot\delta\mathbf{x}dV \quad + \quad \int_{\partial\mathcal{B}_0}(\mathbf{t} - \mathbf{P}\cdot\mathbf{N})\cdot\delta\mathbf{x}dA \\
+ \ &\int_{\mathcal{B}_0}(\boldsymbol{\xi}\cdot\nabla + \underline{\pi})\,\delta\underline{z}\,dV \quad + \quad \int_{\partial\mathcal{B}_0}(\boldsymbol{\xi}\cdot\mathbf{N})\delta\underline{z}dA = 0.
\end{aligned}
\tag{4.5}
$$

which render the local forms

$$
\begin{aligned}
&1.\ \ \mathbf{P}\cdot\nabla + \mathbf{f} = \mathbf{0}\ \text{ in }\mathcal{B}_0, \quad 2.\ \ \mathbf{t} = \mathbf{P}\cdot\mathbf{N}\ \text{ on }\partial\mathcal{B}_0^{\mathbf{P}}, \\
&3.\ \ \boldsymbol{\xi}\cdot\nabla + \underline{\pi} = \mathbf{0}\ \text{ in }\mathcal{B}_0, \quad 4.\ \ \boldsymbol{\xi}\cdot\mathbf{N} = \mathbf{0}\ \text{ on }\partial\mathcal{B}_0^{\boldsymbol{\xi}}.
\end{aligned}
\tag{4.6}
$$

Here, Eq.(4.6.1) and Eq.(4.6.2) are the static equilibrium and the associated boundary condition for the macro scale introduced in Eq.(2.36). Eq.(4.6.3) and Eq.(4.6.4) are the extended equilibrium and the associated boundary condition for the micro scale in the non-classical continua. $\mathcal{B}_0^{\boldsymbol{\xi}}$ is the Neumann boundary for the micro scale. The density of internal power $p^{(i)}$ defined in Eq.(2.34) for the classical continua is now extended for the non-classical continua as

$$
p^{(i)}(\dot{\mathbf{x}}, \dot{\underline{z}}) = \mathbf{P} : \dot{\mathbf{F}} - \underline{\pi}\dot{\underline{z}} + \boldsymbol{\xi} : \nabla\dot{\underline{z}}, \tag{4.7}
$$

where $\underline{\pi}\dot{\underline{z}}$ and $\boldsymbol{\xi} : \nabla\dot{\underline{z}}$ are additional powers related to the additional STRAINs $\underline{z}$ and $\nabla\underline{z}$, respectively. In the sequel of this chapter, the general setting for the concept of generalized stresses for generalized continua is exploited to extend the multi-mechanism model of Chapter 3 (MMM) with gradient phase transformations.

4.2.2 Constitutive framework

Analogously to the STATE-definition of the original MMM in Eq.(3.1) and taking the additional STRAIN $\nabla\underline{z}$ in Eq.(4.1.2) into account, state variables are selected as

$$
\text{STATE} = \{\overline{\mathbf{C}}_e, \underline{q}, \underline{z}, \nabla\underline{z}, \theta\}. \tag{4.8}
$$

Furthermore, the Helmholtz energy Ψ of Eq.(2.34.3) is assumed as

$$
\Psi = \Psi[\overline{\mathbf{C}}_e, \underline{q}, \underline{z}, \nabla\underline{z}, \theta]. \tag{4.9}
$$

According to the derivation of Eq.(3.3) and concerning the special definition in Eq.(4.7) and the extra STATE variable $\nabla \underline{z}$ the Clausius-Duhem inequality (2.34.3) – with quantities with respect to the intermediate configuration – reads as

$$
\left(\overline{\mathbf{M}} - \rho_0 2 \overline{\mathbf{C}}_e \cdot \frac{\partial \Psi}{\partial \overline{\mathbf{C}}_e} \right) : \bar{\mathbf{L}} + \left(\boldsymbol{\xi} - \rho_0 \frac{\partial \Psi}{\partial \nabla \underline{z}} \right) \cdot \nabla \dot{\underline{z}} + \left(\eta + \frac{\partial \Psi}{\partial \theta} \right) \dot{\theta}
$$
$$
+ \quad \rho_0 2 \overline{\mathbf{C}}_e \cdot \frac{\partial \Psi}{\partial \overline{\mathbf{C}}_e} : \bar{\mathbf{L}}_i - \rho_0 \frac{\partial \Psi}{\partial \underline{q}} \dot{\underline{q}} - \left(\underline{\pi} + \rho_0 \frac{\partial \Psi}{\partial \underline{z}} \right) \dot{\underline{z}} - \frac{1}{\theta} \mathbf{q}_0 \cdot \nabla \theta \geq 0.
\tag{4.10}
$$

Next, we define the thermodynamic forces

$$
1. \ \overline{\mathbf{M}} = \rho_0 2 \overline{\mathbf{C}}_e \frac{\partial \Psi}{\partial \overline{\mathbf{C}}_e}, \quad 2. \ \boldsymbol{\xi} = \rho_0 \frac{\partial \Psi}{\partial \nabla \underline{z}}, \quad 3. \ \eta = -\frac{\partial \Psi}{\partial \theta},
$$
$$
4. \ \underline{Q} = \rho_0 \frac{\partial \Psi}{\partial \underline{q}}, \quad 5. \ \underline{Z}_\nabla = \rho_0 \frac{\partial \Psi}{\partial \underline{z}} + \underline{\pi}.
\tag{4.11}
$$

In comparison to Eq.(3.4) we have an additional relation Eq.(4.11.2) and the different chemical forces $\underline{Z}_\nabla$. The following inequalities are sufficient for the validity of the Clausius-Duhem inequality (2.34.3)

$$
1. \ \mathcal{D}^i = \overline{\mathbf{M}} : \bar{\mathbf{L}}_i - \underline{Q} \ \dot{\underline{q}} \geq 0, \ 2. \ \mathcal{D}^z = -\underline{Z}_\nabla \ \dot{\underline{z}} \geq 0, \ 3. \ \mathcal{D}^\theta = -\frac{1}{\theta} \mathbf{q}_0 \cdot \nabla \theta \geq 0. \tag{4.12}
$$

In Section 4.3.2 we will formulate the following evolution equations to fulfil the inequalities (4.12.1) and (4.12.2):

$$
1. \ \bar{\mathbf{L}}_i = \bar{\mathbf{L}}_i \left[\overline{\mathbf{M}}, \underline{Q}, \underline{Z}_\nabla, \underline{q}, \underline{z}, \nabla \underline{z}, \theta \right], \quad 2. \ \dot{\underline{q}} = \dot{\underline{q}} \left[\overline{\mathbf{M}}, \underline{Q}, \underline{Z}_\nabla, \underline{q}, \underline{z}, \nabla \underline{z}, \theta \right],
$$
$$
3. \ \dot{z}_A = \dot{z}_A \left[\overline{\mathbf{M}}, \underline{Q}, \underline{Z}_\nabla, \underline{q}, \underline{z}, \nabla \underline{z}, \theta \right].
\tag{4.13}
$$

The chemical dissipation $\mathcal{D}^z$ in Eq.(4.12.2) must be non-negative and a function of the phase evolution $\dot{\underline{z}}$. Analogously to AMMAR *et al.* [5] for a mesoscopic case we postulate the existence of a non-negative chemical dissipation as a multiplication of a positive constant β and a non-negative quadratic term $\dot{\underline{z}}^2$, that is

$$
\mathcal{D}^z = \beta \dot{\underline{z}}^2.
\tag{4.14}
$$

Comparing this relation to the relation (4.12.2) one obtains

$$
\underline{Z}_\nabla = -\beta \dot{\underline{z}}.
\tag{4.15}
$$

Inserting Eq.(4.11.2) into Eq.(4.6.3), solving for $\underline{\pi}$ and inserting again into Eq.(4.11.5) we obtain

$$
\underline{Z}_\nabla = \rho \frac{\partial \Psi}{\partial \underline{z}} - \nabla \cdot \boldsymbol{\xi} = \rho \frac{\partial \Psi}{\partial \underline{z}} - \rho \nabla \cdot \frac{\partial \Psi}{\partial \nabla \underline{z}}.
\tag{4.16}
$$

Comparing Eq.(4.15) and Eq.(4.16) renders

$$\rho \frac{\partial \Psi}{\partial \underline{z}} - \rho \nabla \cdot \frac{\partial \Psi}{\partial \nabla \underline{z}} = -\beta \dot{\underline{z}}. \tag{4.17}$$

This equation expresses the relation between the Helmholtz energy Ψ and the evolution of phase transformation $\dot{\underline{z}}$, and will be used as a constraint for deriving the evolution equation of phase fractions in Section 4.3.2.

Eq.(4.17) is actually a Cahn-Allen- or (time dependent) Ginzburg-Landau-equation in the terminology of phase field models (see e.g. [16, 31]). In classical phase field models the gradient term can be seen as a regularization of sharp interfaces and this term can be associated with an interface energy. In this chapter, the extended gradient term affects the phase transformations (see Section 4.3.2) and takes the size effect into account as mentioned in Section 1.1.

4.2.3 Heat-conduction equation

Analogously to the derivation of Eq.(3.14) and using the relations (2.13.1), (2.32), (4.7) and (4.11), the heat-conduction equation of the constitutive framework introduced above can be obtained from Eq.(2.34.2):

$$\begin{aligned}
\rho_0\, c_d\, \dot{\theta} + \nabla \mathbf{q}_0 \;=\;& \overline{\mathbf{M}} : (\bar{\mathbf{L}}_i + \bar{\mathbf{L}}_\theta + \bar{\mathbf{L}}_z) - \underline{Q}\, \dot{\underline{q}} - \underline{Z}_\nabla \dot{\underline{z}} - \boldsymbol{\xi} \cdot \nabla \dot{\underline{z}} \\[2mm]
& + \theta\, \frac{\partial \overline{\mathbf{M}}}{\partial \theta} : \bar{\mathbf{L}}_e + \theta\, \frac{\partial Q}{\partial \theta}\, \dot{\underline{q}} + \theta\, \frac{\partial \underline{Z}_\nabla}{\partial \theta}\, \dot{\underline{z}} + \theta\, \frac{\partial \boldsymbol{\xi}}{\partial \theta} \cdot \nabla \dot{\underline{z}} + \rho_0 r_\theta.
\end{aligned} \tag{4.18}$$

Here c_d is the heat capacity defined in Eq.(3.15).

4.3 A prototype model for cutting processes

Analogously to the formulation of the prototype model MMM in Section 4.3, the general thermodynamic framework in Section 4.2.2 is now specialized to the scenario of a cutting process. To this end, we make concrete proposals for the Helmholtz energy as well as for the evolution of internal variables. Finally, we discuss the thermodynamic consistency of the model extended below. We have the same phases as in Chapter 3:

$$\begin{aligned}
z_A & \quad \text{for austenite} \\
z_M & \quad \text{for martensite.}
\end{aligned} \tag{4.19}$$

The austenite fraction z_A is regarded as the additional DOF z_A in Eq.(4.1) with $\underline{z} \equiv z_A$. Since only two phases occur, the martensite fraction can be expressed as

$$z_M = 1 - z_A. \tag{4.20}$$

4.3.1 Helmholtz energy

Concerning thermo-mechanical effects and phase transformations with an extended phase gradient for the special cutting process, we propose the Helmholtz free energy Ψ:

$$
\begin{aligned}
1.\ \Psi \ &= \Psi^{iso}[\overline{\mathbf{C}}_e, \theta] + \Psi^{vol}[\overline{\mathbf{C}}_e, z_A, \nabla z_A, \theta] + \Psi^{\theta}[\theta] + \Psi^p[\underline{q}, z_A, \nabla z_A, \theta] \\
&\quad + \Psi^{ch}[z_A, \nabla z_A, \theta], \ \text{where}
\end{aligned}
$$

$$
2.\ \Psi^{iso} = \frac{G[\theta]}{4\rho_0}\left(\mathrm{tr}\left[\ln \hat{\mathbf{C}}_e\right]^2\right)
$$

$$
3.\ \Psi^{vol} = \frac{1}{2\rho_0}K[\theta]\left(\ln J_e\right)^2
$$

$$
4.\ \Psi^{\theta} = \int_{\theta_0}^{\theta} c_d[\bar{\theta}]d\bar{\theta} - \theta \int_{\theta_0}^{\theta} \frac{c_d[\bar{\theta}]}{\bar{\theta}}d\bar{\theta},
$$

$$
5.\ \Psi^p = \Psi^{p1} + \Psi^{p2} = \frac{1}{2\rho_0}H_1 q_1^2 + \frac{1}{2\rho_0}H_2 q_2^2,
$$

$$
6.\ \Psi^{ch} = \Psi^{grad} + \Psi^{pot} = \frac{1}{2}\mu(\nabla z_A)^2 + (z_A - z_{0A})\phi_{ch,A}[\theta].
$$

(4.21)

The parts Ψ^{iso}, Ψ^{vol}, Ψ^{θ} and Ψ^p are identical to the proposals in Eq.(3.17). The chemical part Ψ^{ch} represents the chemically stored energy with respect to phase transformations. In comparison to the potential energy Ψ^{pot} in Eq.(3.17.6) we consider an extra gradient part Ψ^{grad}. μ is a constant.

Remark 4.1

The thermodynamic forces $\overline{\mathbf{M}}$, Q_1 and Q_2 remain unchanged as given in Eq.(3.22). The forces $\boldsymbol{\xi}$ and $\underline{Z}_{\nabla} \equiv Z_A$ are obtained from the relations (4.11):

$$
\begin{aligned}
1.\ \boldsymbol{\xi} \ &= \ \rho_0\frac{\partial\Psi^{ch}}{\partial\nabla z_A} = \rho_0\mu\nabla z_A, \\
2.\ Z_A \ &= \ \rho_0\frac{\partial\Psi^{ch}}{\partial z_A} - \rho_0\nabla\cdot\frac{\partial\Psi^{ch}}{\partial\nabla z_A} = -\rho_0\mu\nabla^2 z_A + \rho_0\phi_{ch,A}[\theta].
\end{aligned}
$$

(4.22)

4.3.2 Evolution equations

Identical to Eq.(3.33), the inelastic part of the velocity gradient $\bar{\mathbf{L}}_i$ is decomposed additively as

$$
\bar{\mathbf{L}}_i = \bar{\mathbf{L}}_p + \bar{\mathbf{L}}_t,
$$

(4.23)

where $\bar{\mathbf{L}}_p$ and $\bar{\mathbf{L}}_t$ represent the visco-plastic and the TRIP part, respectively. In this section we extend the visco-plasticity with an asymmetric hardness dependency and consider the hardness modification with the aid of an empirical function.

A hardness dependent flow rule

UMBRELLO *et al.* [80] show that yield stress and the tensile strength of AISI 52100 increase if the material becomes harder. They propose a linear function

$$F + Ge_v \tag{4.24}$$

with

$$1.\ F(\mathcal{H}) = F_1 \cdot \mathcal{H} - F_2, \quad 2.\ G(\mathcal{H}) = G_1 \cdot \mathcal{H} - G_2 \tag{4.25}$$

to describe this dependency. Here, $\mathcal{H}$ is the hardness, which can be changed due to the white layer formation. F_1, F_2, G_1, and G_2 are material parameters.

Eq.(4.24) allows itself to be integrated into the yield function Eq.(3.30.1). Thus we have

$$\Phi \;=\; \sigma_v - (Y_0 + F + Ge_v + Q_1 + Q_2)\,\mathcal{J}, \tag{4.26}$$

where the term $Y_0 + F$ represents the initial flow stress of a new hardened state. The function Ge_v describes the variation of the yield stress with a change of hardness. The total barrier $Y_0 + F + Ge_v$ is defined to be non-negative. In order to take the asymmetric dependency of hardness into account, we weight the parameters with the weighting functions w_i as in Eq.(3.45)

$$1.\ F_1 = \sum_{i=1}^{S} w_i F_{1i}, \quad 2.\ F_2 = \sum_{i=1}^{S} w_i F_{2i}, \quad 3.\ G_1 = \sum_{i=1}^{S} w_i G_{1i}, \quad 4.\ G_2 = \sum_{i=1}^{S} w_i G_{2i}. \tag{4.27}$$

A hardness modification due to white layer formation

UMBRELLO *et al.* [82] find that the material becomes harder than the bulk material due to white layer formation and describe the hardness modification with an empirical function

$$
\begin{aligned}
1.\ \mathcal{H} \;\; &= \mathcal{H}_{init} + \Delta\mathcal{H} \\
2.\ \Delta\mathcal{H} \;\; &= F_{\mathcal{H}} \tfrac{\mathcal{H}_r - \mathcal{H}_{init}}{\theta_r - A_{c1}} (\theta_{max} - A_{c1}) \cdot H(\theta_{max} - A_{c1}) \cdot H(\theta_{MS} - \theta)
\end{aligned}
\tag{4.28}
$$

where $\mathcal{H}_{init}$ is the hardness of the bulk material. $\Delta\mathcal{H}$ represents the change of the hardness. $\mathcal{H}_r$ and θ_r are parameters representing the reference hardness and the reference temperature. θ_{max} is the maximal temperature and if it is greater than the austenitization start temperature A_{c1}, austenitization occurs. This relation is interpreted by the switch function $H(\theta_{max} - A_{c1})$. During quenching, as soon as the temperature becomes lower than the martensite start temperature θ_{MS}, the white layer forms and the hardness changes, which can be interpreted by the switch function $H(\theta_{MS} - \theta)$. The parameters A_{c1} and θ_{MS} are given in Section 3.3.6. The maximal temperature determines the hardness level of the white layer. $F_{\mathcal{H}}$ is a control quantity. The parameters for the hardness modification are summarized as $\kappa_{\mathcal{H}} = [\mathcal{H}_r, \theta_r, F_{\mathcal{H}}]$. $\mathcal{H}_r$ and θ_r are empirically chosen as $\mathcal{H}_r = 67$ HRC and $\theta_r = 1030$ °C by UMBRELLO *et al.* [82].

$I.$	Flow rule	$\bar{\mathbf{L}}_p = \dot{\lambda}\sqrt{\dfrac{3}{2}}\mathbf{N}$
$II.$	Flow direction	$\mathbf{N} = \dfrac{\overline{\mathbf{M}}^{dev}}{||\overline{\mathbf{M}}^{dev}||}$
$III.$	Flow factor	$\dot{\lambda} = \dot{e}_v = \sqrt{\dfrac{2}{3}\bar{\mathbf{L}}_p : \bar{\mathbf{L}}_p}$
$IV.$	Yield function	$\Phi = \sigma_v - \left(Y_0 + F + Ge_v + Q_1 + Q_2\right)\mathcal{J}$
$V.$	von Mises stress	$\sigma_v = \sqrt{\dfrac{3}{2}}||\overline{\mathbf{M}}^{dev}||$
$VI.$	Hardness functions	$F(\mathcal{H}) = F_1 \cdot \mathcal{H} - F_2, \quad G(\mathcal{H}) = G_1 \cdot \mathcal{H} - G_2$
$VII.$	Hardness modification	$\mathcal{H} = \mathcal{H}_{init} + \Delta\mathcal{H}$
		$\Delta\mathcal{H} = F_{\mathcal{H}} \frac{\mathcal{H}_r - \mathcal{H}_{init}}{\theta_r - A_{c1}}(\theta_{max} - A_{c1}) \cdot H(\theta_{max} - A_{c1})$
		$\cdot H(\theta_{MS} - \theta)$
$VIII.$	Hardening stresses	$\dot{Q}_1 = \dot{\lambda}\mathcal{J}\left(H_1 - cQ_1\right), \quad \dot{Q}_2 = \dot{\lambda}H_2\mathcal{J}$
$IX.$	JC coefficient	$\mathcal{J} = \mathcal{J}^\theta \mathcal{J}_{HK}^R \geq 0, \quad \mathcal{J}^\theta = (1 - (\theta^*)^m)$
$X.$	HK coefficient	$\mathcal{J}_{HK}^R = 1 + C_1 \ln\left(\left\langle\dfrac{\dot{e}_v}{\dot{\varepsilon}_0}\right\rangle_1\right) + C_2 \left(\ln\left(\left\langle\dfrac{\dot{e}_v}{\dot{\varepsilon}_0}\right\rangle_1\right)\right)^2$
$XI.$	Weighted constants	$F_1 = \sum\limits_{i=1}^{S} w_i F_{1i}, \quad F_2 = \sum\limits_{i=1}^{S} w_i F_{2i}, \quad G_1 = \sum\limits_{i=1}^{S} w_i F_{1i}$
		$G_2 = \sum\limits_{i=1}^{S} w_i G_{2i}, \quad H_1 = \sum\limits_{i=1}^{S} w_i H_{1i}, \quad H_2 = \sum\limits_{i=1}^{S} w_i H_{2i},$
		$c = \sum\limits_{i=1}^{S} w_i c_i, \quad C_1 = \sum\limits_{i=1}^{S} w_i C_{1i}, \quad C_2 = \sum\limits_{i=1}^{S} w_i C_{2i},$
		$\dot{\varepsilon}_0 = \sum\limits_{i=1}^{S} w_i \dot{\varepsilon}_{0i}, \quad m = \sum\limits_{i=1}^{S} w_i m_i$
$XII.$	Material parameters	$\boldsymbol{\kappa}_{pl} = [F_{1i}, F_{2i}, G_{1i}, G_{2i}, Y_{0i}, H_{1i}, H_{2i}, c_i, C_{1i}, C_{2i},$
		$\dot{\varepsilon}_{0i}, m_i]^T, \; i = 1, ..., S$
		$\boldsymbol{\kappa}_{\mathcal{H}} = [\mathcal{H}_r, \theta_r, F_{\mathcal{H}}]$

Table 4.1: Constitutive equations for visco-plasticity combining hardness dependency

The new approach related to visco-plasticity with additional hardness dependency is summarized in Table 4.1. The flow rule Eq.I, the flow direction Eq.II, the flow factor

Eq.III, the von Mises stress Eq.V, the hardening stresses, the Johnson-Cook coefficient Eq.IX and the Huh-Kang coefficient Eq.X are identical to the terms given in Table 3.1. In the yield function Eq.IV $F + Ge_v$ is the additional term for representing the hardness dependency, F and G are functions of the hardness given in VI. The hardness modification due to white layer formation is given in Eq.VII. Analogously to Table 3.1, the asymmetric effect is considered by weighting the constants in the equations XI. All related material parameters are summarized in Eq.XII.

Evolution of phase fractions

In this subsection we intend to formulate phase transformations with an extended gradient term. For the case of austenitic transformation an approach due to LEBLOND and DEVAUX [46] and for the case of retransformation the classical Koistinen-Marburger [45] approach are used. Both approaches are extended by the gradient of austenite phase fraction ∇z_A.

Based on the constraint in Eq.(4.17) we obtain the evolution equation of austenite phase fraction in relation of the chemical free energy as

$$\dot{z}_A = -\frac{1}{\beta}\left(\rho_0\frac{\partial\Psi}{\partial z_A} - \rho_0\nabla\cdot\frac{\partial\Psi}{\partial\nabla z_A}\right). \tag{4.29}$$

For the sake of simplicity we assume that only the chemical part Ψ^{ch} affects the partial derivations $\partial\Psi/\partial z_A$ and $\partial\Psi/\partial\nabla z_A$. Thus Eq.(4.29) rewrites as

$$\dot{z}_A = -\frac{1}{\beta}\left(\rho_0\frac{\partial\Psi^{ch}}{\partial z_A} - \rho_0\nabla\cdot\frac{\partial\Psi^{ch}}{\partial\nabla z_A}\right). \tag{4.30}$$

Inserting Eq.(4.21) into this relation the transformation of austenite is formulated as:

$$\dot{z}_A = \frac{\rho_0\mu}{\beta}\nabla^2 z_A + \frac{\rho_0\phi_{ch,A}[\theta]}{\beta}. \tag{4.31}$$

A simple assumption of the term $\rho_0\phi_{ch,A}[\theta]/\beta$ is the approach due to LEBLOND and DEVAUX [46] as in Eq.(3.54). Thus the austenitic transformation is formulated as

$$\dot{z}_A = \alpha\nabla^2 z_A + \mu_{MA}(1 - z_A)H(\theta - A_{c1}) \quad\text{with}\quad \alpha = \frac{\rho_0\mu}{\beta}. \tag{4.32}$$

Here $\mu_{MA} > 0$ is a constant and A_{c1} is the austenite start temperature. The Heaviside function H with $H(s) = 1$ for $s > 0$ and $H(s) = 0$ for $s \leq 0$, otherwise, plays the role of a switcher. α represents the effect of the extended gradient term ∇z_A.

Analogously, the martensitc transformation Eq.(3.55) is due to Koistinen-Marburger [45] and extended as

$$\dot{z}_M = \alpha\nabla^2 z_M + \left\langle\frac{-\dot{\theta}}{k_\theta}\right\rangle(1 - z_M)H(\theta_{MS} - \theta). \tag{4.33}$$

$k_\theta > 0$ is the Koistinen-Marburger parameter, and θ_{MS} is the martensite start temperature.

According to Eq.(4.20) we have

$$1.\ \dot{z}_A = -\dot{z}_M, \quad 2.\ \nabla^2 z_A = -\nabla^2 z_M. \tag{4.34}$$

Inserting Eq.(4.34) into Eq.(4.33) and combining with Eq.(4.32) we obtain

$$\dot{z}_A = \begin{cases} \alpha \nabla^2 z_A + \mu_{MA}(1 - z_A), & \text{if } \theta > A_{c1} \\[2mm] -\alpha \nabla^2 z_A + \left\langle \dfrac{-\dot{\theta}}{k_\theta} \right\rangle z_A, & \text{if } \theta < \theta_{MS} \text{ and } \dot{\theta} < 0 \\[2mm] 0, & \text{else.} \end{cases} \tag{4.35}$$

4.3.3 Thermodynamic consistency

For thermodynamic consistency of the inelastic approach under consideration it is sufficient, that the inequalities (4.12.1) and (4.12.2) are fulfilled.

In comparison to Eq.(3.56) and using Eq.(4.26), inequality (4.12.1) rewrites as

$$
\begin{aligned}
\mathcal{D}^i &= \overline{\mathbf{M}} : \bar{\mathbf{L}}_i - Q_1 \dot{q}_1 - Q_2 \dot{q}_2 \\
&= \dot{\lambda} \underbrace{\left(\sigma_v - (Q_1 + Q_2)\, \mathcal{J} \right)}_{\geq (Y_0 + F + Ge_v)\mathcal{J}} + \dot{\lambda} c \frac{Q_1^2}{H_1} \mathcal{J} \\
&\quad + \begin{cases} \dot{z}_A \dfrac{3}{2} f'_A K_{tpA} \|\overline{\mathbf{M}}^{dev}\|^2 & \text{for } \dot{z}_A > 0 \\[2mm] \dot{z}_M \dfrac{3}{2} f'_M K_{tpM} \|\overline{\mathbf{M}}^{dev}\|^2 & \text{for } \dot{z}_M > 0 \end{cases} \geq 0.
\end{aligned}
\tag{4.36}
$$

The flow factor $\dot{\lambda}$ is defined to be non-negative. Additionally, the term $Y_0 + F + Ge_v$ is defined as positive and the term $\mathcal{J}$ is non-negative. Therefore, the first term becomes non-negative. The second term and the third term are already proven to be non-negative in Eq.(3.56). Thus, the validity of the inequality (4.12.1) is proven.

Furthermore, due to the derivation of the phase evolutions (4.32) and (4.33) by using the constraint Eq.(4.17), the assumption Eq.(eqDisqz) is valid. Therefore,

$$\mathcal{D}^z = \beta \dot{\underline{z}}^2 \geq 0. \tag{4.37}$$

Thus, the validity of the inequality (4.12.2) is also proven.

4.3.4 Summary of constitutive equations

The constitutive relations of our extended multi-mechanism model are summarized in Eq.(I) to Eq.(IV) of Table 4.2 including all parameters.

I. Mandel stress tensor

1. $\overline{\mathbf{M}} \quad = \quad K[\theta] \ln J_e \overline{\mathbf{1}}' + G[\theta] \mathrm{dev} \ln\left(\overline{\mathbf{C}}_e\right) - K[\theta]\left(3\Delta\theta\,\alpha_M[\theta] + K_{tv} z_A\right)\mathbf{1}$

2. $G(\theta) \quad = \quad \dfrac{2E(\theta)}{1+\nu}, \quad K(\theta) = \dfrac{E(\theta)}{3(1-2\nu)}, \quad E = E_0 + c_E\left(\theta - \theta_{E_0}\right)$

II. Inelastic flow

- Additive decomposition $\quad \overline{\mathbf{L}}_i = \overline{\mathbf{L}}_p + \overline{\mathbf{L}}_t$

- Visco-plastic flow $\overline{\mathbf{L}}_p$: see Table 4.1

- TRIP flow $\overline{\mathbf{L}}_t$: see Table 3.2

III. Phase transformation (PT) kinetics

- Martensite $\to$ Austenite $(M \to A)$:

  1. $\dot{z}_A \quad = \quad \alpha\nabla^2 z_A + \mu_{MA}\left(1 - z_A\right)H(\theta - A_{c1})$

- Austenite $\to$ Martensite $(A \to M)$:

  2. $\dot{z}_M \quad = \quad \alpha\nabla^2 z_M + \left\langle \dfrac{-\dot{\theta}}{k_\theta}\right\rangle(1 - z_M)H(\theta_{MS} - \theta)$

IV. Material parameters

1. $\boldsymbol{\kappa}_{gr} \quad = \quad [\alpha]^T$ $\qquad\qquad$ 2. $\boldsymbol{\kappa}_{el} \quad = \quad [E_0, c_E, \theta_{E_0}, \nu]^T$

3. $\boldsymbol{\kappa}_\theta \quad = \quad [\alpha_A]^T$ $\qquad\qquad$ 4. $\boldsymbol{\kappa}_{tp} \quad = \quad [K_{tpA}, K_{tpM}, \mu_{MA}, k_\theta]^T$

5. $\boldsymbol{\kappa}_{co} \quad = \quad [\theta^m, \theta^r, \rho_M, \rho_A, A_{c1}, \theta_{MS}]^T$

Table 4.2: Multi-mechanism model for elasticity, visco-plasticity and transformation-induced plasticity with consideration of a phase gradient.

4.4 Numerical implementation on a finite element level

In Section 4.3 we extended the multi-mechanism model of Section 3.3 with a phase gradient term, where the austenite phase fraction is treated as an extra DOF. In comparison to the normal DOFs such as displacement and temperature, this DOF must be defined from user while using a FE-software. Therefore, the numerical implementation on the material level as in Section 3.4 is not sufficient. The model must be implemented on a

finite element level. As in Section 3.4 a dynamic explicit analysis will be used. To this end, the strong forms of equilibrium (4.6) and (4.18) will be derived into weak forms, which will be solved numerically by using the Finite-Element method. The isoparametric concept will be introduced and the finite element residuals will be formulated in matrix form.

4.4.1 Weak formations

The strong forms of equilibrium in a material form and the related boundary conditions for the macro and the micro scale in accordance of the two DOFs $\mathbf{x}$ and z_A are given in Eq.(4.6). The strong form of the another DOF the temperature θ as an additional DOF is given in Eq.(4.18). There are several ways to derive finite element matrix formulations, e.g. the method of virtual displacements, HU-WASHIZU functional and LAGRANGE functional. In this work the method of virtual displacements is used. For construction of weak formulations of Eq.(4.6) and Eq.(4.18) the spaces of compatible displacements $\mathcal{U}$ and phases $\mathcal{Z}$ as well as temperatures $\mathcal{T}$ are introduced as follows:

$$
\begin{aligned}
1. \quad \mathcal{U} &= \{\delta\mathbf{u} = \delta u_i \mathbf{e}_i \quad | \quad \delta u_i \in H^1(\mathcal{B}_0),\ \delta\mathbf{u} = \mathbf{0} \text{ on } \partial\mathcal{B}_0^u\}, \\
2. \quad \mathcal{Z} &= \{\delta z_A \qquad\quad | \quad \delta z_A \in H^1(\mathcal{B}_0)\}, \\
3. \quad \mathcal{T} &= \{\delta\theta \qquad\quad | \quad \delta\theta \in H^1(\mathcal{B}_0),\ \delta\theta = \overline{\theta} \text{ on } \partial\mathcal{B}_0^\theta\},
\end{aligned}
\tag{4.38}
$$

and where $\mathbf{e}_i, i = 1, 2, 3$ are orthogonal unit basis vectors. $\overline{\theta}$ is the prescribed temperature introduced in Eq.(2.35). Next we take a scalar product of Eq.(4.6.1) with a test function $\delta\mathbf{u} \in \mathcal{U}$, integrate over the volume $\mathcal{B}_0$ and impose the traction boundary conditions Eq.(2.35). Furthermore, Eq.(4.6.3) is multiplied with a test function $\delta z_A \in \mathcal{Z}$ and is integrated over the volume $\mathcal{B}_0$ under consideration of Eq.(4.6.4). Moreover, Eq.(4.18) is multiplied with a test function $\delta\theta \in \mathcal{T}$ and is integrated over the volume $\mathcal{B}_0$ under consideration of the boundary conditions Eq.(2.35). After some rearrangements we have the following weak formulations:

$$
\begin{aligned}
1. \quad & G_{\mathbf{u}} := G_{int} - G_{ext} = 0, \\
2. \quad & G_{int} = \int_{\mathcal{B}_0} \delta\mathbf{P} : \mathbf{F} \ dV = \int_{\mathcal{B}_0} \delta\mathbf{E} : \mathbf{S} \ dV \qquad \forall \quad \delta\mathbf{u} \in \mathcal{U}, \\
3. \quad & G_{ext} = \int_{\mathcal{B}_0} \delta\mathbf{u} \cdot \mathbf{f} \ dV + \int_{\partial\mathcal{B}_0^{\mathbf{P}}} \delta\mathbf{u} \cdot \mathbf{t} \ dA \qquad \forall \quad \delta\mathbf{u} \in \mathcal{U}, \\
4. \quad & G_z := \int_{\mathcal{B}_0} \delta z_A (\nabla \cdot \boldsymbol{\xi} + \pi) \ dV = 0 \qquad \forall \quad \delta z_A \in \mathcal{Z}, \\
5. \quad & G_\theta := \int_{\mathcal{B}_0} \delta\theta (\rho_0\, c_d\, \dot{\theta} + \nabla\mathbf{q}_0 - \varphi_{in} - \rho_0 r_\theta) = 0 \quad \forall \quad \delta\theta \in \mathcal{T},
\end{aligned}
\tag{4.39}
$$

where $\mathbf{S}$ is the second Piola-Kirchhoff stress tensor. G_{int} and G_{ext} are the internal and external part of the weak form related to the displacement, respectively. $\mathbf{E}$ is the Green strain tensor introduced in Eq.(A.5). φ_{in} is the inelastic dissipation with

$$
\begin{aligned}
\varphi_{in} &= \overline{\mathbf{M}} : (\bar{\mathbf{L}}_i + \bar{\mathbf{L}}_\theta + \bar{\mathbf{L}}_z) - \underline{Q}\,\dot{\underline{q}} - \underline{Z}_\nabla \dot{\underline{z}} - \boldsymbol{\xi} \cdot \nabla\dot{\underline{z}} \\
&+ \theta\frac{\partial\overline{\mathbf{M}}}{\partial\theta} : \bar{\mathbf{L}}_e + \theta\frac{\partial Q}{\partial\theta}\,\dot{\underline{q}} + \theta\frac{\partial\underline{Z}_\nabla}{\partial\theta}\,\dot{\underline{z}} + \theta\frac{\partial\boldsymbol{\xi}}{\partial\theta} \cdot \nabla\dot{\underline{z}}.
\end{aligned}
\tag{4.40}
$$

Using Eq.(4.11.2), Eq.(4.11.5), Eq.(4.15), Eq.(4.17), Eq.(4.30) and Eq.(4.31), the weak formulation for the phase z_A of Eq.(4.39.4) can be rearranged as

$$\int_{\mathcal{B}_0} \delta z_A (\dot{z}_A - \alpha \nabla^2 z_A - \mu_{MA} (1 - z_A) H(\theta - A_{c1})) dV = 0 \quad \forall \ \delta z_A \in \mathcal{Z} \qquad (4.41)$$

The weak equations for the displacement $\mathbf{u}$, the phase z_A and the temperature θ are

1. $G_{\mathbf{u}} = \int_{\mathcal{B}_0} \delta \mathbf{E} : \mathbf{S} \ dV - \int_{\mathcal{B}_0} \delta \mathbf{u} \cdot \mathbf{f} \ dV - \int_{\partial \mathcal{B}_0^{\mathbf{P}}} \delta \mathbf{u} \cdot \mathbf{t} \ dA = 0 \quad \forall \ \delta \mathbf{u} \in \mathcal{U},$

2. $G_z = \int_{\mathcal{B}_0} \delta z_A (\dot{z}_A - \alpha \nabla^2 z_A - \mu_{MA} (1 - z_A) H(\theta - A_{c1})) dV = 0 \quad \forall \ \delta z_A \in \mathcal{Z},$ (4.42)

3. $G_\theta = \int_{\mathcal{B}_0} \delta \theta (\rho_0 \, c_d \, \dot{\theta} + \nabla \mathbf{q}_0 - \varphi_{in} - \rho_0 r_\theta) = 0 \quad \forall \ \delta \theta \in \mathcal{T}.$

Note, Eq.(4.42.2) only considers the case $\theta > A_{c1}$ of Eq.(4.35). The remaining cases can be calculated analogously.

4.4.2 Discretization

We consider a 2D problem that occupies the 2D-domain $\mathcal{B}_0 \subset \mathcal{E}^2$. A discretization of the domain $\mathcal{B}_0 \approx \mathcal{B}_0^h = \cup_{e=1}^{n_e} \mathcal{B}_0^e$ into n_e quadrilateral elements with nodes $nen = 4$ is given in Figure 4.3. Each element occupies a subdomain $\mathcal{B}_0^e$.
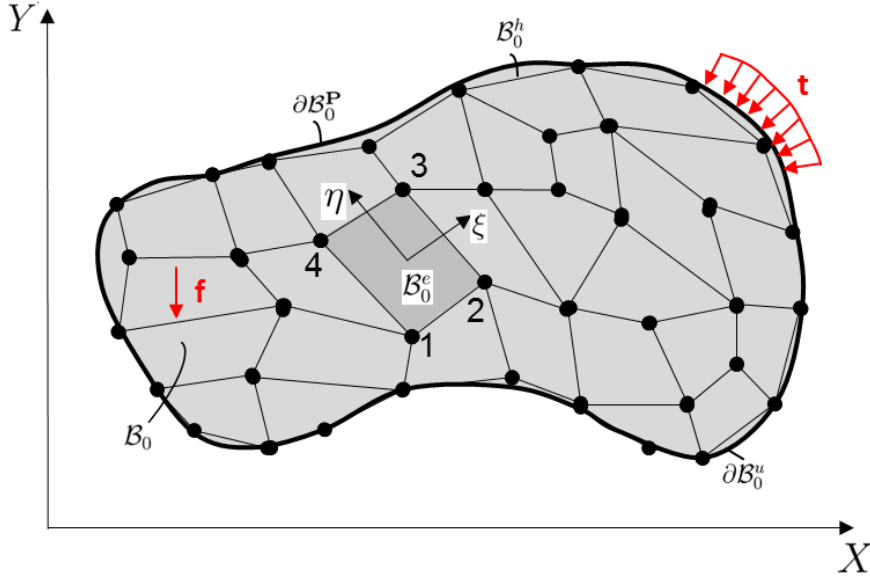
Figure 4.3: Discretization with quadrilateral elements in the reference configuration

In the isoparametric domain $\mathcal{B}_0^{e,\xi}$, a local coordinate system with the coordinates ξ and η is introduced with the properties

$$0 \le \xi, \quad \eta \le 1. \qquad (4.43)$$

A global coordinate system $\underline{X} = [X,\ Y]^T$ in the reference configuration, a global coordinate system $\underline{x} = [x,\ y]^T$ in the current configuration and a local coordinate system $\underline{\xi} = [\xi,\ \eta]^T$ are created. An overview for the transformation between the configurations is given in Figure 4.4.
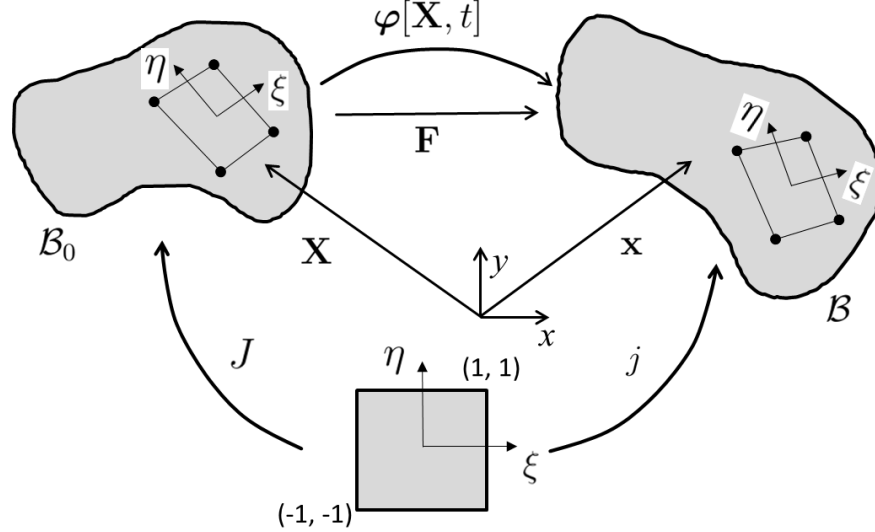
Figure 4.4: Transformations between isoparametric, reference and current domain

The geometry in the reference configuration and the current configuration are obtained as

$$1.\ \underline{X}(\underline{\xi}) = \sum_{i=1}^{nen} N^i(\underline{\xi})\hat{\underline{X}}_i, \quad 2.\ \underline{x} = \sum_{i=1}^{nen} N^i(\underline{\xi})\hat{\underline{x}}_i, \tag{4.44}$$

respectively. Here, $\hat{\underline{X}}_i$ and $\hat{\underline{x}}_i$ denote the coordinates at the node i in the reference and current configuration, respectively. The ansatz functions are denoted by $N^i(\underline{\xi})$. In case of the quadrilateral element with bilinear ansatz functions we have

$$N^i(\underline{\xi}) = \frac{1}{4}(1 + \xi\xi_i)(1 + \eta\eta_i). \tag{4.45}$$

The ansatz function for a node i is denoted by N^i with ξ_i and η_i.

The key idea of the isoparametric concept is to describe the geometry and the degrees of freedom as well as the variables of the elements by using the same ansatz functions. Therefore, the incremental displacement, the virtual displacement, the austenite phase fraction, its virtual term, the temperature and its virtual term read

$$
\begin{aligned}
&1.\ \ \mathbf{u} = \sum_{i=1}^{nen} N^i\hat{\mathbf{u}}_i = \underline{N}\hat{\underline{\mathbf{u}}}, &\qquad &2.\ \ \delta\mathbf{u} = \sum_{i=1}^{nen} N^i\delta\hat{\mathbf{u}}_i = \underline{N}\delta\hat{\underline{\mathbf{u}}}, \\
&3.\ \ z_A = \sum_{i=1}^{nen} N^i\hat{z}_{Ai} = \underline{N}\hat{\underline{z}}_A, &\qquad &4.\ \ \delta z_A = \sum_{i=1}^{nen} N^i\delta\hat{z}_{Ai} = \underline{N}\delta\hat{\underline{z}}_A, \\
&5.\ \ \theta = \sum_{i=1}^{nen} N^i\hat{\theta}_i = \underline{N}\hat{\underline{\theta}}, &\qquad &6.\ \ \delta\theta = \sum_{i=1}^{nen} N^i\delta\hat{\theta}_i = \underline{N}\delta\hat{\underline{\theta}}.
\end{aligned}
\tag{4.46}
$$

As shown in Figure 4.4, the transformation between the isoparametric configuration $\mathcal{B}_0^\xi$ and the reference configuration $\mathcal{B}_0$ can be described with the Jacobian, which is expressed in matrix notation as

$$\underline{J} = \frac{\partial \underline{X}}{\partial \underline{\xi}} = \sum_{i=1}^{nen} \frac{\partial N^i(\underline{\xi})}{\partial \underline{\xi}} \hat{\underline{X}}_i = \begin{bmatrix} \sum_{i=1}^{nen} \frac{\partial N^i}{\partial \xi} \hat{X}_i & \sum_{i=1}^{nen} \frac{\partial N^i}{\partial \xi} \hat{Y}_i \\ \sum_{i=1}^{nen} \frac{\partial N^i}{\partial \eta} \hat{X}_i & \sum_{i=1}^{nen} \frac{\partial N^i}{\partial \eta} \hat{Y}_i \end{bmatrix}. \tag{4.47}$$

The derivatives of the ansatz functions in the reference configuration are

$$\begin{aligned} 1. \quad \frac{\partial \underline{N}(\xi)}{\partial \underline{\xi}} &= \frac{\partial \underline{X}}{\partial \underline{\xi}} \cdot \frac{\partial \underline{N}(\xi)}{\partial \underline{X}} = \underline{J} \cdot \frac{\partial \underline{N}(\xi)}{\partial \underline{X}}, \\ 2. \quad \frac{\partial \underline{N}(\xi)}{\partial \underline{X}} &= \underline{J}^{-1} \cdot \frac{\partial \underline{N}(\xi)}{\partial \underline{\xi}}. \end{aligned} \tag{4.48}$$

The derivatives of the ansatz functions for the current configuration render

$$\frac{\partial \underline{N}(\xi)}{\partial \underline{x}} = \underline{F}^{-T} \cdot \frac{\partial \underline{N}(\xi)}{\partial \underline{X}} = \underline{F}^{-T} \underline{J}^{-1} \cdot \frac{\partial \underline{N}(\xi)}{\partial \underline{\xi}} = \underline{j} \cdot \frac{\partial \underline{N}(\xi)}{\partial \underline{\xi}} \tag{4.49}$$

with

$$\begin{aligned} 1. \quad \underline{F} &= \frac{\partial \underline{x}}{\partial \underline{X}} = \frac{\partial \underline{N}(\xi)}{\partial \underline{X}} \cdot \hat{\underline{x}} = \underline{J}^{-1} \cdot \frac{\partial \underline{N}(\xi)}{\partial \underline{\xi}} \cdot \hat{\underline{x}} \\ 2. \quad \underline{j} &= \underline{F}^{-T} \underline{J}^{-1}. \end{aligned} \tag{4.50}$$

4.4.3 Finite element residuals

In this subsection we will formulate the residual equations Eq.(4.42) into finite element matrix notations. Using the relation (A.5), the tensor term $\delta \mathbf{E}$ is formulated in matrix notation as:

$$\begin{aligned} \delta \underline{E} &= \frac{1}{2} \left(\delta \underline{F}^T \underline{F} + \underline{F}^T \delta \underline{F} \right) \\ &= \frac{1}{2} \left(\delta \hat{\underline{u}} \cdot \frac{\partial \underline{N}(\xi)}{\partial \underline{X}} \underline{F} + \left(\delta \hat{\underline{u}} \cdot \frac{\partial \underline{N}(\xi)}{\partial \underline{X}} \underline{F} \right)^T \right), \end{aligned} \tag{4.51}$$

where

$$\delta \underline{F} = \frac{\partial \underline{N}(\xi)}{\partial \underline{X}} \cdot \delta \hat{\underline{u}}. \tag{4.52}$$

Using Eq.(4.46.2) the relation (4.51) can be rewritten as

$$\delta \underline{E}(\delta \hat{\underline{u}}) = \sum_{i=1}^{nen} \underline{B}_L^i(\underline{\xi}) \delta \hat{\underline{u}}_i = \underline{B}_L \delta \hat{\underline{u}}. \tag{4.53}$$

Here $\underline{B}_L = [\underline{B}_L^1, \underline{B}_L^2, \underline{B}_L^3, \underline{B}_L^4]$ with

$$\underline{B}_L^i = \begin{bmatrix} F_{11}\dfrac{\partial N^i}{\partial X} & F_{21}\dfrac{\partial N^i}{\partial X} \\[2ex] F_{12}\dfrac{\partial N^i}{\partial Y} & F_{22}\dfrac{\partial N^i}{\partial Y} \\[2ex] F_{11}\dfrac{\partial N^i}{\partial Y} + F_{12}\dfrac{\partial N^i}{\partial X} & F_{21}\dfrac{\partial N^i}{\partial Y} + F_{22}\dfrac{\partial N^i}{\partial X} \end{bmatrix} \tag{4.54}$$

Converting the weak form of Eq.(4.42) to matrix notation renders:

1. $\displaystyle\sum_{e=1}^{ne} \int_{\mathcal{B}_0^e} \delta \underline{E}\underline{S} \, dV - \sum_{e=1}^{ne} \int_{\mathcal{B}_0^e} \delta \underline{u}\underline{f} \, dV - \sum_{e=1}^{ne} \int_{\partial\mathcal{B}_0^{\mathrm{Pe}}} \delta\underline{u}\underline{t} \quad dA = 0 \ \forall \ \delta\underline{u},$

2. $\displaystyle\sum_{e=1}^{ne} \int_{\mathcal{B}_0^0} \delta\underline{z}_A(\dot{z}_A - \alpha\nabla^2 z_A - \mu_{MA}\left(1-z_A\right)H(\theta - A_{c1}))dV = 0 \quad \forall \ \delta\underline{z}_A, \tag{4.55}$

3. $\displaystyle\sum_{e=1}^{ne} \int_{\mathcal{B}_0^0} \delta\underline{\theta}(\rho_0\,c_d\,\dot\theta + \nabla\underline{q}_0 - \varphi_{in} - \rho_0 r_\theta)dV = 0 \quad \forall \ \delta\underline{\theta}.$

We separate the time t into n time-steps. Using an explicit forward Euler scheme the time derivation of the phase $\dot{z}_A$ and the temperature θ in (n+1)-th step can be expressed as

$$1.\ \dot{z}_A = \frac{z_A^{n+1} - z_A^n}{\Delta t}, \quad 2.\ \dot\theta = \frac{\theta^{n+1} - \theta^n}{\Delta t}, \tag{4.56}$$

where Δt is the time increment. n+1 refers to the current time step, and n refers to the old time step. Inserting Eq.(4.53) into Eq.(4.55), we obtain the finite element residual equations as follows:

1. $\underline{R}_u \quad = \displaystyle\mathop{\mathbf{A}}_{e=1}^{ne} \int_{\mathcal{B}_0^e} \left(\underline{B}_L^T \underline{S} - \underline{N}^T\mathrm{f}\right) \, dV - \mathop{\mathbf{A}}_{e=1}^{ne} \int_{\partial\mathcal{B}_0^{\mathrm{Pe}}} \underline{N}^T \cdot \underline{t} \, dA = \underline{0},$

2. $\underline{R}_{z_A} \ = \displaystyle\mathop{\mathbf{A}}_{e=1}^{ne} \int_{\mathcal{B}_0^0} \underline{N}^T(\dot{z}_A - \alpha\nabla^2 z_A - \mu_{MA}\left(1-z_A\right)H(\theta - A_{c1}))dV = \underline{0}, \tag{4.57}$

3. $\underline{R}_\theta \quad = \displaystyle\mathop{\mathbf{A}}_{e=1}^{ne} \int_{\mathcal{B}_0^0} \underline{N}^T(\rho_0\,c_d\,\dot\theta + \nabla\underline{q}_0 - \varphi_{in} - \rho_0 r_\theta)dV = \underline{0}.$

Analogously, remaining cases of Eq.(4.35) for the phase transformation can also be calculated. Furthermore, the implementation on material level is very similar to the implementation in Section 3.4 and shall not be discussed here.

4.5 Representative examples

In this section we intend to identify the parameters related to the extensions of the multi-mechanism model and investigate some cutting simulations in order to test the model.

In comparison to Section 3.5.1, the following parameters are new due to the extensions: 1. $\boldsymbol{\kappa}_{pl}$ in Table 4.1 related to hardness dependent material behavior, 2. $F_{\mathcal{H}}$ in Remarks 4.3.2 related to hardness modification, 3. α in Eq.(4.32) and Eq.(4.33). Mechanical tests are investigated under tension, compression and shear with different hardened specimens for identifying hardness dependent plasticity. The remaining parameters $F_{\mathcal{H}}$ and α will be studied and discussed with help of the cutting simulations in subsection 4.5.2.

4.5.1 Mechanical tests for identifying hardness dependent plasticity

Due to the hardness dependence of the new visco-plastic model summarized in Table 4.1, more mechanical tests related hardness dependence are required for identifying the parameters $\boldsymbol{\kappa}_{pl}$ in this table. Under consideration of asymmetric effect, the mechanical tests are performed under tension, compression and shear with different hardened specimens at room temperature and constant strain rate. Production of the specimens and the mechanical testing were done by the company NORDMETALL, Adorf, Germany. Concerning specimen geometry and performance of the experiments we refer to HALLE [33] and MAHNKEN [57].

Notation	Strain rate $\dot{\varepsilon}$ [s^{-1}]	Tension (t) /Compression (c) /Shear (s)	Temperature θ [^{o}C]	Hardness HRC
T53	0.1	Tension	20	53
T57	0.1	Tension	20	57
T60	0.1	Tension	20	60
T62	0.1	Tension	20	62
T64	0.1	Tension	20	64
C53	0.1	Compression	20	53
C57	0.1	Compression	20	57
C60	0.1	Compression	20	60
C62	0.1	Compression	20	62
C64	0.1	Compression	20	64
S53	0.1	Shear	20	53
S57	0.1	Shear	20	57
S60	0.1	Shear	20	60
S62	0.1	Shear	20	62
S64	0.1	Shear	20	64

Table 4.3: Summary of the mechanical tests for hardness dependency

The selected hardness states are 53 HRC, 57 HRC, 60 HRC, 62 HRC and 64 HRC. There are two steps to get the chosen hardness states of the specimens. At first, all

specimens must be pre-treated to fully consist of martensite. Therefore, they are heated up to 830 °C and held at this temperature for 10 minutes such that they fully consist of austenite. After this they are quenched with oil resulting in martensite. In the second step the specimens are tempered with different temperatures to obtain different hardness states (375 °C for 53 HRC, 310 °C for 57 HRC, 270 °C for 60 HRC, 220 °C for 62 HRC and 100 °C for 64 HRC).

After the pre-treatment, quasi-statical investigations are performed with the nomenclature as shown in Table 4.3.
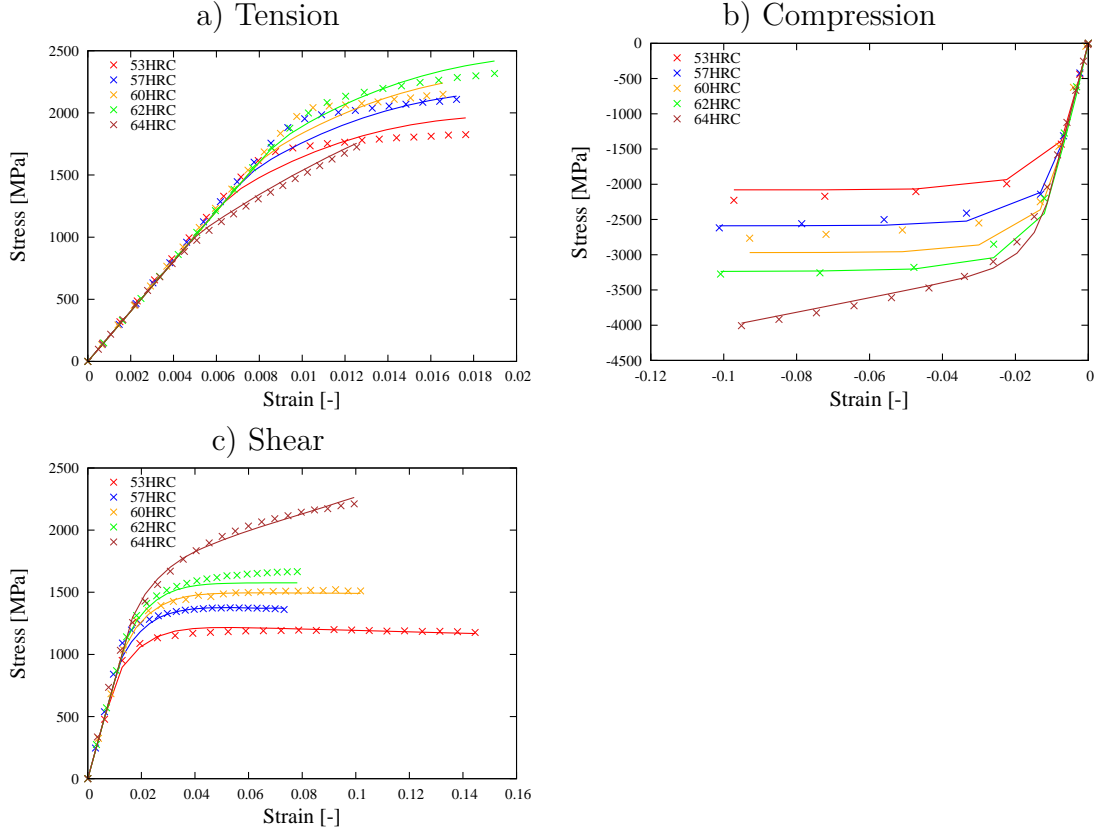
Figure 4.5: Steel AISI 52100: Stress strain curves for different hardened states under a) tension, b) compression and c) shear. Symbols refer to experiment, solid lines to simulation.

Since the hardness dependency is an extra effect, the experimental data of the thermal-mechanical tests in Section 3.5.1 for the hardness 62 HRC is also valid for the new model, if and only if F and G in Eq.(4.25) equal zero

$$1.\ F(\mathcal{H}) = F_1 \cdot 62\ \text{HRC} - F_2 = 0, \quad 2.\ G(\mathcal{H}) = G_1 \cdot 62\ \text{HRC} - G_2 = 0. \qquad (4.58)$$

Once the hardness changes, F and G are non-zero, and the hardness dependency is active.

In this work we shall only show the results of parameter identification related to the hardness dependency. Concerning the different behavior in tension, compression

and shear, $S = 3$ is set for the constitutive equations in Table 4.1. Using a least-squares functional as an identification criterion, the parameters of $\boldsymbol{\kappa}_{pl}$ are identified and summarized in Table 4.4. For more details on the functional and the procedure we refer to [53, 54].

$\boldsymbol{\kappa}_{pl}:$	$F_{11} \left[\frac{\text{MPa}}{\text{HRC}}\right]$	$F_{12} \left[\frac{\text{MPa}}{\text{HRC}}\right]$	$F_{13} \left[\frac{\text{MPa}}{\text{HRC}}\right]$	$G_{11} \left[\frac{\text{MPa}}{\text{HRC}}\right]$	$G_{12} \left[\frac{\text{MPa}}{\text{HRC}}\right]$	$G_{13} \left[\frac{\text{MPa}}{\text{HRC}}\right]$
$\mathcal{H} \geq 62$:	-3.43E+02	2.04E+01	1.27E+02	2.73E+04	4.48E+03	6.707E+03
$\mathcal{H} < 62$:	3.78E+01	1.049E+02	6.43E+01	4.48E+02	4.012E+00	2.504E+02
	F_{21} [MPa]	F_{22} [MPa]	F_{23} [MPa]	G_{21} [MPa]	G_{22} [MPa]	G_{23} [MPa]
$\mathcal{H} \geq 62$:	-2.126E+04	1.265E+03	7.87E+03	1.69E+06	2.77E+05	4.158E+05
$\mathcal{H} < 62$:	2.34E+03	6.503E+03	3.987E+03	2.778E+04	2.487E+02	1.55E+04
	Y_{01} [MPa]	Y_{02} [MPa]	Y_{03} [MPa]	H_{11} [MPa]	H_{12} [MPa]	H_{13} [MPa]
	1.475E+03	2.0953E+03	1.7066E+03	1.4875E+05	1.4875E+05	1.4875E+05
	H_{21} [MPa]	H_{22} [MPa]	H_{23} [MPa]	c_1 [−]	c_2 [−]	c_3 [−]
	1.97E-02	1.97E-02	1.97E-02	2.61E+02	2.61E+02	2.61E+02
	C_{11} [−]	C_{12} [−]	C_{13} [−]	C_{21} [−]	C_{22} [−]	C_{23} [−]
	2.91E-02	2.55E-02	2.39E-02	1.1E-03	8.1E-04	5.1E-04
	$\dot{\varepsilon}_{01}$ [−]	$\dot{\varepsilon}_{02}$ [−]	$\dot{\varepsilon}_{03}$ [−]	m_1 [−]	m_2 [−]	m_3 [−]
	1.0E-05	1.0E-05	1.0E-05	7.23E-01	1.1E+00	0.7E-01

Table 4.4: Material parameters related to visco-plasticity concerning hardness dependency for steel AISI 52100

The resulting stress strain curves of the experiments and simulations are illustrated in Figure 4.5: a) tension, b) compression and c) shear. The symbols show the experimental data. The solid lines refer to simulated data. In all diagrams, good agreements between experiment and simulation is obtained. The results show an identical elastic behavior and different inelastic behavior for the different hardened states in tension and compression as well as in shear. Generally, the harder the specimen, the higher the stress level, except for the hardened state 64 HRC in tension. Since the hardened state 64 HRC is very brittle such that the specimen starts to fail already at elastic loading only with very small plastic deformation for pure tension. Also under compression and shear the material behavior of 64 HRC does not match with other hardened states as the stress level is higher. To this end, a distinction of cases for the parameter identification is made, where the hardened state 62 HRC is treated as the threshold. Therefore, the results for the case $\mathcal{H} \geq 62$ HRC and $\mathcal{H} < 62$ HRC are different (see Table 4.4).

4.5.2 Simulation of a cutting process

Due to the extension and the numerical aspects in Section 4.4, the new model can be implemented as a user-defined element subroutine for explicit calculations (VUEL) and linked to ABAQUS v6.14. Since plotting of user elements is not supported in ABAQUS/CAE [1], additional efforts must be done for visualisations.

Visualisation of VUEL with ABAQUS/Viewer

```
** Section: Section-3
*Solid Section, elset=_PickedSet64, material=MATSPANU
,
*User Element, Nodes=4, Type=VU100, Properties=104, Coordinates=2, Variables=200
 1, 2, 8, 11
*Element, Type=VU100, Elset=VUTRUSS
10001,    1,    9,   491,   244
10002,    9,   10,   492,   491
10003,   10,   11,   493,   492
10004,   11,   12,   494,   493
......
```

Figure 4.6: Definition of user elements in ABAQUS Input-Data

In ABAQUS user elements can be defined in the Input-Data as shown in Figure 4.6. ABAQUS provides a user interface to define nodes of the elements as well as properties, the DOFs, the coordinates and the state variables (SDV) of the nodes. As in Chapter 3 we consider a 2D-problem, thus we have two displacements noted as DOF1 and DOF2. The DOFs 8 and 11 represent the austenite phase fraction and the temperature, respectively. Overall, there are four DOFs. Furthermore, the user has to define the elements e.g. 10001, 10002, 10003... for calculations. As mentioned above, plotting of user elements is not supported in ABAQUS/CAE [1]. This problem can be solved in two steps. Firstly, the alternative standard elements, a sort of dummy elements from the ABAQUS element library, must be used. The topology of the dummy elements and the user elements must be as similar as possible. In this case we chose a 4-node plane strain thermally coupled quadrilateral element (CPE4RT). Although the dummy elements have the same nodes as the user elements, they must be numbered differently as the user elements, e.g. 1, 2, 3... instead of 10001, 10002, 10003.... Their boundary conditions can be defined in a standard way. They should have no resistance to the deformation and therefore are defined to be elastic with a very small Young's modulus e.g. 1.E-20 MPa. After these settings the user elements will have the same boundary conditions as the dummy elements and the deformation is only dependent on the material behavior of the user elements. Secondly, we have to extract the result data of the integration points of the user elements. This can be fulfilled by defining write commands for the variables in the user-subroutine. Once the calculation is running, the result data are saved. As soon as the calculation is completed, these data can be transferred to the result database (ODB) of the dummy elements. The total visualisation process is shown in Figure 4.7.
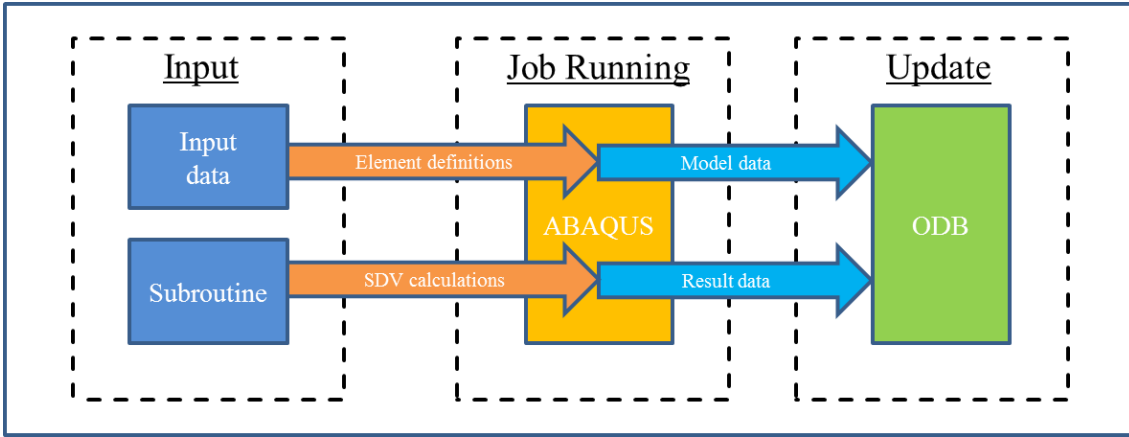
Figure 4.7: Visualisation process of user elements

Simulation results

In this section some cutting simulations are performed to test our model related to the extensions made in this chapter. For simplicity, the geometry, the finite-element discretization and the boundary conditions are chosen as in Figure 3.12 for the original MMM. The tool is treated as a rigid body. The workpiece is defined 500 μm long and 400 μm high with a cutting depth $d = 100$ μm. The initial conditions assume room temperature, and for cooling a conventional temperature condition is applied over the surfaces of the workpiece. For visualisation of the workpiece with ABAQUS/Viewer a 4-node plane strain thermally coupled quadrilateral element (CPE4RT) is selected as the dummy element. The tool is defined in a standard way and uses the element type CPE3T, a 3-node plane strain thermally coupled triangle element.

The extended material model of Section 4.3 is completed with the parameter identification in Section 4.5.1 and applied to the workpiece. For the separation layer we assign the same failure criterion $e_v \leq \mathrm{e}_v^f$ (e_v^f is a constant) as in Section 3.5.2. Furthermore, the cutting speed $v = 3.6$ m/s and the friction between the workpiece and the tool $f = 1.0$ are used for the simulations in this section. Concerning the extensions, the model testing concentrates on the following characteristics:

1. Influence of hardness,

2. Influence of the phase gradient term,

3. Hardness modification due to the white layer formation.

Influence of hardness: In order to study the influence of hardness, two simulations with $\mathcal{H}_{init} = 62$ HRC and $\mathcal{H}_{init} = 59$ HRC are performed, where $\mathcal{H}_{init}$ is the initial hardness state of the workpiece and introduced in Eq.(4.28). Figure 4.8 shows the von-Mises stress of both simulations at time instant $1.14 \cdot 10^{-6}$ s, $2.584 \cdot 10^{-5}$ s, $5.054 \cdot 10^{-5}$ s and $7.6 \cdot 10^{-5}$ s. In comparison, both simulations have nearly the same continuous chips. The stresses concentrate on the cutting zone as always. The maximal value of the von-Mises

stress for $\mathcal{H}_{init} = 62$ is about 3700 MPa, which is about 400 MPa higher than that for $\mathcal{H}_{init} = 59$. Furthermore, the temperature θ and the stress mode factor ξ (Eq.(3.35.1)) are also compared for both simulations at the same time instances as for the von-Mises stress in Figure 4.9 and 4.10, respectively. As can be seen, the maximal temperature for $\mathcal{H}_{init} = 62$ HRC is 850 °C and about 50 °C higher than that for $\mathcal{H}_{init} = 59$ HRC. The contours of the stress mode factor show no difference between both simulations because of their same chip formations.

Influence of the phase gradient term: According to Eq.(4.32) and Eq.(4.33) the gradient term is multiplied by the parameter α, which determines the proportion of the gradient term. In this section we intend to study the influence of the gradient term by performing cutting simulations with variation of the parameter α, where $\mathcal{H}_{init} = 62$ HRC. Figure 4.11 shows the contours of the austenite phase fraction z_A with $\alpha = 0$ μm^2, $\alpha = 1$ μm^2 and $\alpha = 10$ μm^2, respectively. For all simulations austenitization starts at the time point t $= 8.36 \cdot 10^{-6}$ s and occurs mainly on cutting chips due to the temperature distribution as shown in the left column of Figure 4.9. It can be seen, that the maximal value of the austenite for the simulation with smaller α is higher than the one with higher α. However, the austenite for larger α is more diffused. The differences can also be seen in Figure 4.12, which shows the gradient of austenite ∇z_A in horizontal and vertical directions. Furthermore, Figure 4.13 shows the newly formed martensite for the simulations. As can be seen, more new martensite z_M^n (Eq.(3.95)) is formed for the one with higher α than the one with smaller α. The parameter α has a strong influence on the white layer formation. Due to the extension with the gradient term, phase transformations are not only dependent on the temperature but also on the interface energy. Concerning the influence of the extended gradient term we comment on future challenges regarding its identification in the summary in Section 5.2.

Hardness modification due to the white layer formation: As proposed in Section 4.3.2, Eq.(4.28) describes the hardness modification due to the white layer formation. According to this equation the white layer can be induced only if the temperature of a cutting area is higher than the austenitization start temperature and the current temperature is lower than the martensite start temperature. According to the new martensite formation as well as the white layer formation in Figure 4.13, hardness is changed and shown in Figure 4.14. In order to study the influence of the parameter $F_{\mathcal{H}}$ on the hardness modification, different values are used for the simulations, e.g. 2.22, 2.52, 3.02 and 3.52. Note, for simplicity α is selected as $\alpha = 0$ μm^2 for all simulations. It is shown that all hardness modifications have the same contour as the white layer in Figure 4.13. The higher value of $F_{\mathcal{H}}$, the higher the hardness. The maximal hardness with $F_{\mathcal{H}} = 3.52$ is about 63.4 HRC. According to this effect, experimental tests shall be investigated to determine the value of $F_{\mathcal{H}}$. A further discussion will be given in Section 4.6.

$\mathcal{H}_{init} = 62$ HRC $\qquad$ $\mathcal{H}_{init} = 59$ HRC

$t = 1.14 \cdot 10^{-6}$ s

$t = 2.584 \cdot 10^{-5}$ s

$t = 5.054 \cdot 10^{-5}$ s

$t = 7.6 \cdot 10^{-5}$ s
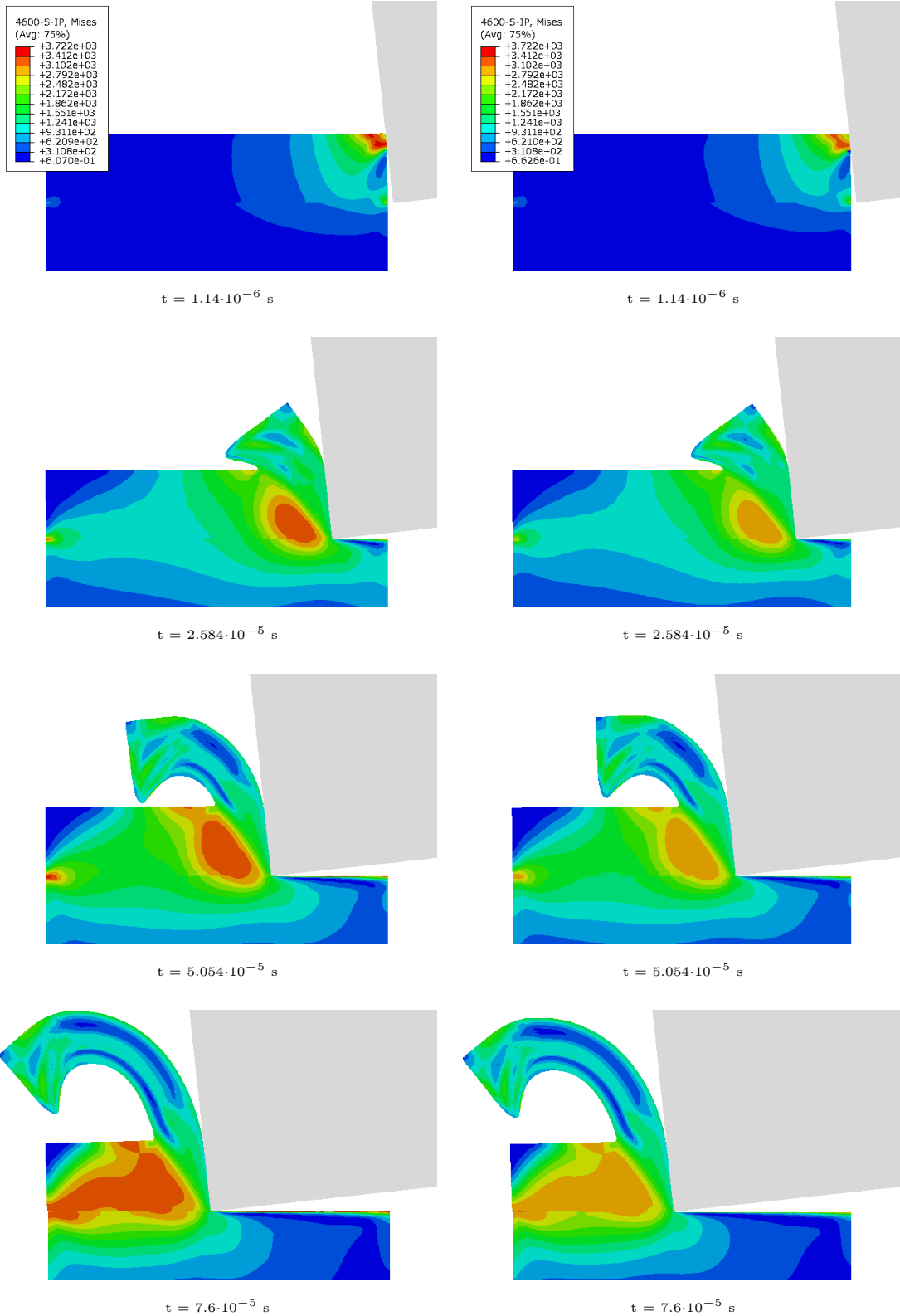
Figure 4.8: Cutting simulation: Contours of von-Mises stress for different initial hardness states

Figure 4.9: Cutting simulation: Contours of temperature for different initial hardness states

$\mathcal{H}_{init} = 62$ HRC $\qquad\qquad\qquad\qquad$ $\mathcal{H}_{init} = 59$ HRC

t = $1.14\cdot10^{-6}$ s $\qquad\qquad\qquad\qquad\qquad$ t = $1.14\cdot10^{-6}$ s

t = $2.584\cdot10^{-5}$ s $\qquad\qquad\qquad\qquad\qquad$ t = $2.584\cdot10^{-5}$ s

t = $5.054\cdot10^{-5}$ s $\qquad\qquad\qquad\qquad\qquad$ t = $5.054\cdot10^{-5}$ s
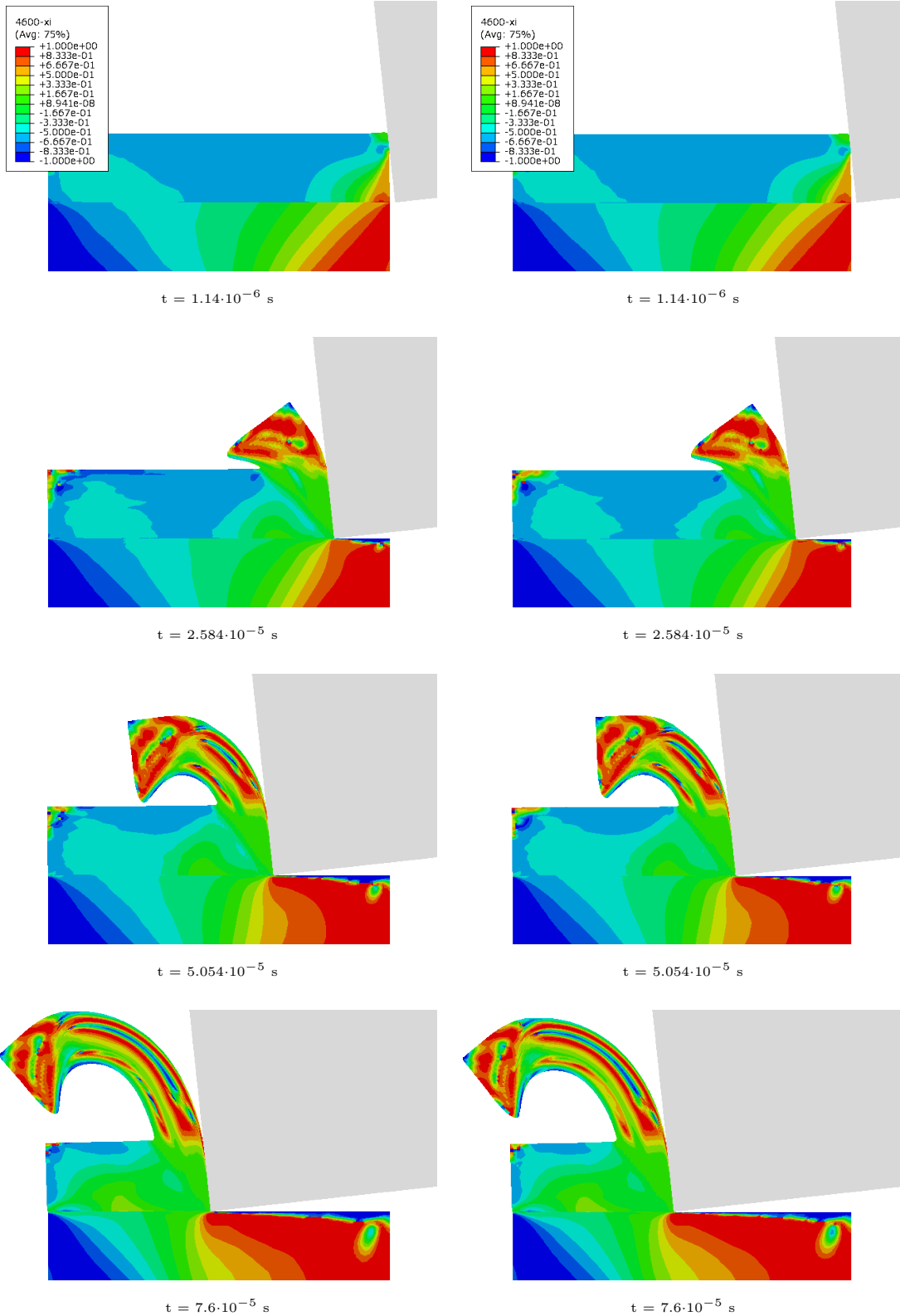
t = $7.6\cdot10^{-5}$ s $\qquad\qquad\qquad\qquad\qquad$ t = $7.6\cdot10^{-5}$ s

Figure 4.10: Cutting simulation: Contours of stress mode factor ξ for different initial hardness states

$\alpha = 0\ \mu\mathrm{m}^2$ $\alpha = 1\ \mu\mathrm{m}^2$ $\alpha = 10\ \mu\mathrm{m}^2$

$t = 8.36 \cdot 10^{-6}$ s $t = 8.36 \cdot 10^{-6}$ s $t = 8.36 \cdot 10^{-6}$ s

$t = 5.054 \cdot 10^{-5}$ s $t = 5.054 \cdot 10^{-5}$ s $t = 5.054 \cdot 10^{-5}$ s

$t = 7.6 \cdot 10^{-5}$ s $t = 7.6 \cdot 10^{-5}$ s $t = 7.6 \cdot 10^{-5}$ s
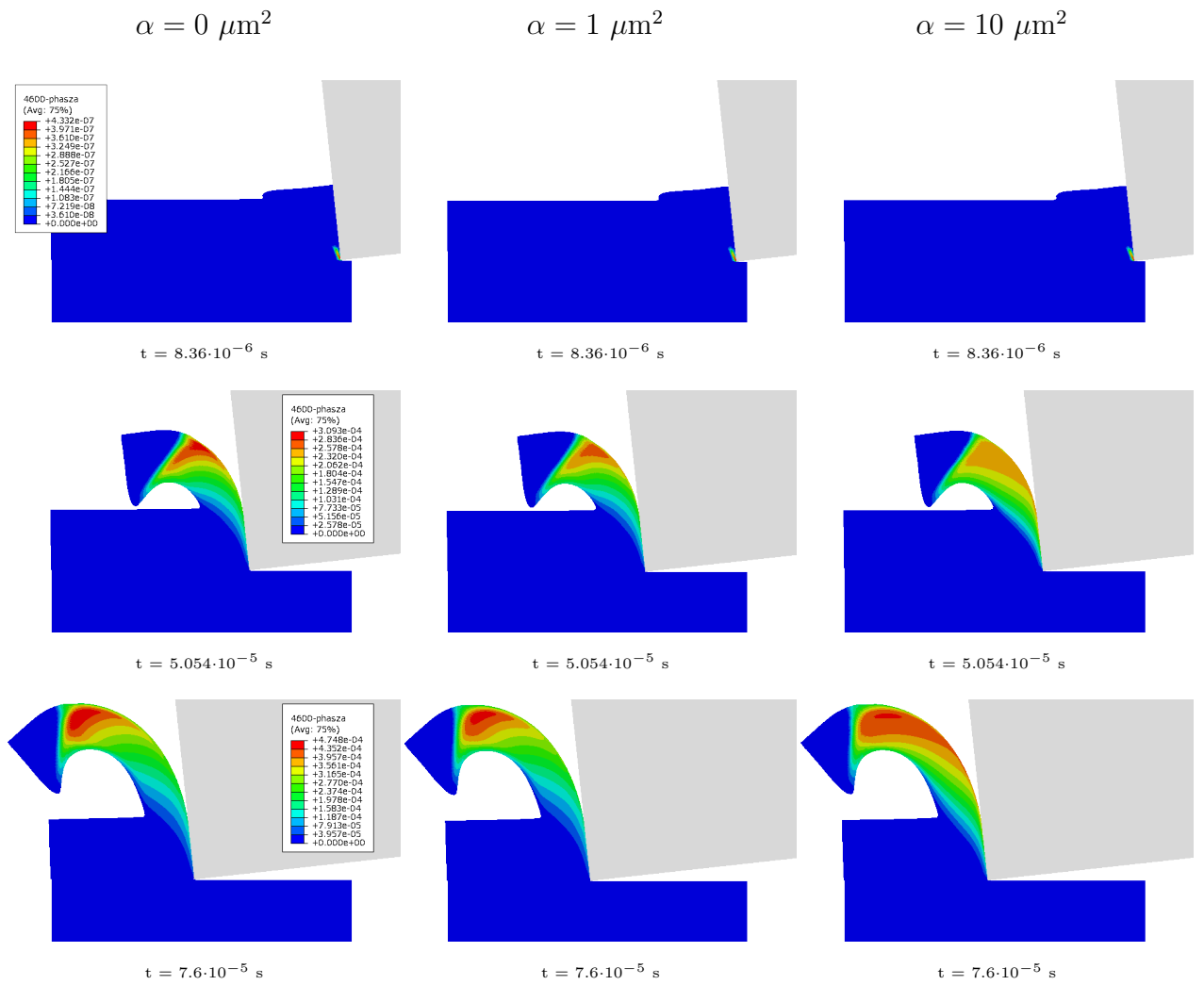
Figure 4.11: Cutting simulation: Contours of austenite z_A for different α

$\alpha = 0\ \mu\mathrm{m}^2$ $\qquad\qquad\qquad$ $\alpha = 1\ \mu\mathrm{m}^2$ $\qquad\qquad\qquad$ $\alpha = 10\ \mu\mathrm{m}^2$

∇z_A in horizontal direction
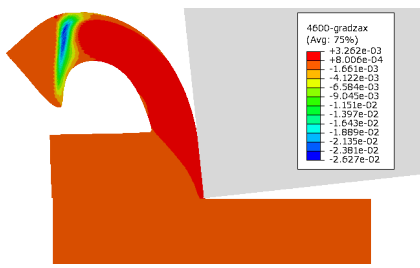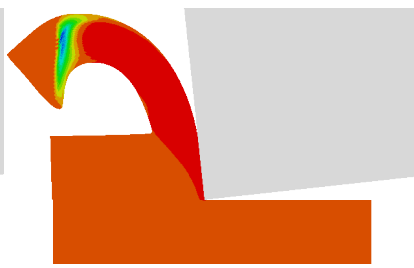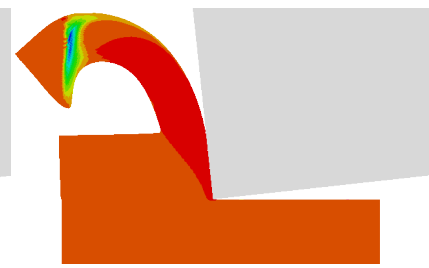
∇z_A in vertical direction
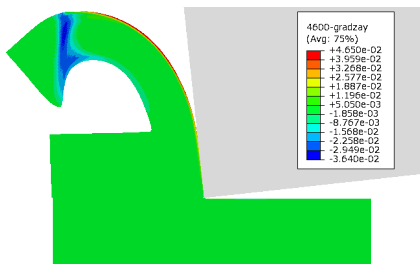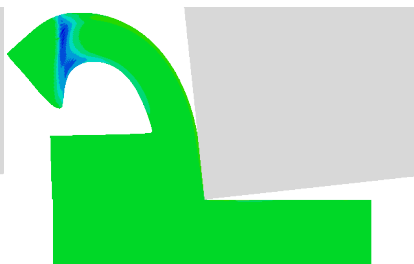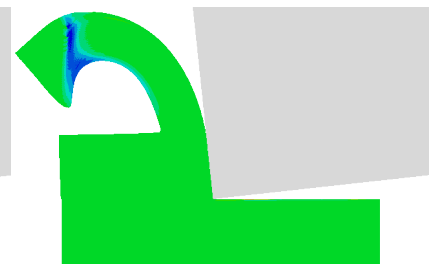
Figure 4.12: Cutting simulation: Contours of ∇z_A for different α
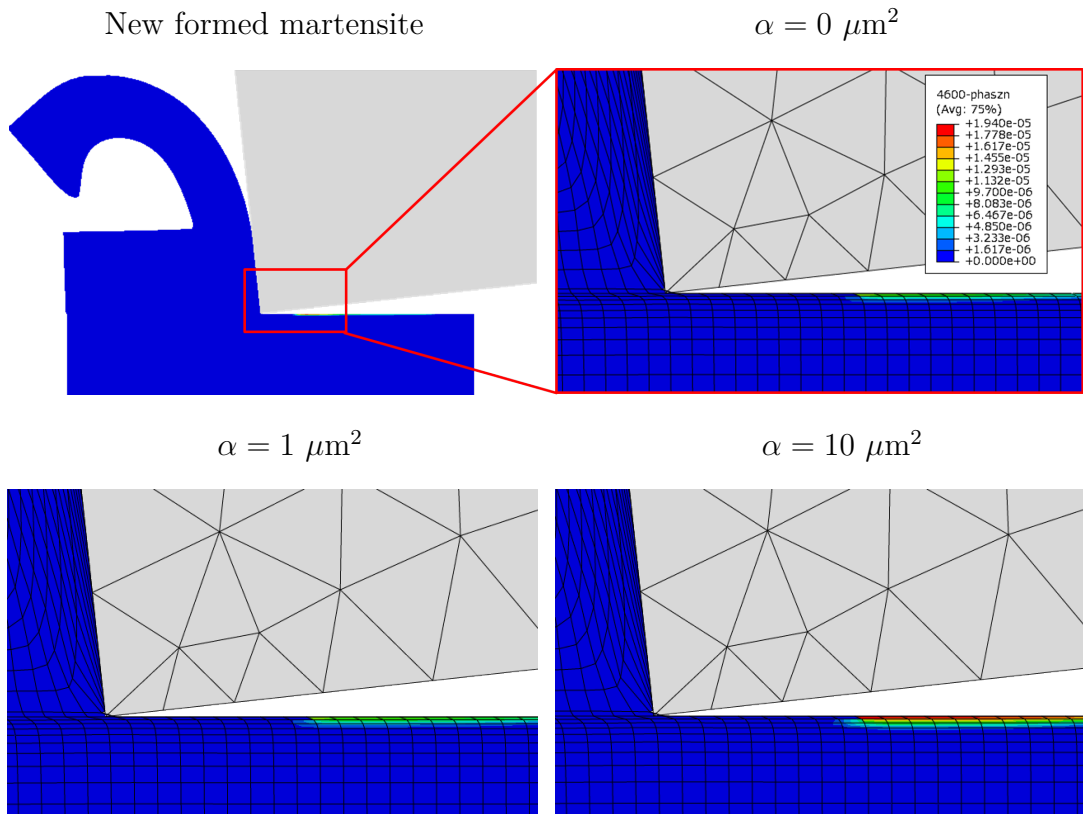
Figure 4.13: Cutting simulation: Contours of new martensite z_M^n for different α at $t = 7.6 \cdot 10^{-5}$ s
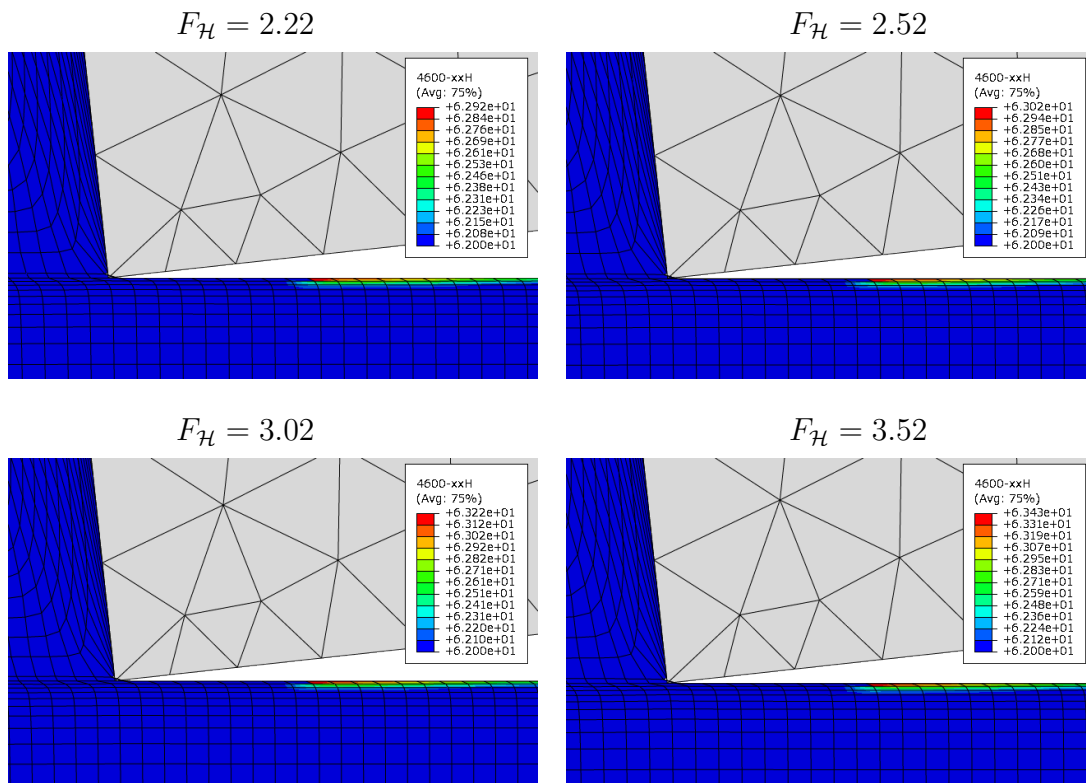
Figure 4.14: Cutting simulation: Contours of hardness modification for different $F_{\mathcal{H}}$ at $t = 7.6 \cdot 10^{-5}$ s

4.6 Summary

Based on the concept of generalized stresses in FOREST *et al.* [27], we extended the multi-mechanism model developed in Chapter 3 with a phase gradient term. To this end, the austenite phase fraction was treated as an extra DOF and its first gradient was involved. Furthermore, the model was extended to take asymmetric hardness dependency and hardness modification into account. To consider the asymmetric hardness dependency, a hardness-dependent function was firstly extended with the concept of weighting functions taking the asymmetric effect into account and then integrated into the yield function (3.30). The hardness modification due to white layer formation was considered with a linear function, which is dependent on austenitization, martensitic retransformation and maximal temperature of the total cutting process. The bulk model was formulated within a thermodynamic framework at large strains and proved to be thermodynamically consistent. The model was implemented on an element level. Furthermore, the parameters related to the asymmetric hardness dependency were identified by comparing simulated data to experimental data. The used mechanical tests were performed with AISI 51200 in different hardened states. Finally, we showed a simulation strategy about the visualisation for user-defined element in ABAQUS and some cutting simulations for testing our new model. The hardness of the material has a significant influence on the stress. The higher the hardness, the higher the stress and the temperature. The extended phase gradient term showed a strong influence on the phase transformation, which is controlled by the parameter α of Eq.(4.32) and Eq.(4.33). The simulation showed also hardness modifications due to the white layer formations, and its level is controlled by the parameter $F_{\mathcal{H}}$ in Section 5.2.

Chapter 5

Summary and Outlook

5.1 Summary

In this dissertation we developed a multi-mechanism model and extended with a phase gradient term based on the concept of generalized stresses. Both models were formulated within a thermodynamic framework at large strains and proved to be thermodynamically consistent. The following effects and aspects are considered in the model: 1. Asymmetric visco-plasticity, 2. phase transformation, 3. TRIP for austenitization and martensitic transformation, 4. Huh-Kang strain rate form, 5. Phase gradient term, 6. Asymmetric hardness dependency, 7. Hardness modification due to white layer formation. Numerical implementations were given on the material level as well as on the element level. Material parameters were identified by using mechanical tests and dilatormeter tests. Mechanical tests were investigated with different strain rates and different temperatures to identify the effects 1 and 4. The effect 6 is identified by investigating further mechanical tests using specimens with different hardness. Dilatormeter tests were used for identifying the effect 2 and 3. Furthermore, cutting simulations were investigated for testing the models according to these effects and studying the influence of the effects 5 and 7.

5.2 Outlook

Concerning further extensions, the model should consider microscopically based observations. As mentioned in TJAHJANTO *et al.* [77] and IWAMOTO *et al.* [41] this would enable to consider the effect of anisotropy due to crystallographic orientations and in this way would provide a detailed insight into the influence of the microstructure on the overall response.

A more extensive data basis is required in future to verify the model presented in a broader sense and to allow to validate modified approaches of modeling phase transformations and TRIP. Moreover, on the numerical side, an adaptive strategy taking strong mesh distortions during a cutting process into account is an area of future research work.

So far, the parameter $F_{\mathcal{H}}$ related to the hardness modification is still unknown. In Section 4.5.2 we found that the greater $F_{\mathcal{H}}$, the harder is the white layer. In order to determine the value of $F_{\mathcal{H}}$, some cutting tests must be investigated under the same

conditions as the simulations. The simulated and the experimental results shall be compared.

Furthermore, an interesting challenge is the identification of the gradient term and the related parameter α on the basis of experiments. The studied material AISI52100 has a carbon content from 0.93 to 1.05% as shown in Table 3.3, which leads to a stabilisation of austenit after the cooling in a martensite-austenite-martensite transformation during a cutting process. The quantities and space distribution of the rest austenite can be measured by using Electron Backscatter Diffraction (EBSD). According to this aspect the parameter α can be identified.

Appendix

A: Basic concepts of tensor calculus on manifolds with application to multiplicative plasticity

A1: Metric tensors and tensor invariants

An intermediate configuration $\bar{\mathcal{B}}$ in addition to a reference configuration $\mathcal{B}_0$ and a actual configuration $\mathcal{B}$ are introduced. The three associated tangent spaces $T\mathcal{B}_0$, $T\mathcal{B}$ and $T\bar{\mathcal{B}}$ are equipped with co-variant Riemannian metric tensors $\mathbf{G}^\flat$, $\mathbf{g}^\flat$, $\overline{\mathbf{G}}^\flat$, respectively, and analogously the associated dual spaces $T\mathcal{B}^*$, $T\mathcal{B}*$ and $T\bar{\mathcal{B}}^*$ with contra-variant Riemannian metric tensors $\mathbf{G}^\sharp = (\mathbf{G}^\flat)^{-1}$, $\mathbf{g}^\sharp = (\mathbf{g}^\flat)^{-1}$, $\overline{\mathbf{G}}^\sharp = (\overline{\mathbf{G}}^\flat)^{-1}$, respectively, see e.g. MARSDEN & HUGHES (1993), GIESSEN & KOLLMANN (1996). The above tensor objects can be used to define invariants of second order tensors. E.g. we define all three *basic invariants* of a mixed-variant second order tensor $\bar{\mathbf{A}}' = \bar{A}_i{}^j \bar{\mathbf{G}}^i \otimes \bar{\mathbf{G}}_j$, related to the intermediate configuration as follows:

$$^{\bar{A}'}I_i \quad := \quad \frac{1}{i}\bar{\mathbf{1}}^\backprime : \left(\bar{\mathbf{A}}'\right)^i = \frac{1}{i}\bar{\mathbf{1}}' : \left(\bar{\mathbf{A}}^\backprime\right)^i = \frac{1}{i}\overline{\mathbf{G}}^\sharp : \left(\bar{\mathbf{A}}' \cdot \overline{\mathbf{G}}^\flat\right)^i, \quad i = 1,2,3. \quad \text{(A.1)}$$

Here $\bar{\mathbf{A}}^\backprime = \mathbf{G}^\sharp \cdot \bar{\mathbf{A}}' \cdot \mathbf{G}^\flat$ and $\bar{\mathbf{1}}^\backprime = \bar{\mathbf{G}}_i \otimes \bar{\mathbf{G}}^i = (\bar{\mathbf{1}}')^t$ is a (mixed-variant) second order unit tensor with basis vectors $\bar{\mathbf{G}}_i$ and $\bar{\mathbf{G}}^i$. In this respect Eq(A.1) represents the invariants as dual pairings of mixed-variant tensors, which by use of $\bar{\mathbf{1}}^\backprime = \overline{\mathbf{G}}^\flat \cdot \overline{\mathbf{G}}^\sharp$ can also be written as dual pairings of co-variant and contra-variant tensors. Without going into details we remark that in complete analogy to the relations (A.1) invariants can be defined relative to the reference configuration and the spatial configuration, respectively. To this end the (mixed-variant) second order unit tensors $\mathbf{1}^\backprime = \mathbf{G}_i \otimes \mathbf{G}^i = (\mathbf{1}')^t$ and $\boldsymbol{\imath}^\backprime = \mathbf{g}_i \otimes \mathbf{g}^i = (\boldsymbol{\imath}')^t$, respectively, are introduced.

A2: Stretch tensors

Several stretch measures can be constructed within the framework of multiplicative plasticity, see e.g. HAUPT [34]. In this work specific attention is directed to the following quantities:

$$
\begin{aligned}
1. \quad & \mathbf{C}_i^{-1} &:=& \quad ^*\Phi_i^\sharp[\overline{\mathbf{G}}^\sharp] &=& \quad \mathbf{F}_i^{-1} \cdot \overline{\mathbf{G}}^\sharp \cdot \mathbf{F}_i^{-t} &=& \quad \mathbf{F}^{-1} \cdot \mathbf{b}_e \cdot \mathbf{F}^{-t} &=& \quad ^*\Phi^\sharp[\mathbf{b}_e] \\
2. \quad & \mathbf{b}_e &:=& \quad _*\Phi_e^\sharp[\overline{\mathbf{G}}^\sharp] &=& \quad \mathbf{F}_e \cdot \overline{\mathbf{G}}^\sharp \cdot \mathbf{F}_e^t &=& \quad \mathbf{F} \cdot \mathbf{C}_i^{-1} \cdot \mathbf{F}^t &=& \quad _*\Phi^\sharp[\mathbf{C}_i^{-1}].
\end{aligned}
\quad \text{(A.2)}
$$

Here the operators $^*\Phi_i^\sharp$, $^*\Phi^\sharp$, $_*\Phi_e^\sharp$, $_*\Phi^\sharp$ denote inelastic pull-back, full pull-back, elastic push-forward, and full push-forward operations of contra-variant tensor objects, respectively. These operations can be regarded as extensions to the standard pull-back and push-forward operations, described e.g. in MARSDEN & HUGHES [61] or SIMO & HUGHES [74]. An extended survey is given e.g. in MAHNKEN [52]. Furthermore, in Eq.(A.2.1) $\mathbf{C}_i^{-1}$ is the inverse inelastic right Cauchy–Green tensor and $\mathbf{b}_e$ is the elastic left Cauchy–Green tensor. Upon replacing the contra-variant metric tensor $\overline{\mathbf{G}}^\sharp$ by the covariant right elastic Cauchy-Green tensor

$$\overline{\mathbf{C}}_e = \mathbf{F}_e^t \cdot \mathbf{g}^\flat \cdot \mathbf{F}_e, \tag{A.3}$$

the relations (A.2) are written analogously as

1. $\mathbf{C} \; := \; ^*\Phi_i^\flat[\overline{\mathbf{C}}_e] \;\; = \;\; \mathbf{F}_i^t \cdot \overline{\mathbf{C}}_e \cdot \mathbf{F}_i \;\;\; = \;\; \mathbf{F}^t \cdot \mathbf{g}^\sharp \cdot \mathbf{F} \;\;\; = \;\; ^*\Phi^\flat[\mathbf{g}^\sharp]$
2. $\mathbf{g}^\flat \; := \; _*\Phi_e^\flat[\overline{\mathbf{C}}_e] \;\; = \;\; \mathbf{F}_e^{-t} \cdot \overline{\mathbf{C}}_e \cdot \mathbf{F}_e^{-1} \;\; = \;\; \mathbf{F}^{-t} \cdot \mathbf{C} \cdot \mathbf{F}^{-1} \;\; = \;\; _*\Phi^\flat[\mathbf{C}].$ $\tag{A.4}$

Here the operators $^*\Phi_i^\flat$, $^*\Phi^\flat$, $_*\Phi_e^\flat$, $_*\Phi^\flat$ represent plastic pull-back, full pull-back, elastic push-forward and full push-forward operations of co-variant tensor objects, respectively. Note, that $\mathbf{C}_i^{-1}$ is related to the reference configuration whereas $\overline{\mathbf{C}}_e$ is related to the intermediate configuration. The right Cauchy-Green tensor $\mathbf{C}$ renders the Green strain tensor

$$\mathbf{E} = \frac{1}{2}(\mathbf{F}^t\mathbf{F} - \mathbf{1}) = \frac{1}{2}(\mathbf{C} - \mathbf{1}) \tag{A.5}$$

with the property $\mathbf{F} = \mathbf{1} \implies \mathbf{E} = \mathbf{0}$. Next, associated to $\overline{\mathbf{C}}_e$ and $\mathbf{b}_e$ the multiplicative splits

1. $\mathbf{b}_e = J_e^{2/3}\hat{\mathbf{b}}_e$, 2. $\overline{\mathbf{C}}_e = J_e^{2/3}\hat{\mathbf{C}}_e$, where
3. $J_e = \left(\det[\overline{\mathbf{C}}_e \cdot \overline{\mathbf{G}}^\sharp]\right)^{1/2} = \left(\det[\mathbf{g}^\sharp \cdot \mathbf{b}_e]\right)^{1/2}$ $\tag{A.6}$

are introduced, such that $\hat{\mathbf{C}}_e, \hat{\mathbf{b}}_e$ and J_e represent the isochoric and volumetric part of the elastic deformation, respectively. Note, that the metric tensors $\overline{\mathbf{G}}^\sharp$ and $\mathbf{g}^\sharp$ are introduced in the above definitions for the determinants, thus allowing directly for unambiguous transformations between different configurations.

A3: Velocity gradients

Velocity gradients can be distinguished with respect to different configurations, see e.g. MIEHE (1994). We start from the well known quantity

$$1. \;\; \mathbf{l} = \nabla\mathbf{v} = \dot{\mathbf{F}} \cdot \mathbf{F}^{-1} \;\;\;\; \implies \;\;\;\; 2. \;\; \mathbf{d} = \text{sym}[\mathbf{g}^\flat \cdot \mathbf{l}], \tag{A.7}$$

where the time derivative $\mathbf{v} = \dot{\mathbf{u}}$ of the displacement $\mathbf{u}$ defines the velocity. Note that $\mathbf{l} = l^i{}_j\mathbf{g}_i \otimes \mathbf{g}^j$ is a mixed variant tensor. An elastic pull-back renders

$$\bar{\mathbf{L}} = {}^*\Phi_e^\backslash[\mathbf{l}] = \mathbf{F}_e^{-1} \cdot \mathbf{l} \cdot \mathbf{F}_e. \tag{A.8}$$

We note, that contrary to $\mathbf{l}$ in Eq.(A.7) and the quantities in Eq.(A.8) are not derived as gradients of a spatial field, such that the terminology *velocity gradient* should not be interpreted in a strict sense.

Bibliography

[1] ABAQUS-VERSION 6.14 Dassault Systemes Simulia Corp., 2014, Providence, RI, USA, Theory manual - Version 6.14.

[2] ACHT, C.; DALGIÇ, M.; FRERICHS, F.; HUNKEL, M.; IRRETIER, A.; LÜBBEN, T.; SURM, H., 2008, Ermittlung der Materialdaten zur Simulation des Durchhärtens von Komponenten aus 100Cr6 - Teil 1, HTM Journal of Heat Treatment and Materials, **63**, 234-244

[3] AHRENS, U., 2003, Beanspruchungsabhängiges Umwandlungsverhalten und Umwandlungsplastizität niedrig legierter Stähle mit unterschiedlich hohen Kohlenstoffgehalten, Dissertation, University of Paderborn, Germany

[4] ALTENBACH, H.; ALTENBACH, J.; ZOLOCHEVSKY, A., 1995, Erweiterte Deformationsmodelle und Versagenskriterien der Werkstoffmechanik, Deutscher Verlag für Grundstoffindustrie, Stuttgart

[5] AMMAR, K.; APPOLAIRE, B.; CAILLETAUD, G.; FEYEL, F.; AND FOREST, S., 2009, Finite element formulation of a phase field model based on the concept of generalized stresses, Computational Materials Sciences, **45**, 800-805

[6] ANTRETTER, T.; FISCHER, F.D.; CAILLETAUD, G., 2004, A numerical model for Transformation Induced Plasticity (TRIP). Int. J. Phys. IV France, **115**, 233–241.

[7] ASM Handbook, 2002, Mechanical testing and evaluation, Materials Part Ohio, Vol. 8

[8] AHRENS, U.; MAIER, H.J.; MAKSOUD, A. EL .M., 2004, Stress affected transformation in low alloy steels-factors limiting prediction of plastic strains, Int. J. Phys. IV France, **120**, 615-623

[9] ATTANASIO, A.; UMBRELLO, D.; CAPPELLINI, C.; ROTELLA, G.; M'SAOUBI, R., 2011, Tool wear effects on white and dark layer formation in hard turning of AISI 52100 steel, Wear 286-287, 98-107

[10] AVRAMI, M., 1939, Kinetic of phase change I: general theory, J. Chem. Phys., **7**, 103-112.

[11] Behrens, A., Westhoff, B., Kalisch, K., 2005, Application of the finite element method at the chip forming process under high speed cutting conditions, in Tönshoff, H. K., Hollmann, F. (editors), Hochgeschwindigkeitsspanen, 112-134, Wiley-vch

References

[12] Betten, J.; Sklepus, S.; Zolochevsky, A., 1998, A creep damage model for initially isotropic materials with different properties in tension and compression, Eng. Fract. Mechs., **59**, 5, 623-641

[13] Böhm, M.; Dachkovski, S.; Hunkel, M.; Lübben, T.; Wolff, M., 2003, Phasenumwandlungen im Stahl: Übersicht über einige makroskopische Modelle für Phasenumwandlungen im Stahl, Berichte aus der Technomathematik, FB 3, Universität Bremen

[14] Bökenheide, S., Wolff, M., Dalgic, M., Lammers, D., Linke, D., 2011, Creep, phase transformations and transformation-induced plasticity of 100Cr6 steel during heating, in: Proc. 3rd Int. Conf. on Distortion Engineering, Bremen, Germany, 14-16 September, edited by H.W. Zoch and T. Lübben (IWT Bremen, Bremen, 2011), 411-418.

[15] Cailletaud, G., Saï, K., 1995, Study of plastic/viscoplastic models with various inelastic mechanisms. Int. J. Plast., **11**, 991-1005

[16] Chan, S.K., 1977, Steady-state kinetics of diffusionless first order phase transformations, J. Chem. Phys., **67**, 5755-5762

[17] Cheng, C., Mahnken, R., 2015, A multi-mechanism model for cutting simulations based on the concept of generalized stresses, Comp. Mat. Sci., **100**, B, 144-158

[18] Cherkaoui, M., 2002, Transformation induced plasticity: Mechanisms and Modeling, Journal of Eng. Mats. Tech., **124**, 55- 61

[19] Denis, S.; Simon, A.; Beck, G., 1983, Analysis of the thermomechanical behaviour of steel during martensitic quenching and calculation of internal stresses, Macherauch, E., Hauk, V. (Hrsg.), 211-238

[20] Denis, S., 1997, Considering stress-phase transformation interaction in the calculation of heat treatment residuel stresses, In: Mechanics of solids with phase changes, **368**, 293-317, eds. Berveiller, M., Fischer, F. D., Springer-Verlag

[21] Dudzinski, D., Molinari, A., 1997, Modelling of cutting for viscoplastic materials, *Int. J. Mech. Sci.*, **39**, 4, 369-389

[22] Ehlers, W., 1995, A single-surface yield function for geomaterials, Archive of Applied Mechanics, **65**, 246-259

[23] Eterovic, A.L., Bathe, K.J., 1990. A hyperelastic based large strain elasto-plastic constitutive formulation with combined isotropic-kinematic hardening using the logarithmic stress and strain measures. Int. J. Num. Meth. Eng., **30**, 1099-1114.

[24] Fischer, F.D.; Sun, Q.-P.; Tanaka, K., 1996, Transformation-induced plasticity (TRIP), ASME Appl. Mech. Rev., **49**, 317

110

References

[25] FISCHER, F.D.; OBERAIGNER, E.R.; TANAKA, K.; NISHIMURA, F., 1998, Transformation induced plasticty revised an updated formulation, Int. J. Solids Structures, **35**, 8, 2209-2227

[26] FISCHER, F.D.; REISNER, G.; WERNER, E.; TANAKA, K.; CAILLETAUD, G.; ANTRETTER, T., 2000, A new view on transformation-induced plasticity (TRIP), Int. J. of Plasticity **16**, 723-748

[27] FOREST, S.; AMMAR, K.; APPOLAIRE, B., 2011, Micromorphic vs. Phase-Field Approaches for gradient Viscoplasticity and Phase Transformations, Lecture Notes in Applied and Computational Mechanics **59** (2011), S. 69 - 88.

[28] B.J.GRIFFITHS, 1987, Mechanisms of white layer generation with reference to machining and deformation processes, Transactions of the ASME: Journal of Tribology, **109**, 525–530.

[29] DE GROOT, S., MAZUR, P., 1984, Non-Equilibrium Thermodynamics, Dover Publications, New York.

[30] Y.B. GUO., C. R. LIU, 2001, Mechanical Properties of Hardened AISI 52100 Steel in Hard Machining Processes, J. Manuf. Sci. Eng, **124**, 1, 1-9

[31] GURTIN, M., 1996, Generalized Ginzburg-Landau and Cahn-Hilliard equations based on a microforce balance, Physica D, **92**, 178-192

[32] HALLBERG, H.; HAKANSSON , P.; RISTIMAA, M., 2007, A constitutive model for the formation of martensite in austenitic steels under large strain plasticity, Int. J. of Plasticity, **23**, 1213-1239

[33] HALLE, T., 2005, Zusammenhänge zwischen Spanvorgängen und dem mechanischen Werkstoffverhalten bei hohen Dehnungsgeschwindigkeiten, Dissertation, Technical University of Chemnitz, Germany

[34] HAUPT, P., 2002, Continuum Mechanics and Theory of Materials, Springer-Verlag, Berlin.

[35] HOLTERMANN, R.; MENZEL, A.; SCHUMANN, S.; BIERMANN, D.; SIEBRECHT, T.; KERSTING, P., 2015, Modelling and simulation of Internal Traverse Grinding: bridging meso- and macro-scale simulations, Production Engineering - Research and Development, **9** 4, S. 451-463

[36] Hortig, Ch., 2010, Local and non-local thermomechanical modeling and finite-element simulation of high-speed cutting, Dissertation, University of Dortmund

[37] HUH, H.; KANG, W.J., 2002, Crash-worthiness assessment of thin-walled structures with the high-strength steel sheet, Int. J. of Veh. Des., **30**, Numbers 1/2

References

[38] IDESMAN, A.V.; LEVITAS, V.I.; PRESTON, D.L.; CHO, J.-Y., 2005, Finite element simulations of martensites of martensite phase transitions and microstructures based on a strain softening model, Journal of the Mechanics and Physics of Solids, **53**, 495-523

[39] IRRETIER, A., 2008, Abschlussbericht Projekt C1 "Stoffwertebestimmung", Sonderforschungsbereichs 570 "Distorsion Engineering", University of Bremen, Germany

[40] IWAMOTO, T., TSUTA, T., TOMITA, T., 1998, Investigation on deformation mode dependence of strain-induced martensitic transformation in TRIP steels and modeling of transformation kinetics, Int. J. Mech. Sci., **40**(2-3), 173-182

[41] IWAMOTO, T., TSUTA, T., 2004, Finite element simulation of martensitic transformation in single-crystal TRIP steel based on crystal plasticity with cellular automata approach, Key Eng. Mater., **274-276**, 679-684

[42] IWAMOTO, T., 2004, Multiscale computational simulation of deformation behavior of TRIP steel with growth of martensitic particles in unit cell by asymptotic homogenization method, Int. J. of Plasticity, **20**, 841-869

[43] JOHNSON, W.A.; MEHL, R. F., 1939, Reaction kinetics in process of nucleation and growth, Trans. AIME, **135**, 416–458

[44] Johnson, G.R., Cook, W.H., 1983, A constitutive model and data for metals subjected to large strain rates and high temperatures, Proc. 7th Int. Symp, on Ballistics, The Hague, 541-547

[45] KOISTINEN, D.P.; MARBURGER, R.E., 1959, A general equation prescribing the extent of the austenite-martensite transformation in pure iron-carbon alloys and plain carbon steels, Acta Metallica, **7**, 59-60

[46] LEBLOND, J.B.; DEVAUX, J., 1984, A new kinetic model for anisothermal metallurgical transformations in steels including effect of austenite grain size, Acta Metallurgica, **32**, 137-146

[47] LEBLOND, J.B., 1989, Mathematical modelling of transformation plasticity in steels II: Coupling with strain hardening phenomena, Int. J. of Plasticity **5**, 537-591

[48] LEVITAS, A.V.; IDESMAN, A.V.; OLSON, G.B., 1998, Continuum modeling of strain-induced martensitic phase transformation at shear-band intersections, Acta Materialia, **47**(1), 219-233

[49] MAHNKEN, R., 2001, Strength difference in compression and tension and pressure dependence of yielding in elasto-plasticity, Comp. Meths. Appl. Mech. Eng., **190**, 5057-5080,

[50] MAHNKEN, R., 2003, Creep simulation of asymmetric effects by use of stress mode dependent weighting functions, Int. Journal of Solids & Structures, **40**, 6189-6209

112

References

[51] Mahnken, R., 2005, Creep simulation of asymmetric effects at large strains by stress mode decomposition, Comp. Meths. Appl. Mech. Eng., **94**, 4221-4243

[52] Mahnken, R., 2005, Void growth in finite deformation elasto-plasticity due to hydrostatic stress states, Comp. Meths. Appl. Mech. Eng., **194**, 3689–3709

[53] Mahnken, R.; Johansson, M.; Runesson, K., 1998, Parameter estimation for a viscoplastic damage model using a gradient-based optimization algorithm. Eng. Comput., **15**(7): 925-955.

[54] Mahnken, R., 2004, Identification of material parameters for constitutive equations, In: Encyclopedia of Computational Mechanics, Vol. 2, Chapter 19, Eds. E. Stein, R. de Borst, T.J.R. Hughes, John Wiley and Sons Ltd, Chichester,

[55] Mahnken, R.; Schneidt, A., 2010, A Thermodynamic Framework and Numerical Aspects for Transformation-Induced Plasticity at Large Strains, Archives of Mechanics, **80**, 229-253

[56] Mahnken, R.; Schneidt, A.; Antretter, T., 2009, Macro modelling and homogenization for transformation induced plasticity of a low-alloy steel, Int. J. Plasticity, **25**, 183-204

[57] Mahnken, R.; Wolff, M.; Cheng, C., 2013, A multi-mechanism model for cutting simulations combining visco-plastic asymmetry and phase transformation, Int. J. Solids Struct. **50**, 3045-3066

[58] Mahnken, R.; Wolff, M.; Schneidt, A.; Böhm, M., 2012, Multi-Phase Transformations at Large Strains - Thermodynamic Framework and Simulation, International Journal of Plasticity, **39**, 1-26

[59] Mahnken, R.; Wolff, M.; Schneidt, A., 2012 Macro modelling for multi-phase transformations at large strains, European Congress on Computational Methods in Applied Sciences and Engineering (ECCOMAS 2012), J. Eberhardsteiner *et al.* (eds.), Vienna, Austria, September 10-14

[60] Maier, H.J.; Ahrens, U., 2002, Isothermal bainitic transformation in low alloy steels: factors limiting prediction of the resulting materials properties, Euromat, vol. 2. Elsevier, Oxford. 817–822.

[61] Marsden, J.E.; Hughes, T.J.R., 1993, Mathematical foundations of elasticity, Dover Publications, New York

[62] Marusich, T., Ortiz, M.: 1995, Modelling and Simulation of High-Speed Machining, Int. J. Num. Meths. Eng., **38**, 3675-3694

[63] Maugin, Gerard A.; Metrikine, Andrei V., 2010, Mechanics of generalized continua, one hundred years after the Cosserats, Springer Berlin Heidelberg

References

[64] MILLER, M.P., MCDOWELL, D.L., 1996, Modelling large strain multiaxial effects in FCC polycrystals., Int. J. Plast.**12**(7), 875-902

[65] MIOKOVIC, T.; SCHWARZER, J.; SCHULZE, V.; VÖHRINGER, O.; LÖHE, D., 2004, Description of short time phase transformations during the heating of steels based on high-rate experimental data, J. de Physique IV, **120**, 591-598.

[66] NOLTING, W., 2010, Grundkurs Theoretische Physik 4, Springer-Verlag, Berlin.

[67] Ozel, T., Zeren, E., 2004, Determination of work material flow stress and friction for FEA of machining using orthogonal cutting tests, Journal of Materials Processing Technology, **153-154**, 1019-1025

[68] RANIECKI, B.; BRUHNS, O., 1991, Thermodynamic reference model for elastic-plastic solids undergoing phase transformations, Archives of Mechanics, **43**, 343-376

[69] RAMESH, A; MELKOTE, S.N., 2007, Modeling of white layer formaion under thermally dominant conditions in orthogonal machining of hardened AISI 52100 steel, International Journal of Machine Tools & Manufacture, **48**, 402-414

[70] Saï, K., 2011, Multi-mechanism models: Present state and future trends, International Journal of Plasticity, **27**, 250-281

[71] SCHWER, L., 2007, Optional Strain-Rate Forms for the Johnson Cook Constitutive Model and the Role of the Parameter ε_0, 6. LS-DYNA Anwenderform, Frankenthal

[72] R. SIEVERT, H.-D. NOACK, A. HAMANN, P. LÖWE, K.N. SINGH, G. KÜNECKE, R. CLOS, U. SCHREPPEL, P. VEIT, E. UHLMANN, R. ZETTIER, 2003, Simulation der Spansegmentierung beim Hochgeschwindigkeits- Zerspanen unter Berücksichtigung duktiler Schädigung, Technische Mechanik, **23**(2-4), 216-233

[73] SIMO, J.C., 1992, Algorithms for static and dynamic multiplicative plasticity that preserve the classical return mapping schemes of the infinitesimal theory, Comp. Meths. Appl. Mech. Eng., **99**, 61–112

[74] SIMO, J.C.; HUGHES, T.J.R., 1998, Computational Inelasticity, Interdisciplinary Applied Mathematics, **7**, Mechanics and Materials, Springer-Verlag.

[75] STOUFFER, D.C.; DAME, L.T., 1996, Inelastic Deformation of Metals, John Wiley & Sons, New York

[76] SPITZIG, W.A.; SOBER, R.J.; RICHMOND, O., 1975, Pressure dependence of yielding and associated volume expansion in tempered martensite, *Acta Metallurgica,* **23**, 885–893

[77] D. D. TJAHJANTO, S. TURTELTAUB, A. S. J. SUIKER, 2008, Crystallographically based model for transformation-induced plasticity in multiphase carbon steels, Continuum Mech. Thermodyn, **19**, 399-422

114

References

[78] TURTELTAUB, S., SUIKER, A.S.J., 2005, Transformation-induced plasticity in ferrous alloys. J. Mech. Phys. Solids, **53**, 1747-1788.

[79] UHLMANN, E.; MAHNKEN, R.; IVANOV, I. M.; CHENG, C., 2012, FEM modeling of hard turning with consideration of phase transformations, 1st International Conference on Thermo-Mechanically Graded Materials, Transregio 30, 29-30. October 2012, Kassel.

[80] UMBRELLO, D.; HUA, J.; SHIVPURI, R., 2004, Hardness-based flow stress and fracture models for numerical simulation of hard machining AISI 52100 bearing steel, Ma. Sci. Eng, **A 374**, 90-100

[81] UMBRELLO, D.; SAOUBI, R.M. AND OUTEIRO, J.C., 2007, The influence of Johnson–Cook material constants on finite element simulation of machining of AISI 316L steel, Int J Mach Tools Manuf. **47**, 462–470

[82] UMBRELLO, D.; FILICE, L., 2009, Improving surface integrity in orthogonal machining of hardened AISI 52100 steel by modeling white and dark layers formation, Annals of CIRP, **58**(1), 73-76.

[83] VOYIADJIS, G.Z.; ZOLOCHEVSKY, A., 1998, Modeling of secondary creep behaviour for anisotropic materials with different properties in tension and compression. Int. J. Plast., **14**(10-11), 388-399.

[84] VOYIADJIS, G.Z.; ZOLOCHEVSKY, A., 2000, Modeling of secondary creep behaviour for anisotropic materials with different properties in tension and compression. Int. J. Solids Struct., **37**, 3281-3303.

[85] WEBER, G.; ANAND, L., 1990, Finite Deformation Constitutive Equations and a Time Integration Procedure for Isotropic, Hyperelastic-Viscoplastic Solids, Comp. Meths. Appl. Mech. Eng., **79**, 173–202

[86] WOLFF, M.; BÖHM, M.; LÖWISCH, G.; SCHMIDT, A., 2005, Modelling and testing of transformation-induced plasticity and stress dependent phase transformations in steel via simple experiments, Comput. Mater. Sci. 32, 604–610.

[87] WOLFF, M.; BÖHM, M.; SCHMIDT, A., 2006, Modeling of steel phenomena and their interactions - an internal variable approch, Materialwissenschaft und Werkstofftechnik, **37**(1), 147-151

[88] WOLFF, M.; BÖHM, M.; BOETTCHER, S., 2007, Phase transformations in steel in the multi-phase case, general modelling and parameter identification, Berichte aus der Technomathematik, FB 3, Universität Bremen

[89] WOLFF, M.; BÖHM, M.; HELM, D., 2008, Material behavior of steel – modeling of complex phenomena and thermodynamic consistency, Int. J. Plasticity, **24**, 746-774

References

[90] Wolff, M.; Böhm, M.; Suhr, B., 2009, Comparison of different approaches to transformation-induced plasticity in steel, Materialwissenschaften und Werkstofftechnik, **40**(5-6), 454-459

[91] Wolff, M.; Böhm, M.; Mahnken, R.; Suhr, B., 2011, Implementation of an algorithm for general material behaviour of steel taking interaction of plasticity and transformation-induced plasticity into account, Int. J. Numer. Meth. Engng, **87**, 1183-1206

[92] Zerilli, F.J.; Armstrong, R.W., 1987, Dislocation-mechanics-based constitutive relations for material dynamics calculations, Journal of Applied Physics, **61**, 1816

[93] Zolochevskii, A.A., 1989, Modification of the theory of plasticity of materials differently resistant to tension and compression for simple loading processes, Soviet Applied Mechanics (transl. Prikladnaya Mekhanika), **24**(12), 1212-1217

[94] Zolochevskii, A.A., 1990, Method of calculating the strength of mine pipes formed from materials that behave differently under tension and compression, *Strength of Materials* (transl. Problemy Prochnosti), **22**(3), 422-428

[95] Zolochevsky, A.A. (1991) Creep of isotropic and anisotropic materials with different behaviour in tension and compression , In: Zyczkovski, M. (Ed.), Creep in Structures, Springer-Verlag, Berlin, 217-220

List of Figures

List of Tables

Lebenslauf wurde aus datenschutzrechtlichen Gründen entfernt.